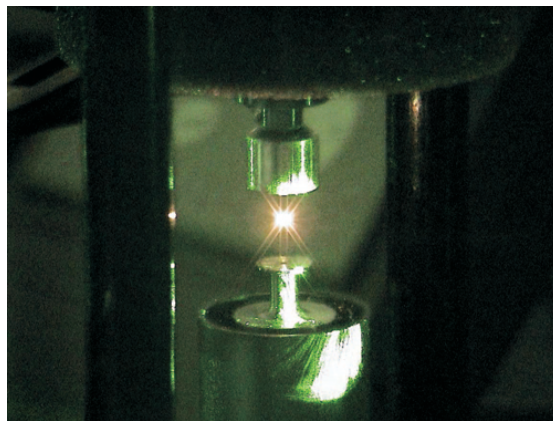# Liquid Droplet Dye Laser

M.Sc. Thesis

Hatim Azzouz

Supervisors: Anders Kristensen, Niels Asger Mortensen
and Jan Westenkær Thomsen

MIC – Department of Micro and Nanotechnology
DTU – Technical University of Denmark
KU – University of Copenhagen

April 2005

Preface

This M.Sc. thesis has been conducted at MIC - Department of Micro and Nanotechnology at the technical University of Denmark (DTU). The thesis title is "Liquid Droplet Dye Laser". The thesis equals 60 ECTS. The work has been presented at the Micro Total Analysis System 2004 International Conference (μTAS'04) September 26-30, Malmö, Sweden.

The work was done under the supervision of the main supervisor Associate Professor Anders kristensen, co-supervisor Associate Professor Niels Asger Mortensen and my internal supervisor Associate Professor Jan W. Thomsen, to whom I am greatly indebted and thankful for the advice, help and support they provided me. I especially appreciate the help from Niels Asger Mortensen for helping to develop the Whispering Gallery resonator model. I owe my gratitude to Ph.D-student Søren Balslev for supplying vast amounts of ideas and guidance on theory and applications. I would like to thank Michael Stenbæk Schmidt for his advices as regards the fabrication of hydrophobic surfaces and for training me in fabrication skills in the cleanroom. Also I would like to thank all the colleagues as well as friends at MIC for the nice time we had together.

Last, but definitely not least, I would like to express my deepest gratitude to my beloved family, especially my father and my mother, for their endless moral support, patience and understanding.

The picture shown on the frontpage is a liquid droplet dye laser levitated by a so-called levitator apparatus.

<div align="right">

Hatim Azzouz

</div>

Contents

Chapter 1

Introduction

In all branches of modern optics, conventional optical cavities consisting of two or more mirrors are utilized. However, the practical usage of such cavities is restricted, and the fabrication of good mirrors and their alignment are rather expensive and difficult tasks.

Open spherical micro-cavities may become an alternative for the usual optical cavities, especially when fabrication of these is simple and inexpensive.

In these spherical cavities, light is trapped near the surface by repeated total internal reflection at grazing incidence in the so-called Whispering Gallery Modes (WGM) [1], [40].

Research interest in optical WGM resonators has grown dramatically in the field of cavity quantum electrodynamics (CQED) and both the fundamental and applied optics. For example, it is highly utilized in many evolving photonics applications as high-resolution spectroscopy and remote sensing [2].

For sensing tasks, analytical chemistry or other measurements, the tunability of light sources can be provided by liquid dye lasers [3]. Liquid dye lasers are widely used as tunable narrow bandwidth light sources in the visible wavelength range from app. 400 nm to 900 nm; Fig 3.3, and have a very wide fluorescent optical band from around 100 nm to 200 nm. Several commercially available laser dyes have a very high efficiency [5], allowing for miniaturization of the laser cavity, with the possibility to enter the "zero-threshold lasing" [5] regime, where the cavity supports only one or few modes in the gain window. The lasing has even been demonstrated in thin sheets of liquid dye laser, relying only on reflection at the liquid-air interfaces [6].

This combined with the perspective of digital microfluidic circuits [7], it is interesting to functionalise liquid droplets. And since earlier lasing in spherical cavities have only focused on solid state materials [1], it is interesting to investigate the lasing properties of liquid droplets of a laser dye solution.

In this thesis I present the first observation of lasing in a spherical shaped droplet containing a laser dye deposited on a hydrophobic substrate. The liquid droplet, with linear dimensions in the micrometer range forms a self-organized laser cavity, relying on total internal reflection at the liquid-air and liquid-substrate interfaces at the incidence angle $> 44°$. Lasing can occur in all droplet shapes fulfilling the resonance condition. However, in this project we are only interested in a spherical shape, since a sphere is easily described mathematically; only by two parameters: radius and contact angle. Interested in creating

spherical shaped droplets with highest possible contact angle; i.e. less contact with the substrate, suitable hydrophobic surfaces were fabricated. The droplet contains the laser dye Rhodamine 6G dissolved in ethylene glycol and was supplied with energy by being optically pumped (532 nm) by an external frequency doubled Nd:YAG laser.

Towards the end of the project, we were informed that a scientific group from Lund University leaded by Professor Staffan Nillson [8] was able to levitate spherical liquid micro-droplets. And since the purpose of this project, as above mentioned, is to create spherical liquid droplets with at least possible contact with the surface, investigating the lasing properties of the levitated spherical liquid droplet dye laser; i.e. not being disturbed by the influence of a contacting surface, was quit opportune and convenient to carry out. Thus, we also present, to our knowledge, the first observation of lasing in a spherical shaped levitated droplet.

The thesis is introduced by Chapter 2 describing the hydrostatic of the micro-droplet and introducing the physical requirements for creating a spherical droplet with the optimal contact angle followed by the fundamental laser theory action in Chapter 3. In Chapter 4 the resonator model describes the morphology-dependent resonances (or WGMs), followed by Chapter 5 describing the various followed steps in fabricating hydrophobic surfaces with the aim to optimize the contact angle. The obtained contact angle results are also presented in Chapter 5. The utilized setup for the optical characterization of the liquid droplet dye laser is presented in Chapter 6 followed by the obtained optical characterization results of the droplet in Chapter 7. The lasing measurements performed on the levitated liquid droplet dye laser is presented in Section 7.4. The thesis is ended by a conclusion in Chapter 8.

Chapter 2

Hydrostatics of Microdroplets

2.1 Introduction

To understand the formation of liquid droplets[1] on a solid surface two central and important physical quantities must be introduced and derived namely, the surface tension and contact angle. These two quantities are responsible for almost all the surface related phenomena occurring in nature such as the capillary rise, formation of soap bubbles, the alveoli of the lungs, the insects ability of walking on water.

The following section, Section 2.2, will be introduced by a definition of the surface tension followed by a force and energy description of the surface tension. Hereafter, other central quantities such as Young-Laplace equation and the dimensionless Bond number will be reviewed. Equally, the definition of contact angle will be introduced in the beginning of Section 2.3, also followed by a force and energy description of the contact angle. Wetting criteria together with a brief analysis of the properties of rough surfaces, will be given in Section 2.3.2 and Section 2.3.3, respectively. The chapter is ended by a computer simulation of the shape of the droplet in Section 2.4.

2.2 Surface Tension

The surface tension is a measure of the tightness of the surface film that seems to cover the surface of a liquid, the tendency of molecules at the surface to be pulled inward: the greater the surface tension, the tighter the surface film seems to be. Although referred to as a free energy per unit area, surface tension may equally well be thought of as force per unit length. The surface tension is a definite and accurately measurable property of the interface between two phases.

---

[1]By a droplet we mean a small volume of liquid at equilibrium surrounded by its vapor (and possibly also air).

2.2.1 Force and Energy Description

Force Description

Consider a liquid-gas interface, that is a liquid droplet surrounded by air, for example. In the liquid the molecules are bound by the van der Waals forces, where the gas molecules are relatively free to move. In the interior of the liquid, each molecule are attracted equally in all directions by its neighbors, and therefore no resultant force tending to move it in any direction. For a surface molecule, however, only half of the surrounding space is occupied by other liquid molecules; Fig 2.1. Therefore, there is no outward force attracting the surface molecules from the liquid, and there is therefore a net inward attraction on the surface molecules. This forces the surface to curve, and the surface behaves as if it was a stretched membrane, with a tension

$$\sigma = \frac{\mathcal{F}}{l} \tag{2.1}$$

along the edge length of the stretched membrane, i.e a force $\mathcal{F}$ per unit length l tending to decrease the surface area. For this reason, a droplet assumes a spherical shape because the surface tension pulls the molecules into the most compact shape, a sphere, neglecting the effects of gravity ; of course. Very small drops of liquid are almost exactly spherical; larger ones are flattened by their weights.

The most compact shape.
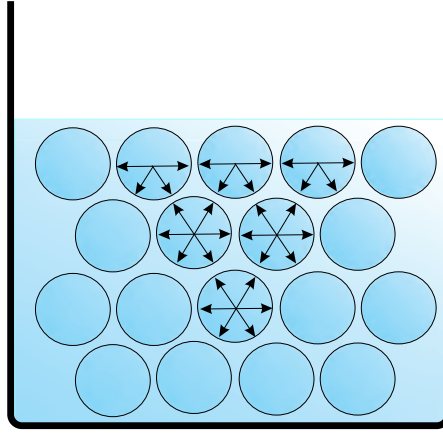
Figure 2.1: The intermolecular forces between the molecules tending to curve the surface.

Energy Description

The above-mentioned example, Fig 2.1, can also be interpreted in a different manner, namely by relating the surface tension to the surface energy. The expanding of the the surface area A of the liquid, will consequently result in an increase in the number of the molecules at the surface. This is due to the fact that molecules that were in the interior region are brought to exterior. For this to occur, a work W must be done to counteract the attractive forces among

these molecules and their neighbors. The work required to increase the surface is given by

$$dW = \sigma dA. \tag{2.2}$$

The molecules at the interface (liquid-gas) are attracted by less neighboring molecules than those in the interior. Therefore the attraction energy at the interface is less than that of the interior.

Now, the dimensions of the surface tension are energy/area $[\text{Jm}^{-2}]$. However, $[\text{Nm}^{-1}]^2$ is still the often used SI-unit for the surface tension σ.

The two descriptions, force and energy, of the surface tension can be shown to be similar, with the reference in Fig 2.2. Here we suppose that a film of liquid is stretched on a wire frame. When pulling the wire a distance dx, a force $\mathcal{F}$ will act in the opposite direction. The energy expended, $\mathcal{F}dx = W$, is given by

$$W = \sigma l dx. \tag{2.3}$$

And the work could equally have been expressed as

$$dW = \sigma dA, \tag{2.4}$$

with $dA = l dx$. In eq. (2.1) the surface tension is given as a force per length, whereas it in eq. (2.4) is given as energy per area.
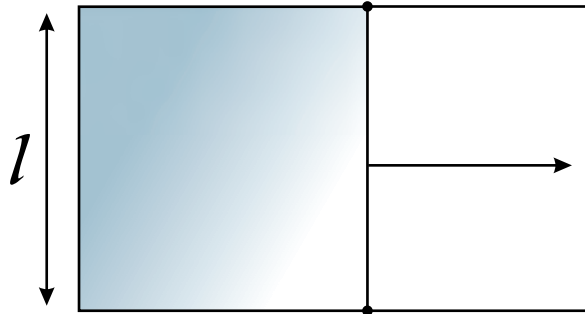
Figure 2.2: A soap film, for instance, stretched across a frame.

2.2.2 Surface Tension in The Formalism of Thermodynamic

Helmholtz Free Energy

We can express the energies related to surface effects in the language of Helmholtz and Gibbs functions. The molecules at the surface has an excess energy, relative to the interior of the liquid. At constant volume and temperature, the work of surface formation can be identified with the change in the Helmholtz free energy F given by

$$F = U - TS, \tag{2.5}$$

---

[2]That is because 1 J=1 Nm

where U is the internal energy, T is the temperature and S is the entropy of the system. The change of the internal energy U is given by

$$dU = TdS - pdV + \sigma dA, \qquad (2.6)$$

where p is the pressure and dV is the change of the volume. Inclusion of the change of the work in the expression for the change of the internal energy gives the differential form of the Helmholtz free energy

$$dF = -SdT - pdV + \sigma dA. \qquad (2.7)$$

Eq. (2.7) shows that the surface tension, σ, is a slope for the free energy at constant T and V, i.e. $dV = dT = 0$. Thus

$$\sigma = \left(\frac{\partial F}{\partial A} \right)_{T,V}. \qquad (2.8)$$

In other words, the surface tension is the surface free energy per unit area. What the surface tension states physically, is that for constant temperature and volume and for a given surface tension, a liquid minimizes its free energy by decreasing its surface area. But when increasing the temperature the surface tension is found to decrease. This is stated by

$$\frac{\partial \sigma}{\partial T} = \left(\frac{\partial^2 F}{\partial T \partial A} \right)_V \qquad (2.9)$$

derived from eq. (2.7).

Gibbs' Free Energy

When treating an equilibrium between two phases, we are in a state where temperature and pressure are constant in time. A function describing this state is the thermodynamic potential G called Gibbs's free energy. This is given by

$$G = F + PV = H - TS, \qquad (2.10)$$

where $H = TdS - pdV$ is the enthalpy. The differential form of G is given by

$$dG = -SdT + Vdp. \qquad (2.11)$$

For constant temperature and pressure the change in Gibbs' free energy is

$$dG = 0. \qquad (2.12)$$

The surface tension can also be defined in terms of the Gibbs free energy, as

$$\sigma = \left(\frac{\partial G}{\partial A} \right)_{T,p}. \qquad (2.13)$$

This is almost similar to the previously derived definition of surface tension, expressed in terms of Helmholtz free energy. However, the pressure is now required constant, instead of the volume, together with temperature, in the definition yielding that a liquid minimizes its energy by decreasing its surface area. Instead of holding the volume constant, the pressure is now required constant.

2.2.3 The Young Laplace Equation

As above mentioned, when the total free energy of the system minimizes, the surface area tends to minimize resulting in a curvature of the surface. This curvature, which is due to the surface tension of the liquid drop, creates a higher pressure within the drop than exists in the surrounding gas. This excesses pressure difference ΔP across the interface. An equation, for a curved surface, expressing the relation between surface tension, σ, the two radii of curvature, R_1 and R_2 [3] and the pressure difference, ΔP, across the interface is the so-called Young-Laplace equation given by

$$\Delta P = \sigma \left(\frac{1}{R_1} + \frac{1}{R_2} \right).$$
(2.14)

In order to derive an expression for the mentioned pressure difference, one has to consider the work needed to expand a small section of an arbitrary curved surface depicted in Fig 2.3, where we assume that both curvatures are locally constant. Now, consider the surface displaced a small distance dz, increasing its surface area. The resulting change in surface area will be

$$dA = (x + dx)(y + dy) - xy = xdy + ydx.$$
(2.15)

The work required to increase the surface by the amount dA is then given by

$$dW = \sigma dA = \sigma(xdy + ydx).$$
(2.16)

Similarly, the work could be expressed by a pressure difference, ΔP, acting on the area xy moved a distance dz. Hence

$$dW = \Delta Pxydz.$$
(2.17)

From trigonometrical considerations, it follows that

$$\frac{x + dx}{R_1 + dz} = \frac{x}{R_1} \quad \Rightarrow \quad dx = \frac{xdz}{R_1}$$
(2.18)

and

$$\frac{y + dy}{R_2 + dz} = \frac{y}{R_2} \quad \Rightarrow \quad dx = \frac{ydz}{R_2}.$$
(2.19)

If the surface is to be in equilibrium, the two work terms; the work expressed by the surface tension and the work expressed by the pressure difference, must be equal. Equating them and substituting the expressions for dx and dy, one gets the Young-Laplace equation

$$\Delta P = \sigma \left(\frac{1}{R_1} + \frac{1}{R_2} \right) = \sigma \left(-\nabla \cdot \hat{\mathbf{n}} \right).$$
(2.20)

The sign of the pressure difference is such that the pressure is less in the liquid than in the gas phase. Therefore, the radii of curvature (where both are of the same sign) always lie on the side of the interface having the greater pressure. Note that the curvature also can be defined by the divergence of the surface

---

[3]A thorough description of the origin of radius R_2 is given in [9].

unit normal: $-\nabla \cdot \widehat{\mathbf{n}}$. For a sphere, that is the case of both radii being equal, $R_1 = R_2 = R$, eq. (2.20) reduces to

$$\Delta P = \frac{2\sigma}{R} \qquad (2.21)$$

When an interface is plane, the pressure difference is zero as $R_1 \to \infty$ and $R_2 \to \infty$, i.e. the pressure is equal on both sides of the plane interface despite the interfacial tension; thus there is no pressure difference across the plane surface. But, as the two radii tend to zero, as is the case for small liquid droplets, the pressure difference becomes apparently important.
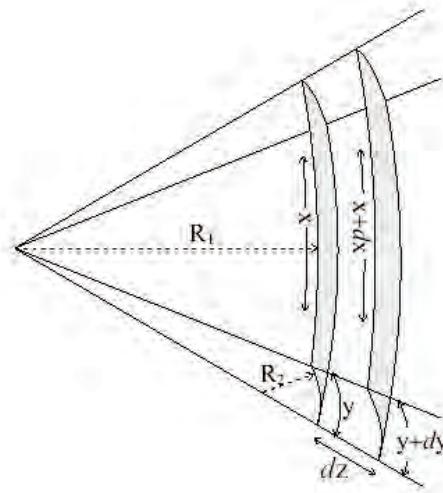
Figure 2.3: Condition for mechanical equilibrium for a curved surface [9].

2.2.4 Bond number

The Bond number B_0 is a special dimensionless number relating the gravitational force to the surface tension force, and is giving by

$$B_0 = \frac{[\text{gravitational force}]}{[\text{surface tension force}]} = \frac{\Delta \rho g d^2}{\sigma}, \qquad (2.22)$$

where $\Delta \rho$ is the difference between the interior drop density and the surrounding liquid density. d is the diameter of the drop. Interested in a hemispherical droplet [4] requires that the surface tension force is much larger than the gravitational force. Hence

$$B_0 \ll 1 \quad \Rightarrow \quad d \ll \left(\frac{\sigma}{\Delta \rho g}\right)^{1/2} \equiv \Delta_c, \qquad (2.23)$$

where Δ_c is the so-called capillary length. Δ_c defines wether a phenomena is controlled by gravity ($> \Delta_c$) or surface tension ($< \Delta_c$).

---

[4]By a hemispherical droplet we mean a droplet having a shape that is a part of a sphere.

The liquid used in this project for the creation of the droplet is ethylene glycol (EG). The liquid-gas surface tension and the density difference for EG [5] at room temperature is 47.3 mN/m [1] and 1.113 g/cm^3, respectively. Using the Bond number to calculate the droplet dimensions for EG with the overstated parameters (σ and $\Delta\rho$), the radius $R = d/2$ and the volume of the droplet ($V_{drop} = \frac{4}{3}\pi R^3$) must be much less than 1 mm and 4 μL, respectively, if the shape of the droplet is required hemispherical. This condition ($R \ll 1$ mm) for creating spherical formed droplet is quite satisfactory and reassuring, since our object is to create droplets in the micron range due to considerations concerning lasing (modes within the cavity) and which will be explained in Chapter 4.

2.3   Contact Angle

A contact angle θ, is geometrically, defined as the angle formed by a liquid at the three phase boundary where a liquid, gas and solid intersect. When a liquid drop is placed on a solid surface forming a contact angle, strictly, it will either spread out and wet the surface or stay on the surface letting the surface "unwetted". Therefore the contact angle is a quantitative measure of the wetting of a solid by a liquid, depending on the surface tension. The relation between the contact angle and the surface tension is given by the important Young's equation, which will be derived in the following section.

2.3.1   The Young Equation

Force description

Considering a liquid drop on a flat surface in static equilibrium, the contact line, forming an angle θ, has to remain fixed and a force balance has to be fulfilled; as shown in Fig 2.4. Three forces are acting on the liquid drop, written in terms of the surface tension components. Thus we have

$$\sigma \cos\theta = \sigma_{sg} - \sigma_{sl} \tag{2.24}$$

where $\sigma \cos\theta$ is the force component of the liquid-gas surface tension $\sigma (\equiv \sigma_{lg})$. σ_{sg} is the solid-gas surface tension and σ_{sl} is the solid-liquid surface tension. Eq. (2.24), relating the contact angle to the terms of surface tension is the so-called Young's equation.

Energy description

Although the force description of Young's equation is simple, it is more concise and convenient from a physical point of view to derive Young's equation from an energy minimization approach. This is attractive partly from a tautological standpoint because the forces are derivatives of the potential energy, partly because it despite being rigorous is exact. This energy approach contains no approximations. These will only be contained within the assumption that the droplet is a perfect sphere described by a radius R and a contact angle θ. The evaporation is neglected in the derivation. B. Shapiro *et al.* [62] introduces a

---

[5]Actually, the Rhodamine 6G is dissolved in EG, but since the concentration of Rhodamine 6G is negligible compared to the density of EG, only the last one will be taken into account.
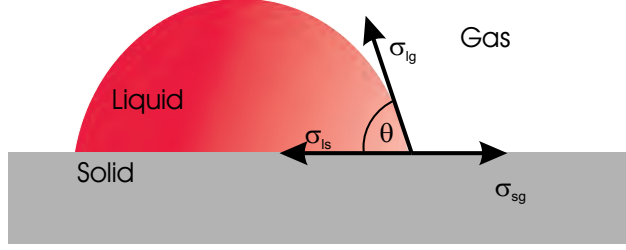
Figure 2.4: Static equilibrium forces acting upon a liquid droplet on a solid.

conversion from energy minimum to Young's equation, stating that in equilibrium the droplet will assume the shape R and θ, that minimizes its energy E, Fig 2.5. Thus, the derivative of the energy with respect to R and θ is zero:

$$dE = \left[\frac{\partial E}{\partial R}(R, \theta) + \right] dR + \left[\frac{\partial E}{\partial \theta}(R, \theta) + \right] d\theta = 0. \tag{2.25}$$

Because the infinitesimal change in energy has to be zero, eq. (2.25) states
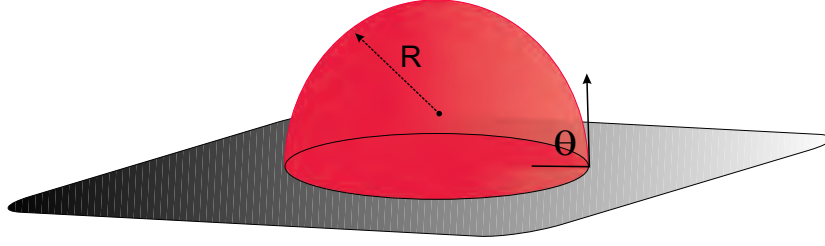
Figure 2.5: Spherical droplet geometry described by two parameters: radius R and contact angle θ.

that only two parameters can possibly change the shape: radius R and contact angle θ. If the radius increases, the contact angle must follow up by decreasing in order to keep the droplet volume constant. Substituting eq. (A.1)for the constant droplet volume in eq. (2.25) and solving it, we get

$$\left(-\frac{2 + \cos\theta}{2\pi R^2 \sin\theta}\right)\frac{dE}{d\theta} = \left(-\frac{2 + \cos\theta}{2\pi R^2 \sin\theta}\right)\left(\left[\frac{\partial E}{\partial R}(R, \theta) + \right]Rq(\theta)\right.$$
$$\left. + \left[\frac{\partial E}{\partial \theta}(R, \theta)\right]\right) = 0, \tag{2.26}$$

where $q(\theta)$ is given by eq. (A.5). In the case where E is expressed in terms of surface tension coefficient of the liquid-solid, liquid-gas and solid-gas interfaces, eq. (2.26) becomes exactly Young's equation derived in eq. (2.24). A more detailed derivation and conversion of the energy approach to the modified Young's equation is given in Appendix A.

2.3.2 Wetting

Young's equation can further be written in yet another form

$$k = \frac{\sigma_{sg} - \sigma_{sl}}{\sigma} = \cos\theta \qquad (2.27)$$

where k is the wetting coefficient lying in the interval $-1 \leq k \leq 1$. This interval can be divided in further four sub-intervals, as follows:

- If $k = 1$, that is a contact angle $\theta = 0°$, the liquid spreads completely over the surface of the solid. The solid is said to be *completely wetted*.

- If $0 \leq k \leq 1$, the contact angle is lying between 0 and $\pi/2$ (90°), and the solid is said to be *partially wetted*. The solid is also referred to as *hydrophilic*.

- If $-1 \leq k \leq 0$, the contact angle is lying between $\pi/2$ and π (180°), and the solid is termed *un-wetted*. In this case the solid is *hydrophobic*. In [22], the super-hydrophobicity is defined as contact angle greater than 150° for water.

- For $k = -1$ the contact angle is π. The solid in this un-physical state is termed *completely un-wetted*.

This is shown in Fig 2.6.
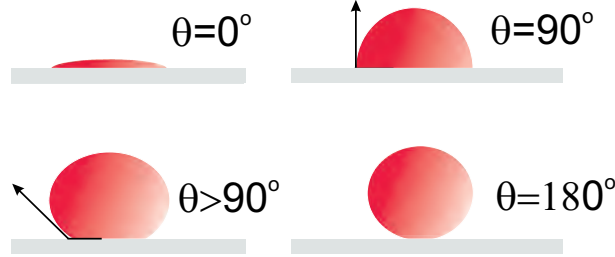
Figure 2.6: The contact angle of a drop on a solid surface with various wetting coefficient and conditions.

2.3.3 Rough Surfaces

So far we have only considered ideally surfaces, e.i. smooth flat homogeneously solid. More realistic surfaces are rough, and particularly this property shows to have a strong impact on the contact angle of a drop in equilibrium on a solid. The first to propose a description on the effect of surface roughness on the wettability of the solid was Wenzel [23].
The roughness r of a surface is defined as the ratio between the actual (or real) surface area A' and the projected one (the macroscopic) A. By considering an infinitesimal dx spreading (parallel to the surface) of a liquid edge on a rough surface, Fig 2.7, the surface tension components defined above are modified by a quantity $d\mathcal{F}$ given by

$$d\mathcal{F} = r(\sigma_{sl} - \sigma_{sg})dx + \sigma dx \cos\theta^*, \qquad (2.28)$$

where θ^* is the apparent contact angle (also called the effective or macroscopic contact angle). In equilibrium where $\mathcal{F}$ has its minimum we get Wenzel's equation

$$\cos\theta^* = r\cos\theta, \tag{2.29}$$

where θ is the contact angle on the same smooth surface given in Youngs's equation eq. (2.24). Hereby, it emerges from eq. (2.29) that the roughness actually increases the contact angle and thereby the wettability for the already hydrophobic surface ($\cos\theta < 0$), but decreases it for hydrophilic surfaces ($\cos\theta > 0$).

When placed on a rough surface the drop will assume a stable state and thereby choosing between two states. The drop can fill the roughness structures as shown in Fig 2.8(a), and the state is called *Wenzel* state. Otherwise, the drop will find it difficult to penetrate the roughness structures because of the capillary forces of the liquid, and the effect is referred to as the *Fakir* effect. In the Fakir state the air is trapped in between the roughness structures, and thereby providing the drop to sit on the composite surface made of solid and air. This is shown in Fig 2.8(b). Energetically, it can be favourable for the drop to break the
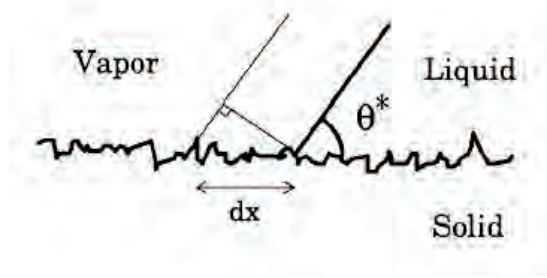
Figure 2.7: Infinitesimal spreading on a rough surface [23].

(a) The Wenzel state. The drop fills the roughness structures.

(b) The Fakir effect. The drop sit on the top of the air-solid surface.
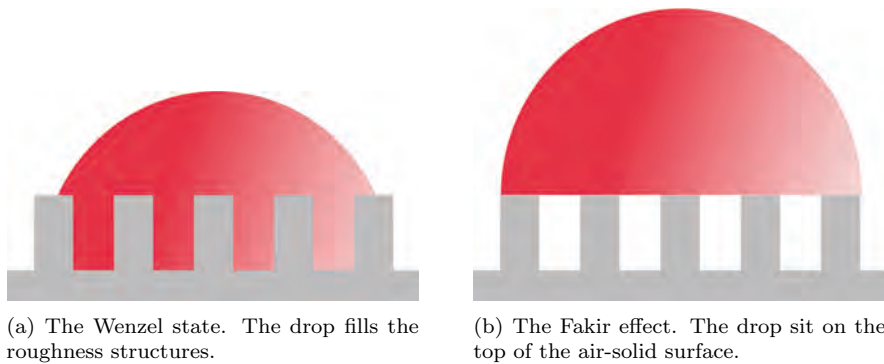
Figure 2.8: The two states; i.e. Wenzel or Fakir, a droplet can assume.

Wenzel state, if the surface energy is larger than the Fakir's. This is only the

case if $\cos\theta < -1/r$ [24], and the Fakir effect will be the stabile and thereby the favorite state. Thus the apparent contact angle in this case (Fakir state) is given by a weighted average of the contact angle θ on the same smooth surface, and the one on air, which is 180°, by Cassie-Baxter equation [23]

$$\cos\theta^* = \phi_s(1+\theta) - 1, \qquad (2.30)$$

where $\phi_s < 1$ is the fraction of the surface in contact with the droplet.

Hydrophobic surfaces possessing the Fakir or the Wenzel state are called the *slippy* or *sticky* surfaces, respectively. In the latter one, the drop will find it difficult to move, whereas in the slippy surface there will be little resistance to drop attachment or placement; i.e. the droplet is rejected, why the droplet will find it easy to move. This effect was observed in nature, specifically in the self-cleaning Lotus flower. This flower has a slippy surface and utilizes this property by letting water droplets roll of the surface and cleans it of contamination in its way, see Fig 2.9. The combination of the self-cleaning effect and high water-repellency characteristics by the Lotus flower has been dubbed the *Lotus-effect* by Prof. Dr. W. Barthlott, a botanist from the University of Bonn [25].

Figure 2.9: A droplet rolling off on a lotus leaf, thus cleaning the surface [26].

2.4   Simulating The Droplet Shape

Requiring a hemispherical shape of the droplet, the Bond-number estimates the droplet radius to be much less than 1 mm, i.e. $R < 1$ mm. Before we proceed, this estimate was investigated by using a simulation program called Surface Evolver, to predict the shape of the droplet for various radii. The Surface Evolver is an interactive program that minimizes the energy of a surface (thereby shaping it) subject to constraints. The energy can include surface tension, gravity and others. The Evolver is written in portable C. The initial surface is specified in a text file (a datafile). The used datafile (mound.fe) is for a mound of liquid sitting on a tabletop [6] with gravity acting on it. The drop starts as a cube, see Fig 2.10. The basic operation of the Evolver is to read in a datafile and take commands in from the user in the command prompt. The basic geometric elements used to represent a surface are vertices, edges, facets and

---

[6]Although, the Bond number predicts a spherical shape for droplets which are not in contact with some surface, we will simulate the shape of the droplet lying on a surface, since it only gives an approximative impression of the droplet form.

bodies. Vertices are points in space. Edges are straight line segments joining pairs of vertices. Facets are flat triangles by three edges. A surface is then a union of facets. The changeable parameters are: the contact angle, gravitation, volume and density. A surface is deemed to have a total energy, arising from
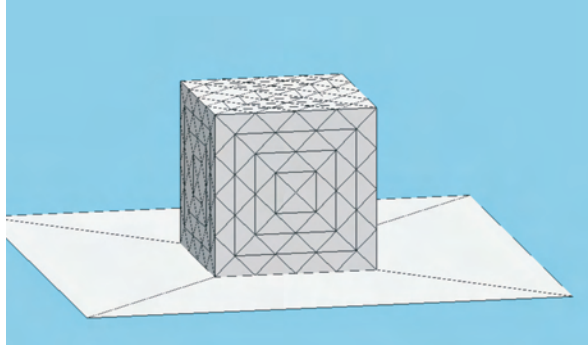

Figure 2.10: The drop starts as a cube.

surface tension (specified implicit through the contact angle) and gravitational energy. It is this energy which the Evolver minimizes. No particular units of measurements are used. The program only deals with numerical values. The fundamental operation of the Evolver is the iteration step, which reduces energy while obeying constraints. An iteration is one evolution step. The motion for the step is calculated by the following three steps:

- Firstly, the force on each vertex is calculated from the gradient of the total energy of the surface as a function of the position of that vertex.

- Secondly, the force gives the direction of the motion.

- Thirdly, the actual motion is found by multiplying the force by a global scale factor.

In the command prompt the contact angle can be varied from 0° to 180°, and the gravitation from 0 (off) to 10. Since the shape of the droplet, according to the Bond number, depends on which factor that is dominating; the surface tension or the gravitation, the diameter (or radius) of the droplet in this simulation can be varied and expressed through the gravitation for a given surface tension value (contact angle parameter). The gravitation parameter G, in the simulation was chosen to have dimensions of the numerator of eq. (2.22) which in terms of approximative values is expressed as $\Delta \rho g d^2 \approx 1000$ kg/m$^3 \cdot 10$ m/s$^2 \cdot d^2 = 1$ kg/m$^3 \cdot 10$ m/s$^2 \cdot [d^2 \cdot 10^3]$. From the expression it can be seen, that the density parameter in the datafile can be chosen to be 1, and still obey the expression written in terms of the SI-units, as long as d^2 is scaled with factor 1000. For diameter values of 0.1 mm, 1 mm, 1 cm and 10 cm, we get the gravitation parameter values of 0.0001, 0.01, 1 and > 10. These gravitation parameter values were inserted in the command prompt for the contact angle parameter of 140°. The simulation results predicting the shape of droplets for these values relating the diameter are shown in Fig 2.11, 2.12, 2.13 and 2.14.
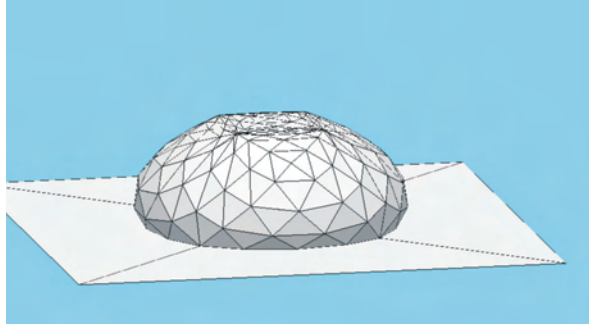
Figure 2.11: Given a contact angle of $140°$ and a diameter of $d = 10$ cm, the shape of the droplet is squashed.
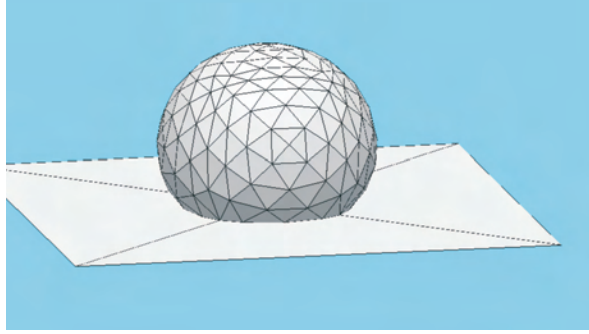
Figure 2.12: Given the same contact angle and $d = 1$ cm, the shape of the droplet becomes more spherical but remains squashed.

It emerges from the figures that for large diameters, i.e. $R = 5$ cm, 0.5 cm $\gg 1$ mm), the droplets squashes, because of the dominant gravitation. But for decreasing radii ($R \ll 1$ mm), the surface tension overcomes the gravitation resulting in a more hemispherical shape of the droplet. This is in good agreement with the estimate given by the Bond number. The shape of EG droplets in real (by experiments) is shown in Fig 2.15 with two different diameters.
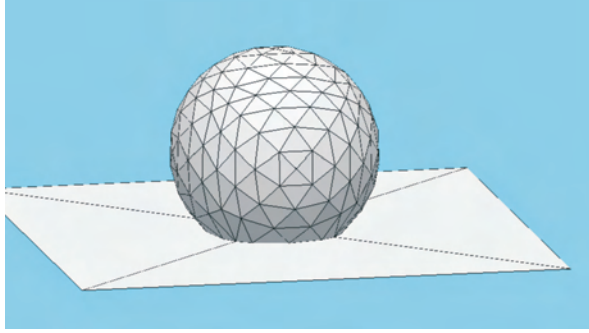
Figure 2.13: For $d = 1$ mm, the shape of the droplet becomes hemispherical.
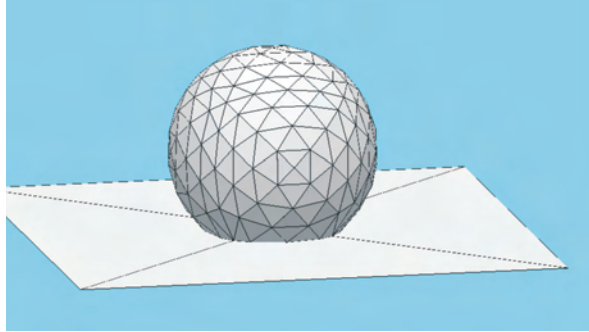
Figure 2.14: For $d = 0.1$ mm, the droplet assumes a more perfect spherical shape than the one in Fig 2.13.
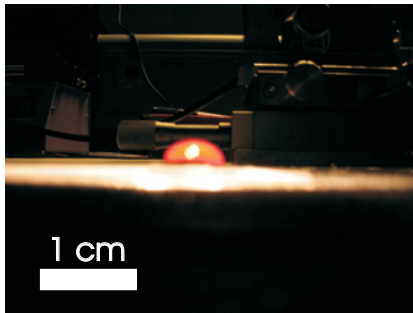
(a) An EG droplet with an approximate diameter of 6 mm. The droplet is too large to be viewed with a microscope why a digital camera was used. Although the sharpness of the picture is not that good, it is clear that the EG droplet is squashed because it exceeds the Bond number condition.
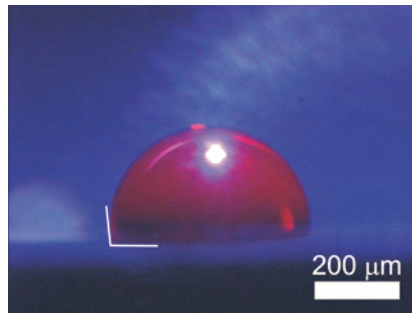
(b) A spherical shaped EG droplet with $d = 540$ μm lying on a surface.

Figure 2.15: Two EG droplets lying on hydrophobic surfaces. The pictures show the behavior of the droplet below and above the Bond number for two different radii.

Chapter 3

Laser Theory and Fundamentals

The term *laser* is an acronym for Light Amplification by Stimulated Emission of Radiation. A laser is a device that amplifies light signals and produces a highly directional, high-intensity beam that typically has a well-defined wavelength. Stimulated emission is the radiative process responsible for laser action and was predicted by Albert Einstein in 1916. Until that time, only two radiative processes were believed to occur when light (photon) interacts with matter (atom), namely stimulated absorbtion and spontaneous emission.

In Section 3.1, the three radiative processes involved in the light interaction with matter will briefly be introduced, followed by a definition of central terms such as the necessary population inversion and the gain threshold that must be exceeded in order to get laser action in Section 3.2. Section 3.3 provides an overview of what a laser consists of. The laser operation is carried out in Section 3.4. The chapter is ended by Section 3.5 regarding the concept of multi-mode laser oscillation.

3.1   Interaction of radiation and Matter

3.1.1   Definition of Radiative Processes

In 1916 Einstein proposed that the state of thermodynamic equilibrium between radiation and matter, where the distribution of radiation energy with frequency is described by Planck's Law and the distribution of atoms amongst their various excite states by the Boltzmann distribution, could be explained in terms of three basic processes: stimulated absorption, spontaneous emission, and stimulated emission. The three radiative processes are shown in Fig 3.1. For simplicity, we consider an atom having two energy levels, an upper level E_2 and a lower level E_1. In addition the number of atoms N_1 at the energy level E_1 and N_2 at E_2 is constant. This means that every time the emission and absorption processes occur, it happens with a constant rate. In this way N_1 and N_2 will always remain unchangeable. Suppose that the atom in the lower level is exposed to radiation with photon energy $h\nu = E_2 - E_1$. The atom may then absorb radiation energy and undergo a transition to the upper level. This process is
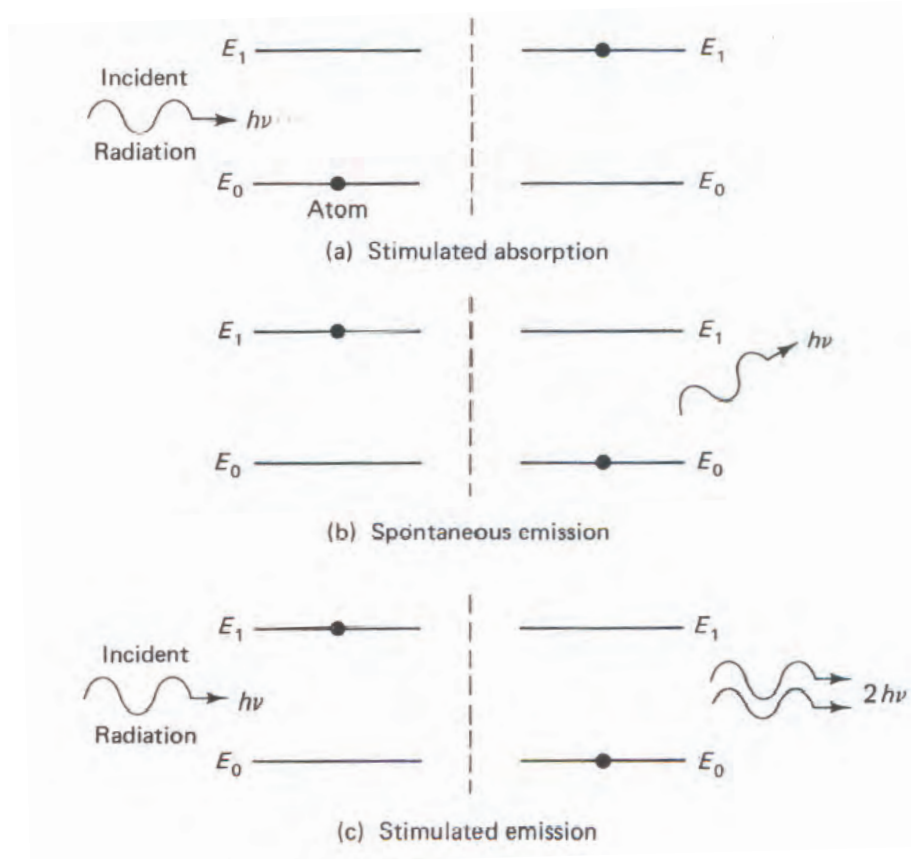
Figure 3.1: The three radiative processes: a) stimulated absorption, b) spontaneous emission and c) stimulated emission, that can occur between two energy levels and affect the passage of radiation through matter [27].

referred to as stimulated absorption. Very soon the atom, after being excited to an upper level E_2, will spontaneously fall down to the lower level E_1 and emit a photon of energy $h\nu = E_2 - E_1$ through the process of spontaneous emission. In the process of stimulated emission an atom in the upper level E_2 may also be stimulated to drop to a lower level E_1 and emit radiation with energy $h\nu = E_2 - E_1$ if exposed to a photon of resonant energy $h\nu = E_2 - E_1$. The resulting effect of this process is that besides the injected photon another photon is produced with the same energy and direction leading to an increase of the intensity of the incoming beam, hence the term light amplification of stimulated emission of radiation.

Stimulated emission is coherent, meaning that all the waves making the beam are in phase. This can be compared to a long column of soldiers walking in step. In contrast, spontaneous emission is incoherent, where all the decays occur in random directions and might be compared with the random movements in the streets.

Although the stimulated emission is a possible process when light interacts

with matter, it is unlikely in nature. This is because thermodynamic equilibrium prescribes that more atoms are in the lower level than in higher ones. This means that stimulated absorption is more likely to occur than stimulated emission.

3.1.2 Einstein's A and B coefficient

The three radiative processes are related mathematically. In the following it is assumed that the considered atoms (matter) in the assembly are in thermodynamic equilibrium with a black body radiation field. In addition the number of atoms N_1 at the energy level E_1 and N_2 at E_2 is constant. This means that every time the emission and absorption processes occur, it happens with a constant rate. In this way N_1 and N_2 will always remain unchangeable. Thus the mathematical expression for the three radiative processes is given by:

- **Spontaneous Emission (A_{21})** The transition from N_2 to N_1 leads to a rate decrease proportional with the population given by

$$\left(\frac{dN_2}{dt}\right)_{spont} = -A_{21}N_2.$$
(3.1)

  The index "21" indicates that the transition is from N_2 to N_1.

- **Stimulated Emission (B_{21})** The stimulated emission is given by

$$\left(\frac{dN_2}{dt}\right)_{stim} = -B_{21}N_2\rho(\nu).$$
(3.2)

  The factor $\rho(\nu)$ is the photon density since the process is stimulated by a radiation field (photons).

- **Absorption (B_{12})** Similarly holds for the absorption. Only is the process reversed, where the transition is from N_1 to N_2.

$$\left(\frac{dN_1}{dt}\right)_{abs} = -B_{12}N_1\rho(\nu).$$
(3.3)

Based on the above stated assumptions it follows that the rate of change of atoms in level E_2 is given by

$$\left(\frac{dN_2}{dt}\right) = 0 = -A_{21}N_2 - B_{21}N_2\rho(\nu) + B_{12}N_1\rho(\nu).$$
(3.4)

Furthermore we assume that the radiation field $\rho(\nu)$ has the spectral energy density of a black body radiation

$$\rho(\nu) = \frac{8\pi h\nu_3}{c^3}\frac{1}{e^{h\nu/k_B T} - 1},$$
(3.5)

and the atom population densities of the various energy levels, is distributed according to Boltzmann distribution at temperature T

$$\frac{N_2}{N_1} = e^{-(E_2 - E1)/k_B T} = e^{-h\nu/k_B T},$$
(3.6)

where ν is the frequency of radiation, c is the speed of light in vacuum, and k_B is the Boltzmann constant. Substituting eq. (3.5) for $\rho(\nu)$ in eq. (3.4) and inserting N_1/N_2 from eq. (3.6), eq. (3.5) is solved to give [27]:

$$\frac{A_{21}}{B_{21}} = 8\pi h\nu^3/c^3, \tag{3.7}$$

$$g_1 B_{12} = g_2 B_{21}, \tag{3.8}$$

where g_1 and g_2 are the statistical weights of the two states. The coefficient A_{21}, B_{21} and B_{12} are referred to as Einstein's coefficient. It should be noted that the stimulated emission coefficient B_{21} and the absorption coefficient B_{12} are equal only for the special case of non-degenerate energy levels

3.2   Population Inversion and Laser Threshold

Considering the case where $N_2 > N_1$ the stimulated emission rate will exceed the absorption rate. Otherwise, i.e. $N_2 < N_1$, absorption rate will exceed the stimulated emission. Since the Einstein relation states that $g_1 B_{21} = g_2 B_{12}$, we must ensure that $N_2 > N_1$ in order to increase the radiation field and get amplification or *gain*. This is the condition of *population inversion*, and is necessary to get laser action. Without it we do not have laser action. The factor $\sigma_{21}(N_2 - (g_2/g_1 N_1))$ is often referred to as the gain coefficient, where σ_{21} is the stimulated emission cross section.

   By increasing the pumping power the laser produces enough population in level 2 compared to level 1, because of the contribution of the stimulated emission to the decay in the active medium. Once the atom decays to the lower energy level it can be absorbed back to the upper energy level. And since the absorption rate equals the stimulated emission, the two rates will under the presence of a strong enough radiation field jump back and forth between E_1 and E_2, what corresponds to that the probability of being in the upper or the lower level is the same, that is a population equally distributed between the two energy levels, and hence $N_2 \sim N/2$ where $N = N_1 + N_2$. At this point the field is said to saturate the gain, *gain saturation*, because there is no longer enough atoms in level 2 to provide the additional gain. A further increase in the pumping power will thus not increase the population inversion but thereby result in an increase of the laser output intensity. However, a decrease of cavity photons will still occur in the laser cavity due to the loss effects such as; scattering, absorption radiation the mirrors [1] , absorption in the active medium and the useful output beam, the *out-coupling*. Thus, to ensure that the beam develops and thereby sustains laser oscillations, the gain is required to overcome the loss effects. This condition for oscillation is the laser threshold, and is depicted in Fig 3.2 as a bend on the curve. This curve also called the efficiency-curve is used to determine wether there is laser action or not as will be shown in in Section 7.

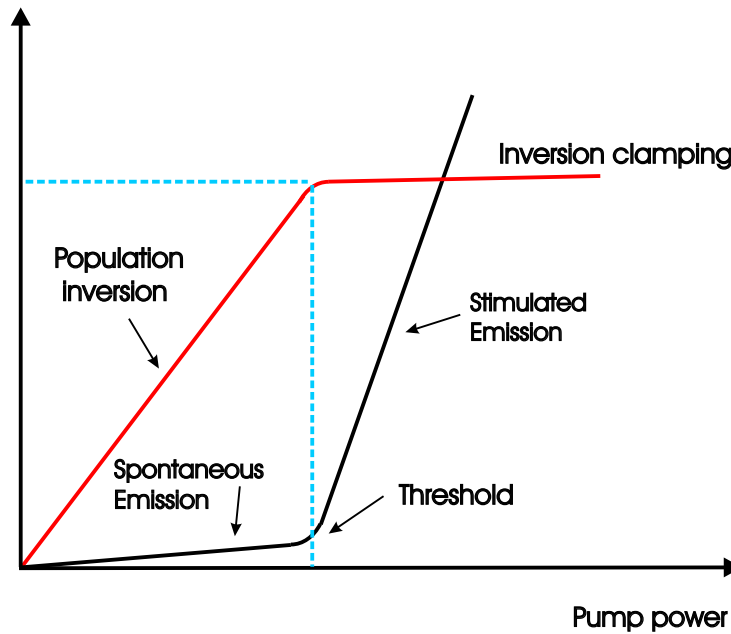[1]In our case the thin solvent surface.

Figure 3.2: Laser dye output versus the pump power (black curve) and population inversion (red curve). In the beginning of the operation the input energy (pumping) is increased increasing the population inversion (red curve) while the laser output is nearly zero (black curve). Only spontaneous emission (fluorescence) is the dominating radiative process. (As the stimulated emission contributes to decay, also spontaneous emission will do so in random directions within the active medium. At gain saturation, the spontaneous emission rate equals the stimulated emission.) The input energy keeps building up the cavity mode until the threshold is obtained (the bend on the black curve), and the gain saturates where the population inversion is no more occurring (flattening of the red curve). Exceeding the threshold by a further increase of the input energy, the modes begins to oscillate resulting in a linear increase of laser out put (black curve after threshold).

3.3 Essential Elements of a Laser

A laser device consists of three primary components: (1) an external energy source (a pump) supplying the amplifier with energy in order to provide stimulated emission, (2) a gain or amplifying medium, where stimulated emission occurs (an active medium), and (3) finally a set of reflecting components (usually mirrors) to feed back the light into the amplifier for continued growth of the beam intensity (a cavity or resonator).

3.3.1 The Pump

The pump is the external energy source utilized to achieve a sufficient pumping flux and thereby create a population inversion between the two energy levels in the laser medium.

Different pumping techniques can be used such as optical, thermal, and chemical. In this project the optical pumping is used by focusing the light on

the laser medium at an appropriate wavelength so that the most of the pumped light can be absorbed by the laser media and thereby pump the atom to the highest energy level. The choice of the optical pump depends on the absorptions wavelength of the laser medium, since the wavelength region of the two must be coincident. Add to this that the absorption wavelengths must be sufficient in order being able to excite (pump) the atom into its highest energy level. The optical pumping requires a quit intense pumping source. We use the Nd:YAG (neodymium:yttrium aluminium garnet) laser as an optical pump and an organic laser dye medium as the active medium.

3.3.2 Dye Laser as The Active Medium

The laser medium is the region in which the stimulated emission occur and thereby amplification of the incoming light signal. It is the responsible part of a laser for the support of the "unnatural" condition of population inversion between the two energy levels of laser atoms.
The laser medium can be gaseous, solid or liquid. As mentioned above, an organic dye is used as the active laser medium in this project.

One of the main reasons that makes the dye laser highly attractive and much sought after in the world of scientific research is the property having a tunability over a wide spectrum that covers a wavelength region from app. 400 nm to 900 nm for each dye and having a laser bandwidth in the order of 30-50 nm; Fig 3.3. Dyes are large molecules with a complex structure and comes under families
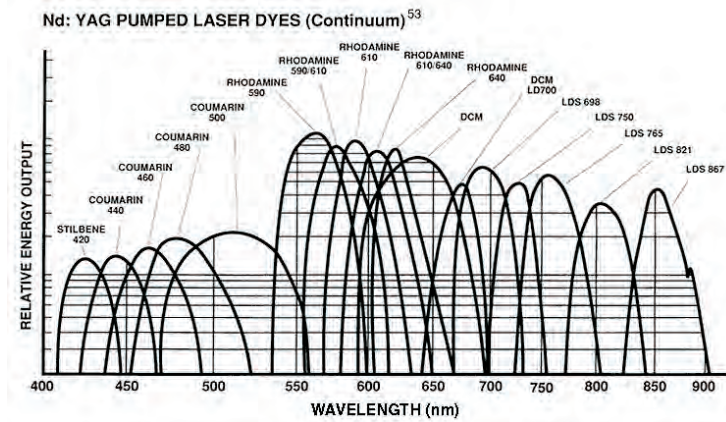
Figure 3.3: The tuning curves of a typical range of dyes [34].

having the same chemical structure. The members of this family differs from each other by having different end-groups sitting on the outer edge. It is these differences that determines the tuning range, the laser emission wavelength and absorption. In this project the dye Rhodamine 6G (Rh6G) is used, see Fig 3.4. Rh6G belongs to the Xanthene dye family. A dye can be used in liquid, solid or gas. But since the liquid has some advantage compared to gas and solid, it is used as a laser gain media. They are more cheaper to fabricate, easier to cool down and they have a higher density of the active atoms than gas. Besides, their

Figure 3.4: The chemical structure for Rh6G [33].
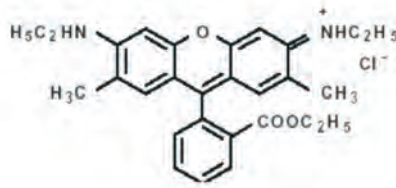
output power is the same as the semiconductors; i.e. relatively high. Thus, by
an organic dye laser we understand a dye laser consisting of solvent material into
which is mixed a laser dye molecules. As regards the solvent material, different
forms of liquid can be used such as water, ethanol or ethylene glycol (EG). Since
we are interested in forming a usable droplet we firstly require a dye solvent with
a low evaporation rate and secondly a solvent having a relatively low polarity,
in order for the laser dye to retain a high quantum yield [2]. EG was found to
fulfill these criteria why it was chosen as a dye solvent, since an ethanol droplet
was observed to evaporate immediately after placement on a surface, and the
water was by D. Magde *et al.* [33] reported to have the lowest quantum yield,
namley $\phi = 0.90$. EG is normally also used when operating with a flowing jet
solution because it is viscous and thereby maintains an optically flat surface.

In our case, the powdered Rh6G is mixed into EG. Rh6G is strongly fluores-
cent, meaning that it absorbs radiation in certain wavelength band and emits
radiation in another wavelength band displaced towards longer wavelengths.
The displacement is due to the energy loss (as heat) during the optical pumping
process. Fig 3.5 shows the absorption and emission spectra for Rh6G dissolved
in ethanol [3].

It emerges that Rh6G has an absorption maximum at 532 nm, why it is
convenient to utilize the Nd:YAG with the wavelength 532 nm as the optical
pump. However, the emission maximum for Rh6G dissolved in EG is around 580
nm. For Rh6G dissolved in ethanol the emission maxima is displaced towards
higher wavelengths due to the so-called solvent tuning [33].

3.3.3 The Resonator

The resonator is as essential a part of a laser as the laser medium. Seemingly,
it sounds sufficient with a population inversion to produce laser. However,
the most useful laser characteristics, such as monochromaticity, coherency and
directionality, originate from the oscillation of light inside a cavity.

A resonator is an optical device providing what is called a positive feedback
that concentrates the stimulated emission in a beam and oscillates it back and

---

[2]The quantum yield is the number of defined events which occur per photon absorbed by
the system. The integral quantum yield is $\phi = \dfrac{\text{number of events}}{\text{number of photons absorbed}}$

[3]Because of the lack of EG data as solvent, and because the gain curve for Rh6G dissolved
in ethanol and methanol are approximately similar, we assume that the gain curve for Rh6G
dissolved in EG do not deviate considerable significantly from ethanol and methanol (In that
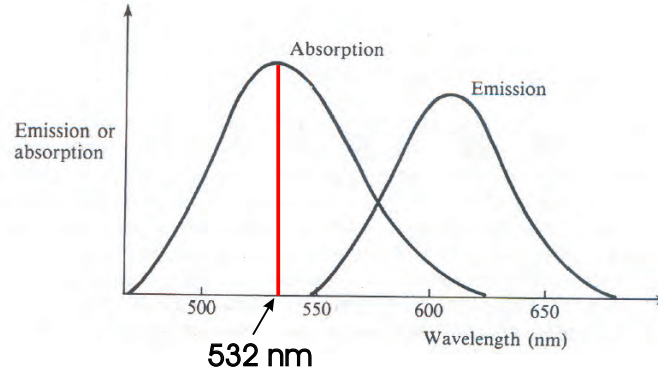way, not said that this is not a concern).

Figure 3.5: Absorption and emission curves for Rh6G in ethanol [29]. The red line is added by the author.

forth in the medium. Without it the stimulated emission will be lost in all different directions and no laser action will thus occur.

Normally, the resonator consists of two reflecting mirrors of which the one has a reflectivity of 100% and the other a bit less than 100% allowing a small part of the collimated light to escape the laser medium. The escaped light is indeed the laser beam.

However, the resonator created in this project looks differently; the reason why this project is unique. In our case, the liquid-air surface of the created droplet serves as a mirror providing the optical feedback at selected wavelengths to the morphology-dependent resonances of a spherical droplet. Here, the differences of the refractive index for air and EG is utilized. A small portion of the trapped light in the droplet will escape (laser beam), and thus we have a liquid dye laser. A more comprehensive description and detailed treatment of this spherical formed resonator will be carried out in the following chapter.

3.4   Laser Operation

So far we have only considered the radiative processes to occur in a simplified system namely the two-level laser scheme. However, this is not the whole truth. Although the laser transition process does occur between two energy levels, a refined energy level system that gives a more accurate description of the laser operation is required. The problem which we encounter in the two-level model is that using the pumping mechanism to excite the atoms ends also de-exciting them. For example, if the atom is pumped from level 1 to level 2 we will cause both the absorption and stimulated emission.

A qualified alternative is to consider a four-level laser scheme for achieving population inversion, as shown in Fig 3.6.

The laser media is supplied by a pump energy amount sufficient to excite the atoms from the ground state to the energy level E_3. Hereafter, an extreme rapid spontaneous decay occurs from E_3 to the upper laser level E_2. Since more and more atoms will decay to E_2 their number N_2 will increase. These can decay to E_1. E_1 is not the ground state but an excited state labelled the lower laser

level. The idea by introducing an E_1 is that the atoms from here can decay to the ground state E_0 and in this way reduce the number of atoms N_1 in E_1, obviously resulting in an enhancement of the population inversion; $N_2 > N_1$. Thus, an incident photon with energy $h\nu = E_2 - E_1$ will stimulate an emission between E_2 and E_1 and thereby leading to laser amplification.
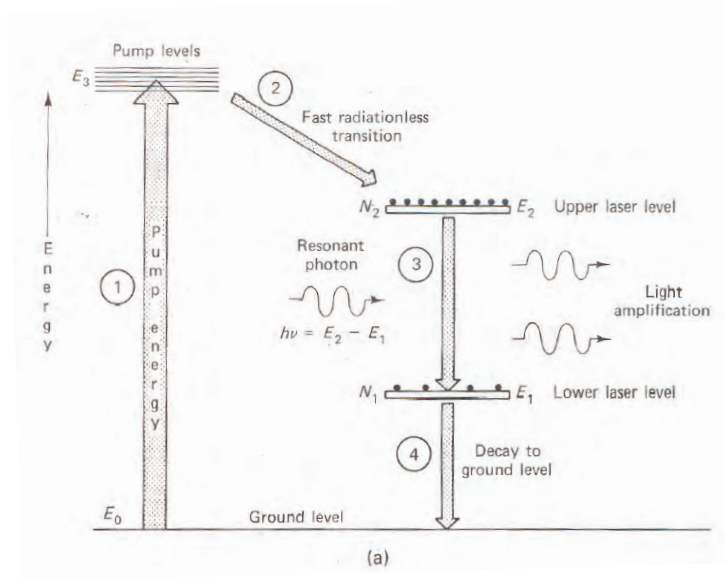

Figure 3.6: A schematic diagram showing a general four-level laser system [27].
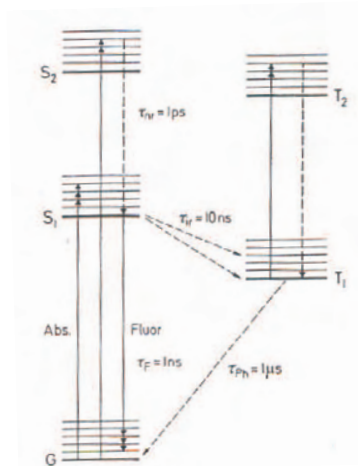

Figure 3.7: Energy-level scheme for a typical dye laser. The electronic energy levels (groups of lines) contain vibrational (dark lines) and rotational (light lines) substates [3].

However the broad absorption and emission spectra for Rh6G, Fig 3.5, and generally for all dye lasers, may be interpreted differently in terms of transitions between the electronic band level, where each electronic level is a large number of sub-levels and is associated to a set of vibrational and rotational energy levels, i.e. homogeneously broadening.

Fig 3.7 shows the typical energy level diagram for a dye laser. The picture is somewhat differently from the previous, however, by the existence of two systems of bands designated "singlet" and "triplet". Yet, the principle remains the same in the two pictures. In a singlet the total spin state of the molecule is zero and for triplet states it is unity [4]. The symbols S_0, S_1, S_2 refer to the singlet bands and T_1, T_2 to the triplet bands. Only transitions between $S \leftrightarrow S$ and $T \leftrightarrow T$ are allowed. The radiative transitions between $S \leftrightarrow T$ are forbidden [5] according to Quantum Mechanics. To begin with we consider only the $S \leftrightarrow S$ transitions. The energy that drives the dye laser comes from the external pump, elevating from the ground state S_0 to states near the top of the first excited singlet electronic state S_1. The $S_0 \rightarrow S_1$ transition covers a wide wavelength range because the vibrational-rotational levels associated to S_0 and S_1 are also wide, why the absorption spectrum is wide for dye lasers, and particulary for Rh6G. The excited molecule rapidly relaxes to states at the bottom of this band. The decay process is non-radiative. Lasing action can then take place between the bottom state of S_1 and those near the top of S_0. The distance between the top and the bottom in the ground state S_0 is sufficient to retain the top of S_0 almost empty in room temperature and the grove four-levels laser scheme is thus obtained.

The $S_1 \rightarrow S_0$ transition is very rapid (~ 10 ns), why it is necessary with an intense pumping to achieve population inversion. As regards the triplet states, these causes troubles, unfortunately. Although $S \leftrightarrow T$ transitions are forbidden, they still occur. The decay $S_1 \rightarrow T_1$ reduce the amount of molecules in the upper level. And since $T_1 \rightarrow S_0$ is also forbidden, while $T_1 \rightarrow T_2$ is strongly allowed, means that once a significant amount molecules have found their ways into the triplet states they are trapped and cannot contribute to laser emission. Also the lifetime in the triplet $T_1 \leftrightarrow T_2$ is too long (microseconds). Operating with pump pulses in the 10 ns range or shorter are too short to produce triplets, the reason why we pump (by means of Nd:YAG laser) with a pulse duration of 5 ns. Pulsing will also prevent (or reduce) the dye laser of bleaching, since this gets bleached by thermal heating during continuous pumping.

3.5   Multi-mode Laser Oscillation

An effect within the cavity, because of its dimension, that plays a decisive role in determining laser characteristics are laser modes. Generally speaking light modes are the possible standing electromagnetic waves that can exist in a system. These waves are defined as the solutions to the Maxwell's equations, and will be reviewed in the following chapter, Chapter 4. Thus, the cavity modes are the modes existing within the cavity.

Ideally the light emitted by a laser is said to be monochromatic, e.i oscillating

---

[4]The total spin quantum number S for a level is $(2S+1)$-fold degenerate. Hence, the names singlet ($2S+1=1$) and triplet ($2S+1=3$) [31].

[5]Actually, these transitions are not strictly forbidden but less likely than the allowed [31].

on a single mode (a distinct wavelength). However, the resultant radiation is hardly monochromatic, as we know. In the case of dye lasers, these has a homogeneously broadened gain medium where generally many cavity modes oscillates, e.i. multi-mode oscillation.

Laser modes covers a broad spectral range in the form of discrete wavelength components closely spaced. The broad covered spectral range is approximatively the fluorescence spectrum. Thus, a given mode can only oscillate if there is gain in its respective wavelength area, and only when the gain exceeds the loss. This is shown in Fig 3.8. Estimating the number of possible lasing modes is done
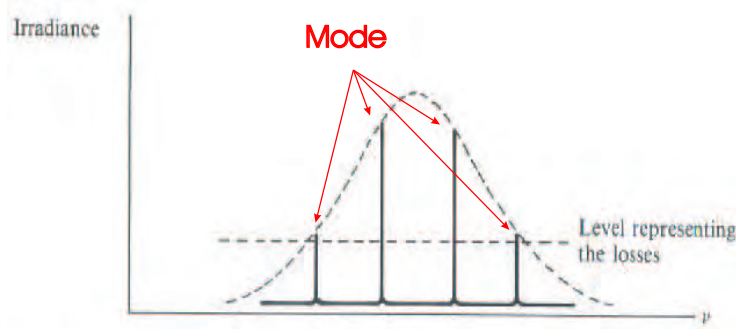

Figure 3.8: Cavity modes (marked in red and added by the author) lying under the gain profile exceeding the losses [29].

by counting the number of cavity modes, separated by $\Delta\nu = c/n_{eg}L$ lying in the gain bandwidth $\Delta\nu_g$. Expressed in terms of wavelength ($\lambda = c/\nu$), this translates to

$$\Delta\lambda = \frac{\lambda^2}{n_{eg}L} \tag{3.9}$$

where L is the distance travelled by the mode inside the cavity and n_{eg} is the refractive index of EG. In our case, $L = 2\pi R$, since we assume the mode to travel around the circumference of the droplet. R is the radius of the droplet. The number of the modes is of the order $\Delta\lambda_g/\Delta\lambda$ for $\Delta\lambda_g > \Delta\lambda$.

Expressing a wish of reducing the number of the possible modes within the gain profile, or even to reach single-mode oscillation, in that case, it is obviously from the above mentioned expression, that the cavity has to be smaller and thereby a reduce of the radius of the droplet. Otherwise the pumping rate has to allow only one mode to reach threshold as shown in Fig 3.9. A disadvantage of the first way is that we end having a small gain cell and consequently a low output power.
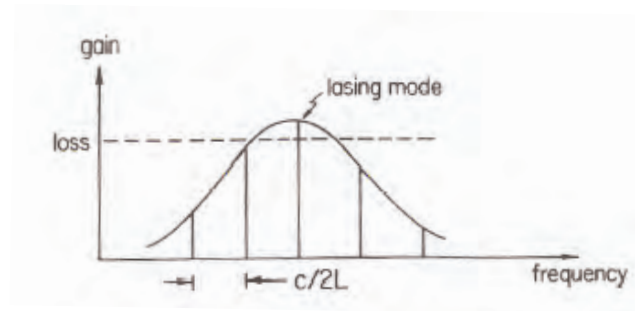
Figure 3.9: Several modes lying under the gain curve, but only one can lase [31].

Chapter 4

The Resonator Model

In this chapter the actual considered resonator is presented followed by a short introduction to the concept of Whispering Gallery Modes. Subsequently, a theoretical model and a numerical analysis of a dielectric sphere is given.

4.1 Introduction to The Spherical Droplet Resonator

The liquid droplet dye laser project takes a rotational symmetric hemispherical liquid droplet resonator as a starting point. As mentioned before, the droplet consists of the laser dye Rh6G dissolved in EG and was deposited by a dip pen method on suitable hydrophobic surfaces; a more detailed description will follow in Chapter 6. Hereafter, the droplet was optically pumped (at 532 nm) with a frequency doubled Nd:YAG laser. Unlike the conventional laser resonators, where two mirrors for instance amplify the light inside the cavity by reflecting it back and forth, the droplet, in our case, forms a self-organized hemispherical laser cavity, relying on reflections at the liquid-air and liquid-substrate interfaces. Since the used substrate is silicon, the refractive index for this is $n_{\mathrm{si}} \approx 4$. This resonant behavior, commonly observed as the ripple structure in elastic scattering resonances, is referred to as morphology dependent resonances, or Whispering Gallery Modes (WGMs).

Although we in fact work on a hemispherical formed liquid droplet, we will consider a problem of high symmetry theoretical treatment of the electromagnetic modes, namely a shielded homogenous and isotropic spherical dielectric resonator.

This I will do partly because it is simpler to study mathematically, partly because there are countless literature dealing with this case. Incidentally, it was the projects main purpose to create a perfect spherical formed droplet, for which reason it is also appropriate to consider the spherical resonator. Nevertheless, after the theoretical treatment, a qualitative comparison between the above-mentioned resonator and our actual liquid droplet resonator is carried out.

The strategy is as follows. In Section 4.2 we shortly introduce the concept of WGMs. In the following, Section 4.3, a theoretical electromagnetic analysis

model of the shielded homogenous and isotropic dielectric sphere is presented. This is based on Maxwell's equations, and has the aim to determine the resonance modes represented in eigenmodes. In Section 4.4 numerical electromagnetic analysis of the same sphere as in Section 4.3, is carried out by using the simulation program, FEMLAB. Here, the possible resonance modes are tried simulated and the results discussed.

4.2 Whispering Gallery Modes

History of The Whispering Gallery

At the end of the 1870'ies, Lord Rayleigh carried out the first studies of the observed acoustic waves clinging to the dome of St. Paul's Cathedral, in London. He observed that a whisper close to the edge of the inner side of the dome could be heard relatively easy by a person standing at the opposite side along the vault , hence the name "Whispering Gallery". But a person standing in the center of the dome would not be able to hear the whispering. The explanation for this phenomenon is that the dome functions as an exclusive acoustic conduit resulting in a travel of the sound waves only along the edge of the vault. Thus, the observations of Lord Rayleigh characterizes the wave propagation in Whispering Gallery Modes (WGMs); where the energy of the signal is concentrated in a local area along the edge where the propagation takes place.

Contrary to the acoustic longitudinal waves, the electromagnetic propagation is treated in transverse waves; but where the characterizing properties for WGMs still is preserved. Thus, the WGMs are defined as electromagnetic resonances travelling in a dielectric medium of circular symmetric structures, such as circular rods, microdisks [36], [37] and liquid microspheres, in our case.

Geometric Optics Picture - Heuristic model

For ideal micropheres, it is informative to consider the confinement of WGMs in a heuristic way, using the geometric optics picture. If we consider a microsphere of radius R with refractive index n_{ref}, the WGM can be viewed as light rays that, once within the spherical particle, intersect repeatedly with the interface with angle of incidence θ_{in} beyond the critical angle θ_{c}, undergoing total internal reflection only if $\theta_{\text{in}} > \theta_{\text{c}} = \arcsin(1/n_{\text{ref}})$. See Fig 4.1(a).

For an EG droplet with refractive index n_{eg}=1.43, the critical angle is given by 44.33°. For large microspheres ($R \gg \lambda$), WGMs are trapped rays that circulates near to the droplet interface, and traverses a distance $\approx 2\pi R$ in one round trip. If one round trip is exactly an integer number n of wavelengths circulating in the medium, then a standing wave occurs as shown in Fig 4.1(b).

(a) The ray totally reflected.

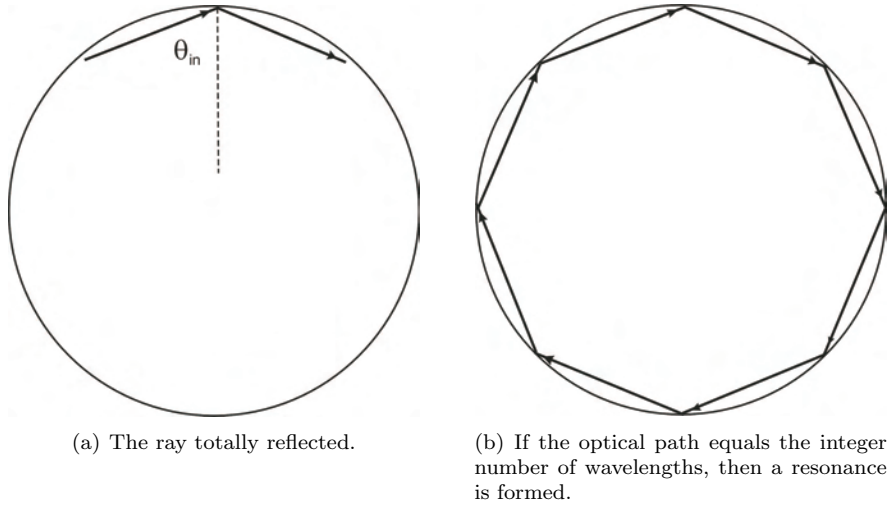(b) If the optical path equals the integer number of wavelengths, then a resonance is formed.

Figure 4.1: Total reflection within the sphere resulting in resonance.

This condition translates into

$$2\pi R \approx n(\lambda/n_{\text{ref}}), \tag{4.1}$$

where λ/n_{ref} is the wavelength in the medium. It is convenient to define a so-called dimensionless size parameter X, for the discrete wavelengths which commensurate with WGMs within a droplet. This is defined as

$$X = \frac{2\pi R}{\lambda}, \tag{4.2}$$

and depends on the shape and the refractive index, n_{ref}, of the droplet. Thus, the resonance condition is

$$X \approx n/n_{\text{ref}}. \tag{4.3}$$

The integer n, originally introduced as the number of wavelengths in the circumference, can be compared to the angular momentum of a circulating photon, se Appendix B. So, the physical interpretation of the mode number is that it describes the angular variation of the internal mode intensity. The mode intensity is given by $|\mathbf{E}|^2$ where $\mathbf{E}$ is the amplitude of the electric field. The mode-spacing in this case would precisely be given by the expression derived in Section 3.5, eq. (3.9):

$$\Delta\lambda = \frac{\lambda^2}{2\pi n_{\text{eg}} R}. \tag{4.4}$$

We have so far referred only to the mode number. In addition, there is also the radial variation indicating the number of the radial maxima in the mode distribution. This can be characterized by the radial mode order l. If we assume a first order resonance, $l = 1$, the value of the mode number will be of the order $n_{\text{ref}} X$. This can be written as

$$n\frac{\lambda}{n_{\text{ref}}} = 2\pi R. \tag{4.5}$$

34

Each WGM has a $(2n + 1)$ azimuthal mode degeneracy. This azimuthal mode, illustrated in Fig 4.2, is designated by m, with mode $m = n$ lying on the equatorial plan. The azimuthal mode can also be compared to the z component of the angular momentum for a circulating photon; Appendix B.

Figure 4.2: The azimuthal mode [41].

Thus, in summary, an individual WGM can be identified in terms of three mode numbers (l, m, n) representing together the radial, equatorial, and polar electromagnetic field components. The radial part, for a WGM in a sphere, can be described by spherical Bessel functions, while the polar -longitudinal- field dependence follows spherical harmonics, and the equatorial -latitudinal- field variation is sinusoidal. In a perfect sphere form, whispering gallery mode frequencies are determined only by n and l. That is because for the radial and equatorial mode, they correspond to different distances light must travel in order to complete a resonant path around the sphere, and hence, different frequencies [40].

Example

(a) Intensity distribution for a WGM with $n = 60$ and $l = 2$ for a droplet [41].

(b) Influence of mode order on radial field [41].

Figure 4.3: The concept of modes.

35

For a better understanding of the concepts of mode number and mode order, we illustrate it by considering the following example given by R. Symes *et al.* [41]. A WGM has the mode number $n = 60$, and the order mode $l = 2$. The distribution of the mode intensity is shown in Fig 4.3(a). The variation of the mode order is illustrated in Fig 4.3(b). It is clear that the mode order increases for a further penetration of the WGM in the droplet. The intensity of WGM becomes insignificant for a penetration depth of $\sim R/n_{\text{ref}}$. This suggests that this is the closest distance a ray can reach to sustain the internal reflection.

4.3 Analytical Model for Modes in A Sphere

In this section a mathematical model for the resonator will be derived. More specifically I compose an electromagnetic theoretical analysis of a homogeneous and isotropic dielectric sphere, based on Yadav *et al.* [38] to describe the optical whispering gallery modes occurring at the liquid-air interfaces inside the dielectric droplet. Due to the spherical form of the droplet only spherical coordinates are considered in this section.

The Macroscopic Maxwell's equation

All electromagnetism is governed by the four Maxwell's equations

$$\nabla \cdot \mathbf{D} = \rho_f, \tag{4.6}$$

$$\nabla \cdot \mathbf{B} = 0, \tag{4.7}$$

$$\nabla \times \mathbf{E} = \frac{\partial \mathbf{B}}{\partial t}, \tag{4.8}$$

$$\nabla \times \mathbf{H} = \frac{\partial \mathbf{D}}{\partial t} + \mathbf{J}, \tag{4.9}$$

where $\mathbf{E}$ and $\mathbf{H}$ are the macroscopic electric and magnetic fields, respectively. $\mathbf{B}$ is the magnetic induction field, $\mathbf{D}$ is the electric displacement, ρ_f is the free charge and $\mathbf{J}$ is the volume current density.

Electromagnetism in dielectric media

Since we consider, in this specific case, a propagation within a dielectric medium, with neither charges nor currents, we can set $\rho_f = \mathbf{J} = 0$. Furthermore, we are interested in relating $\mathbf{D}$ to $\mathbf{E}$ and $\mathbf{B}$ to $\mathbf{H}$. The components D_i of the displacement field $\mathbf{D}$ are usually related to the components E_i of the electric field $\mathbf{E}$ via the power series [39]:

$$D_i = \Sigma_j \epsilon_{ij} E_j + \Sigma_{j,} k \chi_{ijk} E_j E_k + O(E^3) \tag{4.10}$$

Considering a dielectric medium we assume the following:

1. The field strengths are small enough so that we are in the linear region, why we ignore χ and all the higher terms.

2. The material is isotropic, so that $\mathbf{E}(\mathbf{r}, \omega)$ and $\mathbf{D}(\mathbf{r}, \omega)$ are related by a scalar dielectric constant $\epsilon(\mathbf{r}, \omega)$.

3. We focus only on low-loss dielectrics, which means we can treat $\epsilon(\mathbf{r})$ as purely real.

Thus we have $\mathbf{D}(\mathbf{r}) = \epsilon(\mathbf{r})\mathbf{E}(\mathbf{r})$. For most non-magnetic dielectric materials, the magnetic permeability is very close to unity, e.i. $\mu_r \simeq 1$. The relation between the Auxiliary field vectors $\mathbf{D}$, $\mathbf{E}$ with $\mathbf{B}$ and $\mathbf{H}$ are then given by the constitutive relations

$$
\begin{aligned}
\mathbf{D} &= \varepsilon(\mathbf{r})\mathbf{E} = \varepsilon_0 \varepsilon_\mathbf{r} \mathbf{E}, & (4.11) \\
\mathbf{B} &= \mu_0 \mu_r \mathbf{H} = \mu_0 \mathbf{H}, & (4.12)
\end{aligned}
$$

where μ_0 and ϵ_0 are respectively the permeability and permittivity of the free space.

Time dependent E and H field

Now, we consider time dependency of $\mathbf{E}$ and $\mathbf{H}$. Here we make use of the standard method, assuming that the variation is periodic with time. We introduce the assumption:

$$
\begin{aligned}
\mathbf{H}(r, \theta, \phi; t) &= \mathbf{H}(r, \theta, \phi)e^{j\omega t}, & (4.13) \\
\mathbf{E}(r, \theta, \phi; t) &= \mathbf{E}(r, \theta, \phi)e^{j\omega t}. & (4.14)
\end{aligned}
$$

$\omega = 2\pi\nu$ where ν is the frequency of the fields. Eq. (4.13) results in the following simple time derivatives (symbolized with a dot:$\cdot$)

$$
\begin{aligned}
\dot{\mathbf{H}} &= j\omega \mathbf{H}, & (4.15) \\
\dot{\mathbf{E}} &= j\omega \mathbf{E}. & (4.16)
\end{aligned}
$$

Using the constitutive relations, eq. (4.11), the Maxwell's equations, eq. (4.6) reduce to

$$
\begin{aligned}
\nabla \cdot \mathbf{E} &= 0, & (4.17) \\
\nabla \cdot \mathbf{H} &= 0, & (4.18) \\
\nabla \times \mathbf{E} &= -j\omega \mu_0 \mathbf{H}, & (4.19) \\
\nabla \times \mathbf{H} &= -j\omega \varepsilon_r \varepsilon_0 \mathbf{E}. & (4.20)
\end{aligned}
$$

Using the expression for the curl in spherical coordinates, we get eq. (4.19) and eq. (4.20) to

$$
\nabla \times \mathbf{E} = \frac{1}{r} \begin{pmatrix} \frac{1}{\sin\theta}\left[\frac{\partial \sin\theta E_\phi}{\partial\theta} - \frac{\partial E_\theta}{\partial\phi}\right] \\ \frac{1}{\sin\theta}\frac{\partial E_r}{\partial\phi} - \frac{\partial r E_\phi}{\partial r} \\ \frac{\partial}{\partial r}(rE_\theta) - \frac{\partial E_r}{\partial\theta} \end{pmatrix} = -j\omega\mu_0 \begin{pmatrix} H_r \\ H_\theta \\ H_\phi \end{pmatrix}, \qquad (4.21)
$$

$$
\nabla \times \mathbf{H} = \frac{1}{r} \begin{pmatrix} \frac{1}{\sin\theta}\left[\frac{\partial \sin\theta H_\phi}{\partial\theta} - \frac{\partial H_\theta}{\partial\phi}\right] \\ \frac{1}{\sin\theta}\frac{\partial H_r}{\partial\phi} - \frac{\partial r H_\phi}{\partial r} \\ \frac{\partial}{\partial r}(rH_\theta) - \frac{\partial H_r}{\partial\theta} \end{pmatrix} = -j\omega\varepsilon_0\varepsilon_r \begin{pmatrix} E_r \\ E_\theta \\ E_\phi \end{pmatrix}. \qquad (4.22)
$$

These six equations describe completely the electric and the magnetic field. Now taking the curl of eq. (1.18) we get

$$\nabla \times (\nabla \times \mathbf{E}) = -j\omega\mu_0(\nabla \times \mathbf{H}). \qquad (4.23)$$

Using the vector identity, $\nabla \times \nabla \times \mathbf{V} = \nabla(\nabla \cdot \mathbf{V}) - \nabla^2\mathbf{V}$, eq. (4.23) can be rewritten as

$$\nabla(\nabla \cdot E) - \nabla^2\mathbf{E} = -j\omega\mu_0(\nabla \times \mathbf{H}). \qquad (4.24)$$

Using eq.(4.17) (the divergence condition $\nabla \cdot \mathbf{E} = 0$) and eq. (4.20) we get

$$(\nabla^2 + \mu_0\varepsilon_0\varepsilon_r\omega^2)\mathbf{E} = 0. \qquad (4.25)$$

Similarly, we get for the magnetic field

$$(\nabla^2 + \mu_0\varepsilon_0\varepsilon_r\omega^2)\mathbf{H} = 0. \qquad (4.26)$$

TE and TM modes

We distinguish between two types of WGM solutions: The E_{TE} and H_{TM} solutions, called the transverse electric (TE) mode and the transverse magnetic (TM) mode, respectively, because they are both tangent to the spherical surface.

In the following, only the electric fields for the TE modes will be determined by using the standard theory. We are interested in expressing the vector field $\mathbf{E}$ in terms of three components: the radial (E_r), meridional (E_θ), and azimuthal (E_ϕ) components. However, the Laplacian of $\mathbf{E}$ will result in three differential equations each containing the three $\mathbf{E}$-components. For TE mode the following condition is satisfied

$$\mathbf{r} \cdot \mathbf{E} = 0, \qquad (4.27)$$

meaning that $\mathbf{r} \perp \mathbf{E}$. The electric field can be written in terms of the gradient of some scalar function ψ as:

$$\mathbf{E} = \mathbf{r} \times \nabla\psi. \qquad (4.28)$$

Eq. (4.28) satisfies condition (4.27), [1] and the scalar function satisfies the Helmholtz equation (C.3) given by

$$(\nabla^2 + k^2)\psi = 0, \qquad (4.29)$$

where $k = \omega\sqrt{\epsilon_r\epsilon_0\mu_0}$ is a constant. Using the solution of ψ determined in Appendix C (eq. (C.14)) as

$$\Psi(r, \theta, \phi) = \frac{A}{\sqrt{r}}J_{n+(1/2)}(kr)P_n^m(\cos\theta)\cos m\phi, \qquad (4.30)$$

and inserting the expression of the gradient, $\nabla\psi$, in the spherical polar coordinate system given by

$$\nabla\psi = \frac{\partial\psi}{\partial r}\hat{\mathbf{r}} + \frac{1}{r}\frac{\partial\psi}{\partial\theta}\hat{\theta} + \frac{1}{r\sin\theta}\frac{\partial\psi}{\partial\phi}\hat{\phi} \qquad (4.31)$$

---

[1] Inserting eq.(4.28) into eq.(4.27) we have: $\mathbf{r} \cdot (\mathbf{r} \times \nabla\psi) = 0$. Using the vector identity $\mathbf{A} \cdot (\mathbf{B} \times \mathbf{C}) = \mathbf{A} \times (\mathbf{B} \cdot \mathbf{C})$ we get $(\mathbf{r} \times \mathbf{r}) \cdot \nabla\psi = 0$. Since $\mathbf{r} \times \mathbf{r} = 0$ it is by this shown that eq.(4.28) satisfies condition (4.27).

in eq. (4.28) we can determine the components of the electric field as

$$E_r \quad = \quad 0, \tag{4.32}$$

$$E_\theta \quad = \quad \frac{Am}{\sqrt{r}\sin\theta} J_{n+(1/2)}(kr) P_m^n(\cos\theta)\sin m\theta, \tag{4.33}$$

$$E_\phi \quad = \quad \frac{A}{\sqrt{r}} J_{n+(1/2)}(kr) \frac{d}{d\theta}\big\{ P_m^n(\cos\theta)\big\}\cos m\theta. \tag{4.34}$$

Characteristic equations for the TE modes

Having determined the electric field expression for the TE mode, we can derive the eigenvalue equations for these modes employing the boundary conditions. On the metal surface, i.e. $r = R$, the electric field satisfies the boundary conditions, that the tangential components of $\mathbf{E}$ are zero for all θ and ϕ, hence, for the TE modes we get from eqs. (4.33) and (4.34)

$$J_{n+(1/2)}(kr)\mid_{r=R} = 0. \tag{4.35}$$

Eq.(4.35) is the eigenvalue equation for the TE modes. Solving eq. (4.35) gives the value of $kR = x_{nl}$ as

$$x_{nl} = kR = \frac{2\pi n_{\text{ref}}R}{\lambda} \tag{4.36}$$

where λ is the wavelength in the dielectric at which the resonator oscillates (in our case emits radiation) in the appropriate mode.

The first 4 roots of x_{nl}^2 satisfying eq. (4.35) for $n = 1 - 4$ and $l = 1 - 4$, are given in Table 4.1. It is worthy of note that the roots shown in table does not take into the consideration the degeneracy $m = 2n + 1$.

			l		
n	0	1	2	3	4
1	π^2	20.1907	33.2175	48.8312	66.9543
2	$4\pi^2$	59.6795	82.7192	108.516	137.005
3	$9\pi^2$	118.9	151.855	187.636	226.192
4	$16\pi^2$	197.858	240.703	286.409	334.936

Table 4.1: The table showing the first four roots of x_{nl}^2 satisfying eq. (4.35) for $n = 1 - 4$ and $l = 1 - 4$. The degeneracy m is not taken into consideration.

Calculating the mode-spacing

As the name indicates, mode-spacing is the separation distance between adjacent modes, i.e. between two peaks, lying under the gain curve. And since we are operating with three mode types, the separation distance can be between n, l or m. But since the m mode does not influence the frequency and thereby the energy, this can be neglected.

However, because of the merging and the degeneracy of the three mode types, we can in no way by means of measurements detect which peak belongs to which one of the three mode types. Only the energy (wavelength) can be

detected. The eigenvalues have to be plotted for all modes before anything can be said about the mode-spacing.

The liquid droplet dye laser with radius R emits light at the wavelength interval $[\lambda_1, \lambda_2]$, which by use of eq. (4.36) corresponds to the eigenvalue range $[x_1, x_2]$. By plotting the eigenvalues x_{nl} versus all their respective mode types n and l, an asymptotic behavior of the graph Δx will be observed in the interesting eigenvalue range $[x_1, x_2]$. A relation between Δx and the mode-spacing $\Delta\lambda$ is given by determining $\partial x/\partial\lambda$. By differentiating the eigenvalue equation. (4.36) with respect to λ we get

$$\frac{\partial x}{\partial \lambda} = -\frac{2\pi n_{\mathrm{eg}} R}{\lambda^2} \tag{4.37}$$

And since we are interested in relating the mode-spacing $\Delta\lambda$ to Δx, eq. (4.37) can be rewritten to express the mode-spacing

$$\Delta\lambda = \frac{\lambda^2}{2\pi n_{\mathrm{eg}} R}\Delta x. \tag{4.38}$$

By choosing λ as the wavelength of a mode in the lasing regime, the neighboring mode is then separated by $\Delta\lambda$ given by eq. (4.38). It should be noted that the only difference between eq. (4.38) and eq. (4.4) is Δx. This is because eq. (4.4) only operates with one mode type for which $\Delta x = 1$, whereas we in our case, eq. (4.38), operates with three different mode types (or rather two mode types), manifested in Δx. By plotting the eigenvalues x_{nl} versus their respective modes n and l, the slope of the asymptote of the graph was determined to $\Delta x = 3.4$ as shown in Fig 4.4. In Table 7.5, the two mode-spacing expression eq. (4.38) and eq. (4.4) are compared for four droplet radii: 150 μm, 270 μm, 330 μm and 600 μm, in the wavelength range 570-616 nm (lasing regime for the dye droplet). However, only the mode-spacing given by eq. (4.38) will be compared to the measured results. From Table 7.5, it appears that the mode-spacing decreases for increasing sphere radii, which is in agreement with the expected and the discussed in Sec. 3.5. For a dye laser droplet with a distinct bandwidth $\Delta\lambda_g$, the number of the cavity modes increases for increasing cavity dimension; i.e. droplet radius, and thereby the distance between the modes decreases; i.e. a decrease of the mode-spacing.
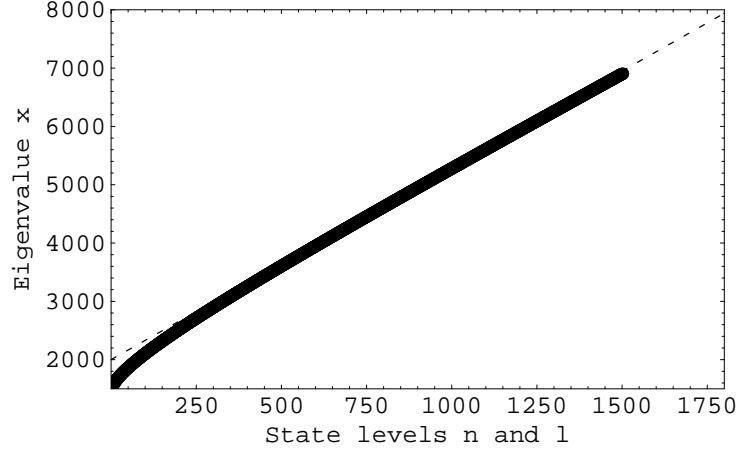
Figure 4.4: The graph shows the plotted eigenvalues versus n and l mode states. Neglecting the m mode does not affect the wavelength (energy). The dashed line is the asymptote in the interesting eigenvalue region corresponding to the wavelength region 570-585 nm for different droplet radii. The slope of the asymptote is determined to be approximately $\Delta x = 3.4$.

Droplet radius R	Laser wavelength λ	$\Delta\lambda_n$	$\Delta\lambda_{nlm}$
150 μm	577 nm	0.76 nm	0.22 nm
270 μm	580 nm	0.43 nm	0.13 nm
330 μm	574 nm	0.34 nm	0.11 nm
600 μm	616 nm	0.25 nm	0.07 nm

Table 4.2: The two mode-spacing expressions $\Delta\lambda_n$ and $\Delta\lambda_{nlm}$ from eq. (4.4) and eq. (4.38), respectively, are calculated and compared for four different droplet radii. Only $\Delta\lambda_{nlm}$ will be compared to measurement results in Chapter 7

4.3.1 Discussion of The Similarities between The Resonator Model and The Liquid Droplet

Although the described resonator model (the electromagnetic theoretic analysis), which takes a shielded homogeneous and isotropic dielectric sphere as a starting point, seemingly is not quit similar to the liquid droplet, however it can be emphasized that the resonator model still can be used to qualitatively describe the hemispherical liquid droplet.

- **The metallic shielded sphere versus the surface of the liquid droplet**: Here we focus on the refractive index. Simply the refractive index has to be higher at the surface (and in the inside) of the droplet than the surrounding (outside the droplet) to ensure total reflection of the electromagnetic modes inside the droplet. The refractive index for the EG droplet is, as above-mentioned, $n_{eg} = 1.43$ compared to the air with $n_{air} = 1$. This is comparable to the metallic shielded sphere, since this also posses a quit high refractive index. Silicon may for instance have a

refractive index up to 4 depending on the wavelength of the light. This was manifested in the assumption in the analytical model that the divergence of the electric field at the surface of the sphere is zero ($\nabla \cdot \mathbf{E} = 0$).

- **A sphere versus a hemisphere**: One could argue that simply a change of volume would not affect the mode-spacing, since this according to eq. (4.38) only depends on radius and not volume. Thus, one only have to ensure that the radii of the sphere and the hemisphere is similar, for the two to be comparable. However, on the other way one could consider R as a variable depending on the volume. In this case, the volume differences between the sphere and hemisphere is significant. Thus, a change of droplet volume is a change of droplet radius and is consequently a change in the mode-spacing. Before we proceed, it should be noted that the droplets created on surfaces in this project were not spherical but hemispherical or at best semi-spherical, [2] as will be shown in the following chapters. If we for instance consider a semi-spherical droplet, the volume V_{half} of this corresponds to the half of the sphere with volume V; i.e. $V_{half} = V/2$. Assuming that this reduces the radius of the half droplet to $R_{half} = R/\sqrt[3]{2} = R/1.3$, where R is the radius of the sphere, the mode-spacing will decrease to $\sim \Delta\lambda/1.3$, where $\Delta\lambda$ is the mode-spacing in a sphere. So, even with the assumption of change in volume, the mode-spacing in a semi-spherical droplet remains approximately in the same order as for a sphere, what allows a qualitative comparison between the analytical results and the experimental. This comparison will be carried out in Sec 7.3. It should be noted that the assumptions made for the semi-spherical example presupposes that the the halved droplet volume also assumes a spherical droplet, which is not the case with our droplets. Although they both posses the same volume, our droplet does not change its radius. However, the assumption was necessary to interpret the decrease of the mode-spacing in the case of halved droplets.

4.4 Numerical Calculations of The Modes in A Sphere

After finishing the theoretical description of the WGMs, it would be quit interesting to visualize these in a sphere with dimensions lying between 150 μm and 300 μm. For that purpose a simulation program called FEMLAB was utilized.

FEMLAB

Finite Element Modelling LABoratory (FEMLAB) is a partial differential equation solver that builds on MATLAB. FEMLAB is an advanced software package for modelling and simulation of any physical process that can be described with partial differential equations (PDEs). Before initiating the solver, a differential equation must be specified in some geometry, the so-called computational domain, together with the boundary conditions along the surface of the domain as well as the initial values at the starting time. The computational domain

---

[2]By a semi-spherical droplet I mean a droplet forming a contact angle of 90° with a surface, i.e. the half of a sphere.

is divided into a huge number of finite-sized elements forming the basis for computation.

After the introduction of the analytic description of the electric field modes inside a shielded homogenous and isotropic dielectric sphere, we are now interested in simulating the modes in FEMLAB for the same geometry i.e., that is inside a sphere. The numerical calculations are then compared to those predicted by the electromagnetic analytical model.

Before starting the simulation, a specialized module has to be chosen and a differential equation specified. Since we are working with electromagnetic equations, it was natural to chose The Electromagnetic Module [3] to work within. However, this module turned out to be very unstable [4] in simulating the modes, for which reason we could not use it, though. Therefore, another module had to be chosen.

The simulated wave

The wave equation eq. (4.25), solved in the previous section, Section 4.3 can be rewritten to

$$\nabla^2 \mathbf{E} = \left(\frac{\omega}{c}\right)^2 \epsilon_r \mathbf{E} \tag{4.39}$$

At the first glance, we notice the similarity between eq. (4.39) and the Shrödinger equation [5] describing a quantum particle in a spherical well given by eq.(B.4)

$$-\nabla^2 \psi(\mathbf{r}) = \xi \psi(\mathbf{r}) \tag{4.40}$$

Therefore, we have chosen to use The Shrödinger Module in 3D-space to simulate the modes. Incidentally, eq. (4.39) is a scalar function, which means that the simulation is expected to be easier and faster contrary to a vectorial equation. The divergence of $\mathbf{E}$ was in FEMLAB specified to be zero at the boundary of the sphere.

Simulation

Before solving the PDE, the desired number of eigenvalues and the specific eigenvalue had to be chosen.

For instance, having chosen to search for four numbers of eigenvalues for the eigenvalue, $x^2 = 0$, one gets the fundamental mode $x_{nlm}^2 = x_{101}^2 = 9.870$ and 3-degenerates for $x_{113}^2 = 20.195$. This is shown in Fig.4.5 and Fig 4.6-4.8.

---

[3]This Module, programmed in FEMLAB, deals with wave propagation and mode analysis in microwave engineering and photonics, static and quasistatic electromagnetic field simulations.

[4]In this mode, the Module deals with a vectorial equation making it very exacting to simulate the Maxwell's equation. Add to this the meshing procedure that consumes to much computer power.

[5]The solution to the TE mode could, alternatively, be carried out by introducing the angular momentum operator $\mathbf{L}$ defined as, $L = (1/j)(\mathbf{r} \times \nabla)$, where $j = \sqrt{-1}$, and constructing L^2 and its relationship with the Laplacian operator. This procedure can be identified with the derivation considering a quantum particle in a sphere with energy spectrum governed by the one-particle Schrödinger equation in Appendix B.
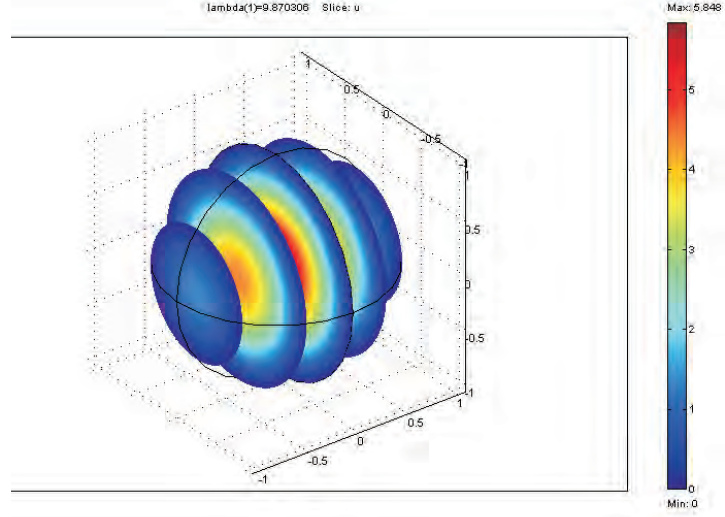
Figure 4.5: The electric field intensity distribution for the fundamental mode with $(n, l, m) = (1, 0, 1)$

.
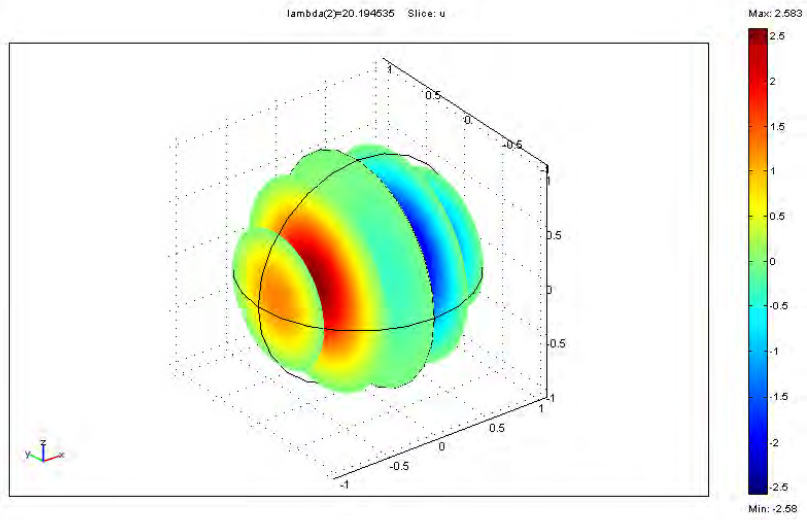
Figure 4.6: The electric field intensity distribution for the mode with $(n, l, m) = (1, 1, 1)$ with $x^2 = 20.195$.
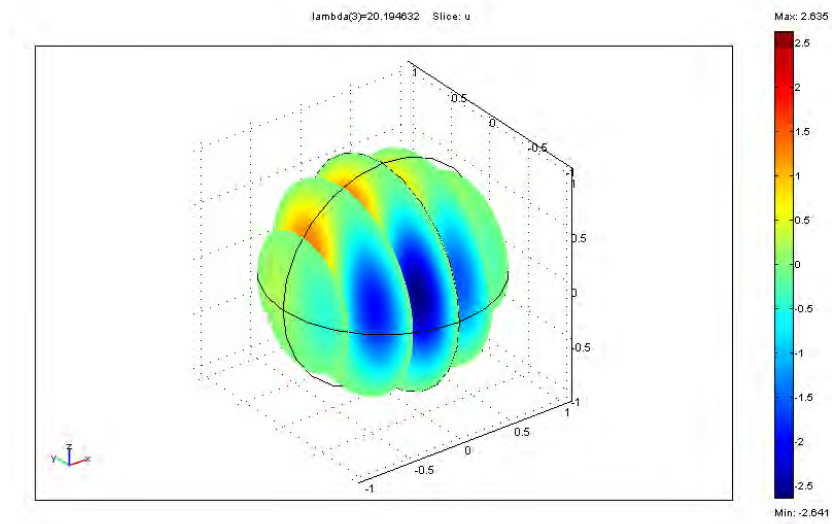
Figure 4.7: The electric field intensity distribution for the mode with $(n, l, m) = (1, 1, 2)$ with $x^2 = 20.195$.
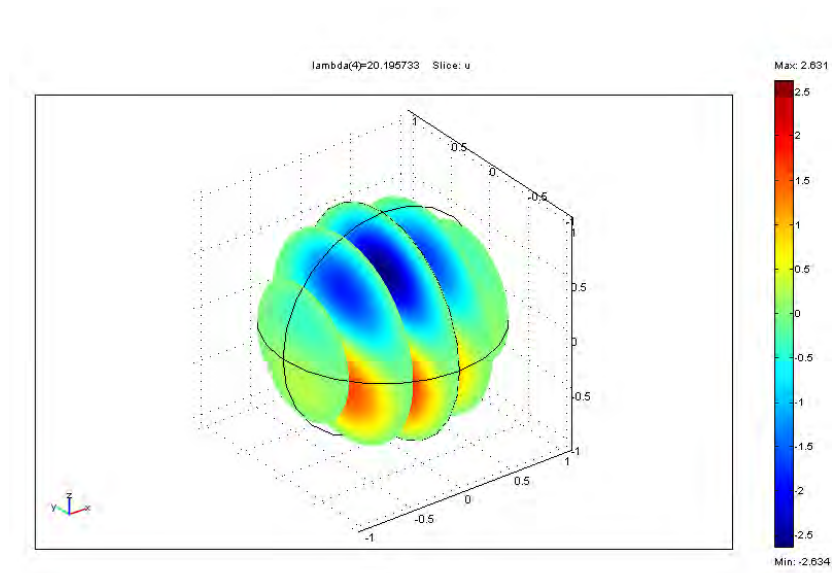

Figure 4.8: The electric field intensity distribution for the mode with $(n, l, m) = (1, 1, 3)$ with $x^2 = 20.195$.

The color nuance indicates the electrical field intensity distribution. For the

fundamental mode in Fig. 4.5, the electrical field intensity has its maximum (red color) in the center of the sphere and flattens out or decreases at the edge of the sphere (blue color). The equatorial electric field component lies in the plan of the polar component ($m = n$) having no radial component ($l = 0$). On the other hand, the mode ($ml = 11$) having one polar electric field component corresponding to the radial component, has three equatorial components of the electric field intensity distributions ($m = 3$) in each direction of the x, y, z-system.

The results obtained from a series of mode simulations is shown below in Table 4.3. In order to control wether there is consistency between the results predicted by theory, in Table 4.1, and those given by simulation in Table 4.3, they were compared in Fig. 4.9.

	l				
n	0	1	2	3	4
1	9.870	20.195	33.233	48.880	67.079
2	39.511	59.779	82.972	109.054	-
3	89.149	-	-	-	-

Table 4.3: The table showing some eigenvalues of x_{nl}^2 for different modes of n and l.
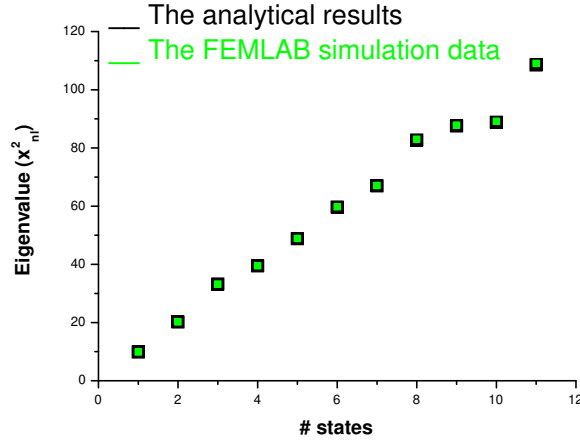
Figure 4.9: Eigenvalues with analytical results indicated by black points and FEMLAB data by colored points.

As it clearly emerges from Fig 4.9, the FEMLAB results are completely identical with the analytical results, meaning that we can rely on the simulation for further simulations where analytical theory is limited. The eigenvalue determined in FEMLAB is given by

$$x_{nl}^2 = (kR)^2 \tag{4.41}$$

For a droplet with radius $R = 330$ μm, for instance, optically operating (laser emission) in the interval 570-585 nm, the search of the interesting eigenvalues, lying in the lasing range, has to be made in the eigenvalue interval 5070^2-5200^2. Choosing an eigenvalue of $x^2 = 5000$ lying in between as a searching value in FEMLAB, unfortunately we get a meaningless result as shown in Fig 4.10.
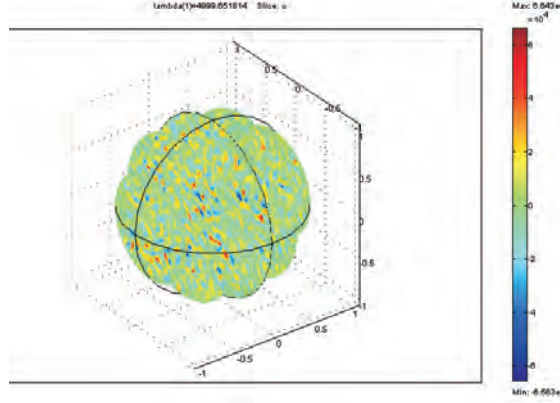
Figure 4.10: A meaningless result for the electric field intensity distribution for the eigenvalue $x^2 = 5000$ due to limitations in FEMLAB.

It turned out that for very high values of eigenvalues, as above stated, the FEMLAB simulation is limited. This is due to the so-called meshing-net. The number of eigenvalues corresponds to the number of the meshing points. Therefore, there cannot exist a higher number of eigenvalues than the meshing points. Desiring a higher eigenvalue, the meshing net must be even comminuted, in order to give rise to more points.

Nevertheless, with the existing limitation in FEMLAB, the maximal eigenvalue for which a meaningful and usable mode simulation is obtained, can be examined. This is done by carrying out random tests far below the interesting eigenvalue interval in FEMLAB. Only at an eigenvalue $x^2 = 500$ a usable mode simulation is obtained. This is shown in Fig 4.11. This maximal eigenvalue has 9-degenerates ($m = 9$) and corresponds to the longitudinal and radial electromagnetic field components $n = 4$ and $l = 8$, respectively. It is interesting to note, that each has its own characteristic electric field intensity distribution mainly lying at the circumference of the sphere, suggesting the WGM effect. Assuming the dye droplet to emit laser light at $\lambda = 580$ nm, the eigenvalue $x^2 = 500$ in this case conditions a shape dimension about $R \simeq 2$ μm. If we go further down in the eigenvalue interval to $x^2 = 88.8$ for instance, a more clear and distinct intensity distribution of the totaly electric field clearly lying at the circumference of the sphere. The electric field intensity distribution lying at the circumference of the sphere, confirms our assumption of a WGM effect. The eigenvalue $x^2 = 88.8$ with 7-degeneracy ($m = 7$) corresponds to $n = 3$ and $l = 1$, which besides clearly emerges from the simulation. By assuming again that $\lambda = 580$ nm, the eigenvalue conditions $R \simeq 600$ nm.

47

It was our purpose to carry out mode simulations, truly with a metallic sphere, but still for spheres lying in the dimension corresponding to the created droplets in this thesis. These had dimensions in the micron range, more specifically in the 150-300 μm range. And since the simulation program (FEMLAB), with its existing setting op, only can simulate modes for droplets with dimensions approximately 100-1000 times less than the current droplets; actually in the order of the wavelength of the lasing spectra. We therefore ascertain that it is by no means possible to simulate the modes for our micron sized droplets. Although it is not quit satisfactory, we may now form a qualitative picture of WGM behavior in a sphere. In addition, it was our purpose to make numerical calculations of the modes for a semi-sphere lying on a surface. However, in the light of the above mentioned FEMLAB limitations, this was abandoned.
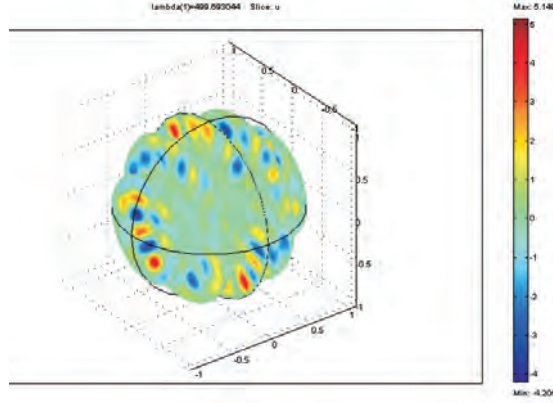
Figure 4.11: A mode simulation for the maximal eigenvalue lying about $x^2 = 500$. This corresponds to $n = 4$, $l = 8$, $m = 9$ and radius $R = 2$ μm. The total electric field intensity distribution lying mainly at circumference of the sphere.
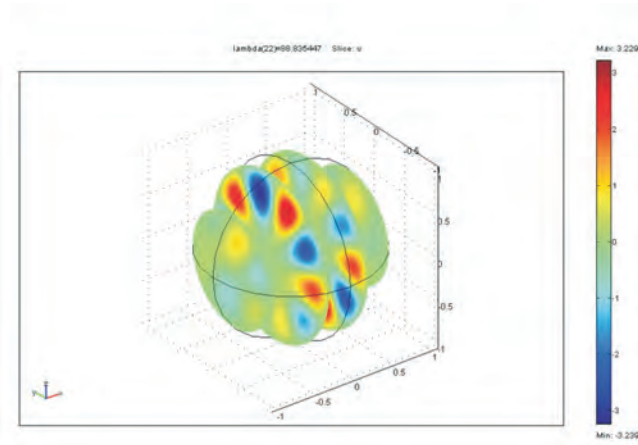
Figure 4.12: A mode simulation for an eigenvalue lying about $x^2 = 88.8$. This corresponds to $n = 3$, $l = 1$ and $m = 7$ and radius $R \simeq 600$ nm. The total electric field intensity distribution lying mainly at circumference of the sphere.

Chapter 5

Fabrication of Hydrophobic Surfaces

This chapter describes the process which I have been through in order to fabricate suitable hydrophobic surfaces. The hydrophobic term in this context is actually misleading. A more physically correct term to use is ethylene-glycol-phobic when dealing with optimizing the contact angles for EG droplets. More specifically, the chapter is initiated by a description of the various fabrication steps and techniques, with the aim improving the ethylene-glycol-phobic properties of the surfaces. This is manifested in the optimizing of the contact angles for EG liquid droplet, by carrying out various experiments on these surfaces. Also a brief description of the used clean room equipments such as the Reactive Ion Etching machine and the Scanning Electron Microscope is given in Section 5.4.1 and 5.6, respectively.

5.1 The Untreated Surfaces - A Standard of Reference

As described in the previous chapter, we are interested in creating a spherical droplet with highest possible contact angle. This we demand to ensure that the walls of the droplet has the optimal condition to function as an effective resonator capable in reflecting the light inside the droplet, and to reduce the light interaction with the surface. The spherical shape of the droplet is ensured by creating droplets with radius less than 1 mm according to the Bond number. To constitute a standard of reference, we started to measure the contact angle for an EG droplets placed on various untreated surfaces such as, gold, glass and silicon. This is shown in Fig 5.1-5.4. All the obtained measurements are listed in Table 5.1
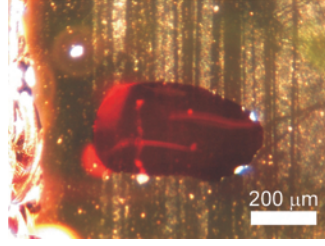
(a) The droplet seen from above (at an angle of 90°) with an un-spherical shape.
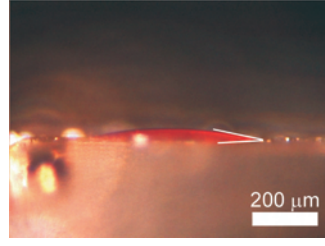
(b) A side view of the droplet (at an angle of 0°). The contact angle formed by the droplet on the surface is $\theta \approx 20°$.

Figure 5.1: An EG droplet (with the dissolved Rh6G) placed on an un-treated gold surface.
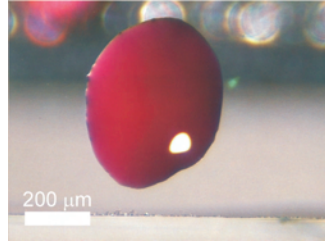
(a) The droplet seen from above with an un-spherical shape.
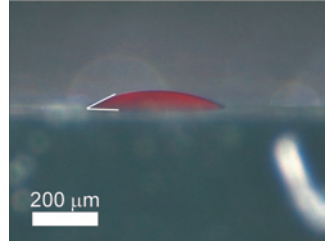
(b) A side view of the droplet . The contact angle formed by the droplet on the surface is $\theta \approx 30°$.

Figure 5.2: An EG droplet (with the dissolved Rh6G) placed on an un-treated glass surface.
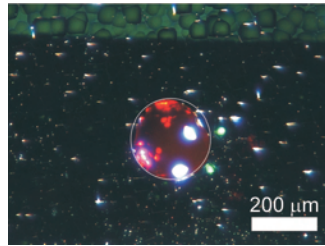
(a) The droplet seen from above. The droplet having a radius $R \approx 80$ μm has a spherical shape indicated by the white circle added by the author.
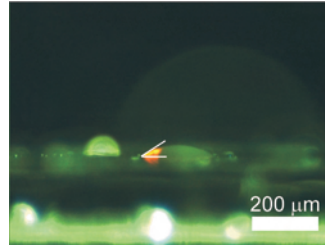
(b) A side view of the droplet. The contact angle formed by the droplet on the surface is $\theta \approx 38°$. The green color in the picture is due to the used filter in the microscope system.

Figure 5.3: An EG droplet (with the dissolved Rh6G) placed on an un-treated silicon surface.

(a) The droplet seen from above. The droplet having a radius $R \approx 300$ μm has a nearly spherical shape indicated by the white circle.
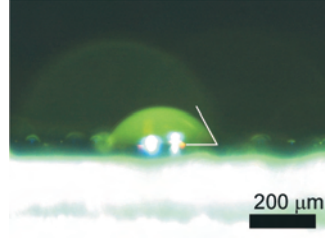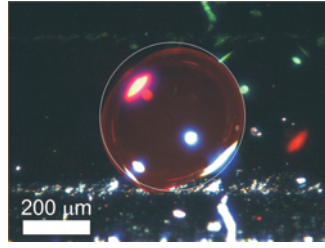
(b) A side view of the droplet. The contact angle formed by the droplet on the surface is $\theta \approx 37°$.
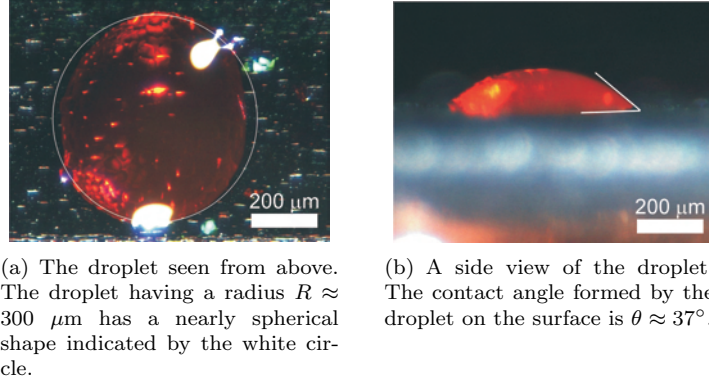
Figure 5.4: An EG droplet (with the dissolved Rh6G) placed on an un-treated silicon surface.

	Contact angle θ	Droplet radius R
Gold	21°	-
	19°	-
Glass	30°	-
	31°	-
Silicon	37°	300 μm
	38°	80 μm

Table 5.1: The contact angle results for EG droplet lying on various un-treated surfaces.

It emerges that the contact angles for the EG droplet placed on the mentioned surfaces are relatively low. The average contact angles were measured to 20°, 30° and 40° for gold, glass and silicon, respectively. Apparently, these surfaces with these low contact angles does not serve our purpose. Nor is the shape of these droplets spherical on gold and glass surfaces, but more deform and indefinable, why special suitable ethylene-glycol-phobic surfaces had to be fabricated. However, for the silicon surface the shape of the EG droplets is more spherical. And since the contact angle for silicon is relatively high this may suggest silicon surfaces to be involved in the further fabrication process of ethylene-glycol-phobic surfaces.

5.2 Fluorocarbon Deposited Si-surfaces

The first obvious thought was to make the silicon surfaces ethylene-glycol-phobic by depositing an anti-sticking hydrophobic coat on them. Ayón *et al.* [43] reports fluorocarbon film, C_4F_8, also called Teflon®, as a useful anti-stiction film with promising hydrophobic property. The contact angle for de-ionized water droplets lying on a fluorocarbon film surface, was in [43] measured being quit high lying in the interval $> 108°$. By using C_4F_8 as feed gas in a plasma tool,

teflon[R] film was deposited onto silicon surfaces using the Advanced Silicon Etching (ASE) machine [1].

Three different Silicon surface types were chosen to be coated with Teflon[R]:

- Si_3N_4/Si : A silicon surface (wafer) deposited with a 2.5 μm thick or silicon nitride (Si_3N_4) layer .

- A smooth Si-surface.

- A rough Si-surface with an estimated rms roughness of 10-30 μm. The estimate was given by cleanroom laboratory technician.

A silicon nitride wafer is highly hydrophile, since the OH-groups would not bind to the surface. A purely silicon (Si) wafer is hydrophobic. This applies only for a relatively short period. Gradually, the surface will be covered by O^2, resulting in a reduce of the hydrophobic property of the surface. Based on the theory of hydrostatic, it is believed that a rough surface results in a higher contact angle than the smooth. This fact will throughout some experiments be tested. The rough surface in this case is simply the backside of the Si-wafer. The deposition time of fluorocarbon in the ASE is 30 sec. According to Ayón *et al.* [43] this deposition time gives a fluorocarbon thickness just below 1000 Å . Fig 5.5, Fig 5.6 and Fig 5.7 shows a random selection of the contact angle measurements for EG droplets carried out on these surfaces. The water droplet is shown in Fig 5.8 as a standard of reference. The averaged measurements are listed in Table 5.2
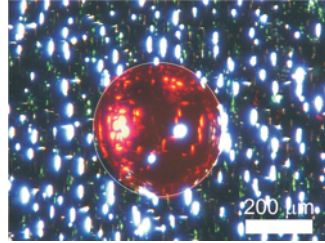
(a) The droplet viewed by a microscope seen from above. The droplet having a radius $R \approx 190$ μm has a nearly spherical shape indicated by the white circle. The white spots is the scattered microscope light.
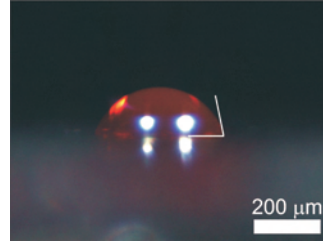
(b) A side view of the droplet. The contact angle formed by the droplet on the surface is $\theta \approx 77°$.

Figure 5.5: An EG droplet (with the dissolved Rh6G) placed on a rough silicon surface coated with Teflon[R].

---

[1]The ASE machine is usually used to etch the silicon only. However it also can be used to deplete teflon on various surfaces.
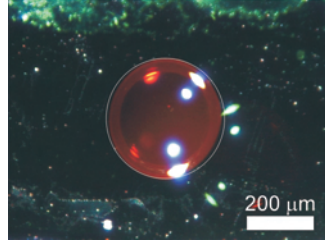
(a) The droplet seen from above. The droplet having a radius $R \approx$ 170 μm has a nearly spherical shape indicated by the white circle.

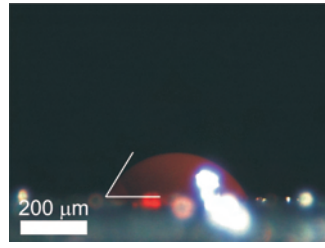(b) A side view of the droplet. The contact angle formed by the droplet on the surface is $\theta \approx 65°$.

Figure 5.6: An EG droplet (with the dissolved Rh6G) placed on a smooth silicon surface coated with Teflon®.

(a) The droplet seen from above. The droplet having a radius $R \approx$ 210 μm has a nearly spherical shape indicated by the white circle.

(b) A side view of the droplet. The contact angle formed by the droplet on the surface is $\theta \approx 61°$.

Figure 5.7: An EG droplet (with dissolved Rh6G) placed on a smooth Si_3N_4 surface coated with Teflon®.
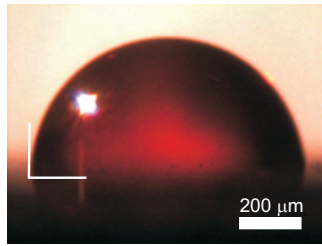
Figure 5.8: A water droplet (with the dissolved Rh6G) forming a contact angle 92° on a silicon surface coated with Teflon®.

	Contact angle θ	Droplet radius R
Si/Si$_3$N$_{42}$	61°	210 μm
Smooth Si	65°	170 μm
Rough Si	77°	190 μm

Table 5.2: The contact angle results for EG droplet lying on various fluorocarbon deposited silicon surfaces.

Compared to results obtained with the un-treated surfaces, apparently an increase in the contact angles was detected. At first eye glance, it is tempting to view the obtained results in agreement with the expected: theory of hydrostatics of micro-droplets. The hydrophilic surface (nitride silicon) assume the position as the surface giving the lowest contact angle compared to the other ethylene-glycol-phobic surfaces, namely 61°. And the smooth hydrophobic surface (smooth Si) gives a less contact angle than the rough, namely 65° compared to 77° for the rough.

However, all the measured values lye very close to each other, why the uncertainty connected to the manual measurements of the contact angle also may be considered. I have estimated the uncertainty to be about 5°. This value nearly corresponds to the difference between the highest and the lowest contact angle measurement. Therefore, we can only ascertain that the Teflon$^{®}$ deposited on Si-surfaces actually increases the contact angle for EG droplets to 65°-77° compared to the un-treated surfaces.

As regards the water droplet, the contact angle for this was measured to about 92°, which is relatively high compared to the EG droplets on the various Si-surfaces. This contact angle value is above 90 ° and is in the order of the reported value in [43]; i.e. > 108°. The reason for the deviation in contact angles between water and EG is due to the unique surface energy property they every each possesses. Unlike EG, the surface tension is much higher for water, namely 72.8 mN/m.

Utilizing Young's equation, the surface energies for fluorocarbons can be predicted. Inserting the expression for the component of the solid-liquid surface tension $\sigma_{sl} = \sigma_{lg} - \sigma_{sg}$ [9], in the Young's equation, eq. (2.24) we get

$$2\sigma_{sg} = \sigma_{lg}(1 + \cos\theta) \tag{5.1}$$

Inserting the measured contact angle for water $\theta_{water} = 92°$ and the surface tension for water $\sigma_{lg} = 72$ mN/m in eq. (5.1) we get $\sigma_{sg} \simeq 34$ mN/m for the surface tension of the used fluorocarbon film. This is in the order of the reported result in [43], where the measured contact angles in this corresponded to energies from more than 10 mN/m to less than 5 mN/m. The variation in the surface energies is due variations of the concentration in the fluorocarbon films. The higher the concentration the higher becomes the contact angles [43].

In an attempt to optimize the contact angle further, we experimented with the following surfaces.

5.3 Nanoglass® Grown on Si-surfaces

However, the results of the contact angle measurements on Teflon deposited Si-surfaces were not quit satisfying. In the meantime, we initiated a corporation with Dr. David Mecerreyes [44] on the surface modification of silicon wafers project. He suggested to use a polymer growth from the surface in order to make it ethylene-glycol-phobic for which reason he offered to modify the silicon surfaces using nanoporous silsesquioxane materials, commercially known as Nanoglass®. Nanoporous glasses is a porous material with very low dielectric constants. It is deposited by a standard spin coater employing standard spin, bake and hot plate cure. The nanometer-scale porosity is produced by adding a sacrificial polymer to the precursor glass solution. The polymer is initially soluble but phase separates into nanometer-size domains during initial curing of the glass. The polymer is volatized at high temperatures, and the glass is vitrified to leave a porous glass film [45], [46], [47]. The Nanoglass® is widely applied in a number of technologies as in optical, electronic and biological technologies that uses nanoporous thin films, but are limited by the degradation of mechanical properties. In our case, it was believed that the porosity properties of nanoglasses increases the ethylene-glycol-phobic property of the surfaces.

Suitable surfaces were sawed in proper dimensions (1 cm×1 cm) and send to Spain. A few weeks later, we received the modified surfaces, with the instructions telling us that the surfaces needed no further treatment and were ready for contact angle measurements. Thus, the contact angle measurements were initiated. Unfortunately, the results were quit disappointing, since the measured contact angles were lower than or equal to the measured contact angles for the Teflon® deposited surfaces. This is shown in Fig 5.9. The contact angles were lying in the interval of $50° - 70°$.

In order to increase the hydrophobicity of the Nanoglass® surfaces, these were intended to be coated with fluorocarbon film. However, the idea was abandoned after examining the Nanoglass® surfaces in the Scanning Electron Microscope (SEM). The pictures taken with SEM revealed a silicon landscape, instead of porous-nano-glass structures, covered with few randomly distributed spots as shown in Fig 5.10(a). Zooming into the spots with the diameter of 34 μm in Fig 5.10(b), these seems to posses a rough porous surface, presumably the porous-nano-glass structures. Based on the SEM pictures of the Nanoglass®, it seems that the silicon surface is tried coated with the porous-nano-glass, but the attempt however failed. Obviously another solution was to be found.
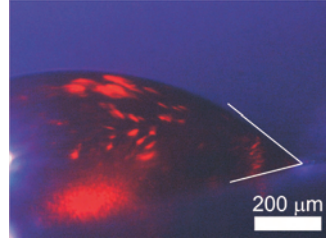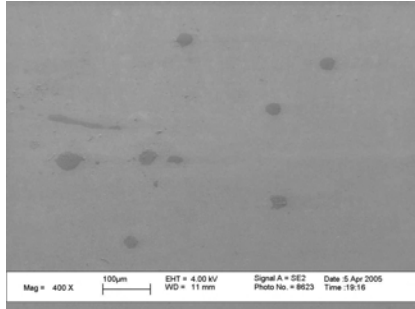
(a) The contact angle formed by the droplet on the surface is $\theta \approx 57°$.
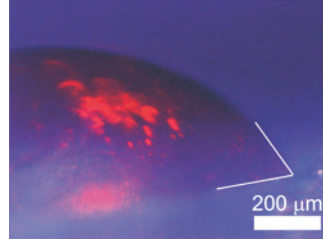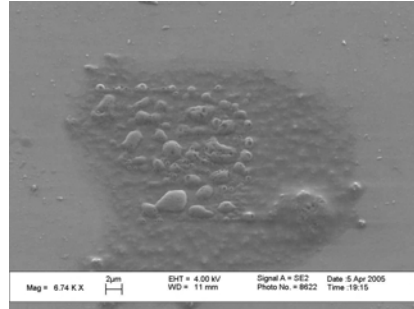
(b) The contact angle formed by the droplet on the surface is $\theta \approx 65°$.

Figure 5.9: A side view of EG droplets (with the dissolved Rh6G) placed on two different Nanoglass surfaces. The obliquity of the picture is due to the microscope camera that was mounted obliquely.

(a) A SEM picture of the presumed porous-nano-glass structures. Notice the few distributed spots.

(b) A close-up view of a spot in Fig 5.10(a) seeming to posses a rough porous surface.

Figure 5.10: SEM pictures of the presumed silicon-Nanoglass®-deposited surface.

5.4 Black Silicon Surfaces

In [49] and [50], the so-called black silicon (BS) surfaces were fabricated, and seemed to posses super-hydrophobic properties, the reason why the fabrication of BS was initiated and a series of contact angle measurements were performed.

BS is nano structures appearing on the silicon surface etched by the Reactive Ion Etching (RIE) machine. The surfaces were etched for various etching periods in attempt to optimize the contact angle. In the following a brief description of the operation of the RIE and the fabrication of BS surfaces is given; followed by the performed experiments on these surfaces.

5.4.1 Reactive Ion Etching

Reactive Ion Etching (RIE) is a very common and used etching technique. It was developed in the 70'ies in order to replace the only etching technique then;

wet etching [51], and is especially usable to dry anistropic etching.

In our case, the RIE is used to etch black silicon (BS) on silicon wafers. BS is nano-peaks that appears at the silicon surface making the surface very rough, that light once trapped between the peaks, is prevented from escaping the surface, hence the term black.
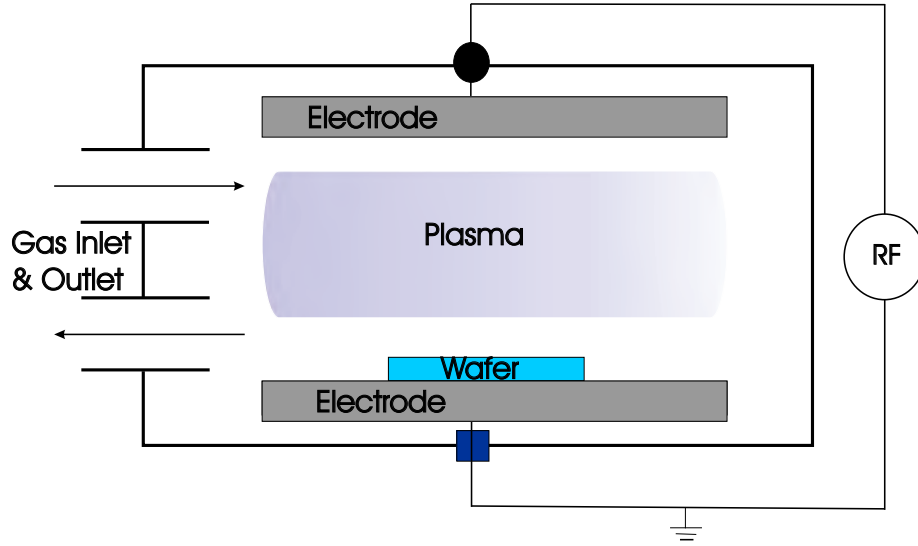

Figure 5.11: A schematic setup of RIE's mode of operation.

Fig 5.11 shows a schematic set-up of the RIE system.
The RIE system consists of two electrode plates placed in parallel toward each other. Between the electrodes we have the plasma chamber. The wafer is placed on the lowest electrode. The upper electrode is connected to the chamber walls which is grounded, while the lowest is connected to a Radio Frequency (RF) generator applying it a voltage drop. In principle, the RIE technique make use of two etching mechanisms; a physical and a chemical. By using the two gases SF_6 and O_2, the ions are used both to knock of the atoms from the surface and via a chemical reaction to etch it. A more fully description of the two mechanisms follows. After injecting the SF_6 gas inside the chamber and applying a voltage drop between the two electrodes via the RF, the introduced gas is ionized to fluorine free radicals F^- and SF_5^+ ions, creating the plasma. The fluorine ions reacts with the silicon surface creating SiF_4 which is a volatile gas, and which is pumped out of the system. The consequence of this reaction is an etch of the silicon surface resulting in an isotropic etch profile as shown in Fig 5.12.
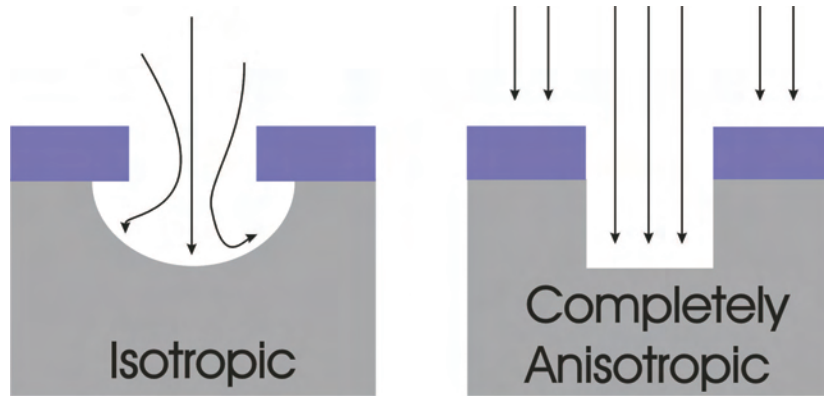
Figure 5.12: A schematic diagram of the etching profile: the isotropic and the completely anisotropic.

Unlike the fluorine ion the positive ions will be influenced by the applied electric field orthogonal to the wafer, and will consequently be accelerated along the field line towards the wafer. The result will be that these positive ion hit the surface with an energy high enough to tear off the silicon atoms from the surface. The result will be an anisotropic etch profile. For a more anisotropic etch profile different gasses can be use such as O_2, CHF_3, CF_4 and SF_6. However O_2 is used in our case. F^- and O^- ions bind to silicon forming SiO_xF_y and hereby passivating the surface. It protects the surface lying beneath it. As the etching process proceeds, and since SiO_xF_y distributes randomly on the surface, the characteristic peaks will appear, and the peaks will get taller. This is shown in Fig 5.13.
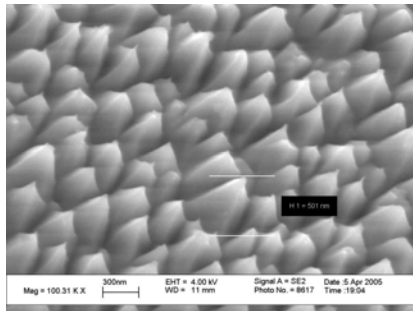
(a) A SEM picture of the characteristic peaks on a BS surface after an etching period of 25 min. When viewed in SEM, the sample was tilted about 30°.
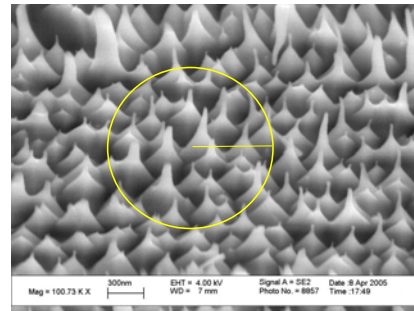
(b) A SEM picture of the characteristic peaks on a BS surface after an etching period of 45 min. When viewed in SEM, the sample was tilted about 45°.

Figure 5.13: The characteristic peaks are becoming taller during etching.

5.4.2 Contact Angle Measurements on BS Surfaces Deposited with Teflon®

Five various types for BS surfaces were fabricated for five process times (etching periods): 25 min, 30 min, 35 min, 40 min, and 45 min, in order to optimize the contact angles. However, it should be noted that (later experienced), the length of the peaks does not keep increasing as a function of the etching time. Depending on the used recipe, the length of the peaks reaches a maximum, where they no longer increases. Only the surface level decreases for further etching.

However, after having coated the various fabricated BS surfaces with fluorocarbon by following the above mentioned recipe, the contact angles were measured for these surfaces and plotted in Fig 5.14.

Fig 5.15-5.17 shows pictures of the contact angle measurements for three various etching periods. The results were overwhelming good.
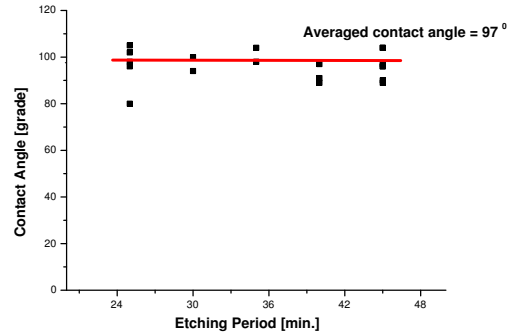
Figure 5.14: A plot of the measured contact angles for the five various types for BS surfaces fabricated for five process times.
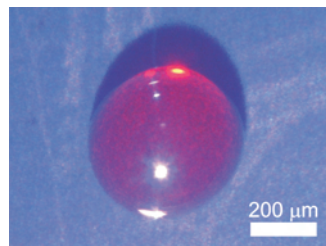
(a) The droplet seen from above. The shape of the droplet is clearly spherical.
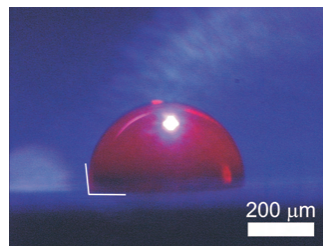
(b) A side view of the droplet. The contact angle is measured to about 95°.

Figure 5.15: An EG droplet (with the dissolved Rh6G) placed on a BS surface coated with Teflon®.

(a) The contact angle is 95° on a silicon surface etched for 25 min.

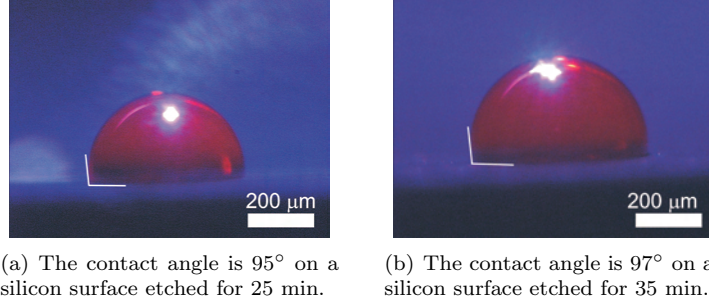(b) The contact angle is 97° on a silicon surface etched for 35 min.

Figure 5.16: The contact angle for various etched processed periods on a BS surface coated with Teflon®.
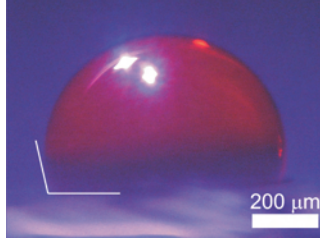

Figure 5.17: The contact angle is about 100° on a silicon surface etched for 45 min.

As it emerges from the plot and the pictures, the measured contact angle is quit constant, lying in the interval 90°-105°, for all the varied etching periods. That is directly opposite our expectation that the contact angles will increase with increasing etching. However, this turns out to be logic and in agreement with the theory.

The results can be explained by the Cassie-Baxter equation; eq. 2.30, for rough surfaces. It predicts an increase of the contact angle on rough surfaces only if the surface fraction being in contact with the droplet ϕ_s is increased; i.e. a high peak density. What we have here is a constant ϕ_s since the etching does not affect or change the number spikes per area, but only the length of the spikes. In the light of this argument it is understandable why the contact angle is constant for all the etching varied surfaces.

To determine whether the Fakir or the Wenzel state is the dominating state on the fluorocarbon-coated-BS surfaces, the surface energy of the two states must be compared. The Fakir state will be the stable state if the surface energy in this, is lower than the one in the Wenzel state [24]. Mathematically, this is the case if $\cos\theta < -1/r$, where θ is the contact angle on a flat surface and r is the surface roughness. The surface roughness was in Section 2.3.3 defined as the ratio between the actual (or real) surface area A' and the projected one (the macroscopic) A. Considering a surface area $A = 1.5$ μm^2 (indicated as the yellow circle in Fig 5.13(b)), this contains about $N_{peak} = 16$ peaks each with an average length $L_{peak} = 350$ nm and an average distance to adjacent peak $W_{peak} = 300$ nm. Thus, the actual surface area is estimated as $A' =$

$(2L_{peak} + 2W_{peak})N_{peak} = 60 \ \mu m^2$. This corresponds to a roughness $r \simeq 13$ $\Rightarrow 1/r = 0.07$. Since the contact angle on fluorocarbon coated smooth silicon surface [2] was measured to about $\theta = 65°$ in Section 5.2 we get: $\cos \theta < -1/r \Rightarrow -0.56 < -0.07$, indicating that the Fakir state is the stable state in this case. Hence, the droplet on a BS surface is sitting on the peaks, and do not fill the areas between them.

Fig 5.18 shows a water droplet lying on the BS surface depleted with Teflon®. The contact angle is measured to be about 145°. The Teflon®-deposited BS can nearly be categorized as super-hydrophobic. Because the surface is highly hydrophobic, the water droplet could only be placed on the surface if it was relatively large in order for the gravitation to overcome the very high surface tension. This explains the large shape of the droplet in Fig 5.18.
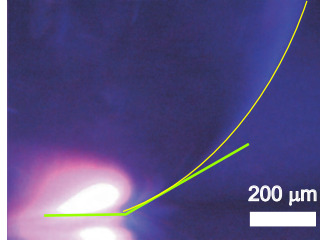
Figure 5.18: A water droplet placed on a Teflon®-deposited-BS surface with a contact angle of about 145°. The droplet shape of the droplet is indicated with the yellow line.

5.5   BS Surface with Grooves

The semi-spherical droplet lying on the BS surface was observed to consistently assume a more deform form while being pumped with an external laser as shown in Fig 5.19.
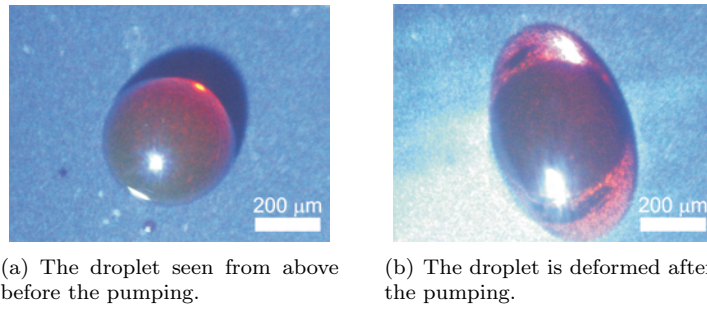

(a) The droplet seen from above before the pumping.

(b) The droplet is deformed after the pumping.

Figure 5.19: A droplet placed on a BS surface coated with Teflon® before and after being pumped with an external laser.

The deformation was thought to have something to do with the orientation of the surface making it easy for the droplet to deform in certain direction. But

---

[2]It should be noted, that only the smooth silicon surface wafer was used for RIE-etching.

what provokes the deformation is yet unknown. It was therefore necessary to fabricate grooves on BS surfaces in order to prevent the droplet from deforming. These patterned surfaces were fabricated by utilizing the Nanoimprint Lithography (NIL) technique. The concept of NIL process technique is quit simple. In Fig 5.20 the basic NIL processes are shown.
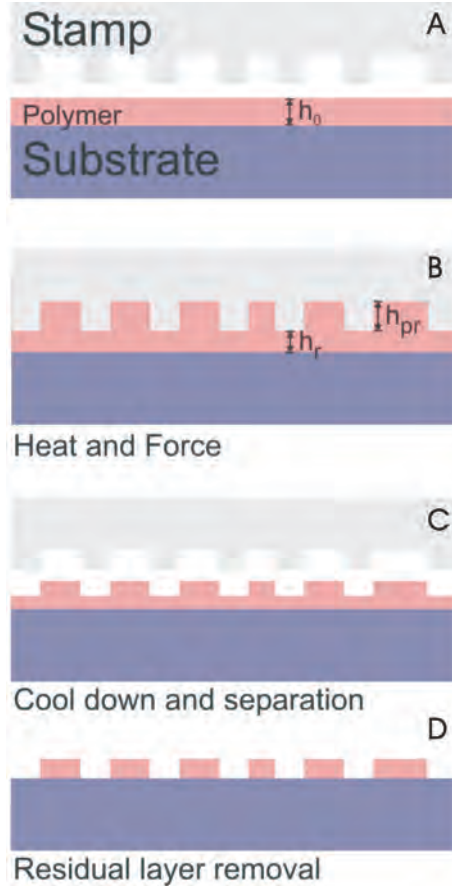

Figure 5.20: NIL processes [52]. A) The stamp and substrate before heating. B) The stamp and substrate are heated, and the stamp is pressed into the polymer. C) The stamp and the substrate are cooled, and the stamp separated from the polymer. D) The imprinted pattern is transferred after the residual layer removal.

A silicon surface is deposited with a thin film poly-methylmethacrylate (PMMA) by spin-coating onto a 4-inch silicon wafer. This is heated to above the glass transition temperature ($> 150°$C) and a stamp with the desired pattern is imprinted onto PMMA. After cooling, the stamp is removed, and a negative pattern of the stamp appears. As regards the stamp, this can be made by any method of lithography. A detailed description of the NIL technique is to find in [52].

The used surfaces with the patterns (or grooves) were fabricated by Theodore Nielsen [52]. The width of the grooves is 25 μm and the distance between the

grooves is 100 μm. This is shown in Fig 5.21. Hereafter, the surface was etched in the RIE, by following the above mentioned recipe for etching BS surfaces, and coated with Teflon®, subsequently.
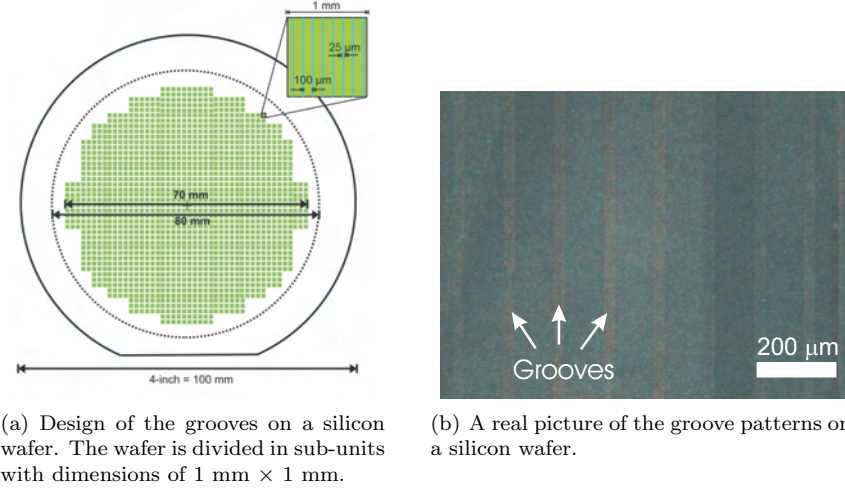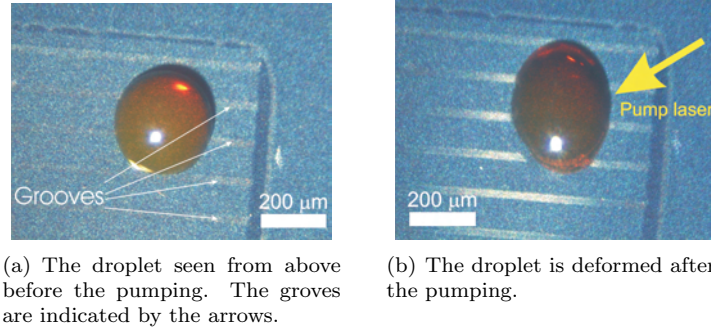

(a) Design of the grooves on a silicon wafer. The wafer is divided in sub-units with dimensions of 1 mm × 1 mm.

(b) A real picture of the groove patterns on a silicon wafer.

Figure 5.21: The groove width is 25 μm and the distance between them is 100 μm.

(a) The droplet seen from above before the pumping. The groves are indicated by the arrows.

(b) The droplet is deformed after the pumping.

Figure 5.22: A droplet placed on a BS surface coated with Teflon® before and after being pumped with an external laser.

Even though the BS-groove surfaces were not completely capable in preventing the droplet deformation after the pumping, the occurrence of this was however reduced. The rate indicating the decrease of the deformation can not be stated, since no systematic investigation of this effect was carried out due to the lack of time, Fig 5.22.

5.6 Scanning Electron Microscope

Before ending this chapter, a brief description of the used clean room tool: Scanning Electron Microscope (SEM) is given. In this project, the SEM was used to examine, categorize and judge the fine structures and features, typically in the nano-metre range, of a surface. The SEM is a microscope that uses electrons rather than light to produce high resolution images of a sample surface. A typical SEM configuration is shown in Fig 5.23.

The electron beam is emitted from a tungsten and is attracted through an anode. The electron beam, which typically has an energy ranging from a few keV to 50 keV, is focused by two successive condenser lenses into a beam with a very fine spot size (5 nm). The scan coils are energized (by varying the voltage produced by the scan generator) and create a magnetic field which deflects the beam back and forth in a controlled pattern. As the primary electron beam hits the sample, it produces a secondary electrons from the sample. These electrons are collected by a secondary detector (backscatter detector), converted to a voltage and amplified. The amplified signal is displayed as pixels on a Cathode-ray tube (CRT) whose intensity is determined by this number.
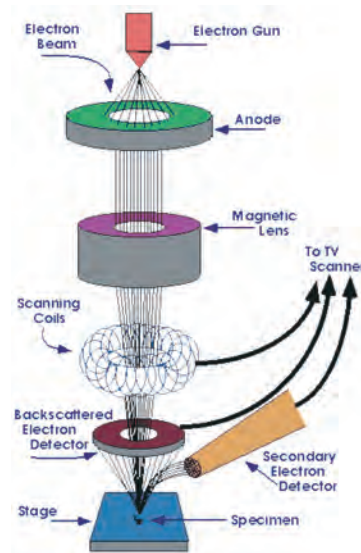

Figure 5.23: SEM configuration [53].

Chapter 6

Materials and Setup

The idea behind the setup build and used in this project was to integrate two types measurement setups in one. It has to be possible to carry out spectra measurements on the droplet simultaneously with shape and contact angle measurements of the same droplet. In the subsequent sections a description of vital parts of the setup plus the small belonging together parts that eases and improves the measure outputs and measurements is given. The method followed in creating the droplets is given in Section 6.5. The chapter is ended with Section 6.6 describing the setup as a unified whole.

6.1   The Metallic Setup Box

A setup box was specially build for the purpose. During the design of this setup box, a series of considerations about some specific demands that had to be be fulfilled in order to be able to use it for the liquid droplet laser, was made as follows

- A 90° rotational arm allowing the coupled microscope to rotate in order to view the droplet from the top (shape measurements) and from the side to measure the contact angle.

- The stage on which the droplet is placed has to be 8 mm away from the microscope objective lens (the focal length).

- The walls of the setup box has to be painted in black in an attempt to prevent the dangerous laser light reflections.

Fig 6.1 shows the ready-made aluminium setup box. The box was build up by three plates. On one of the three plates the stage was mounted. On the second, a rail was made so the mounted microscope could rotate freely. The third plate defines the base of the construction. It should be noted that the distance from the stage and the microscope lens is made variable, so that the desired distance can be set. Fig 6.2 and Fig 6.3 shows pictures of the droplet viewed by the coupled microscope from different angles.
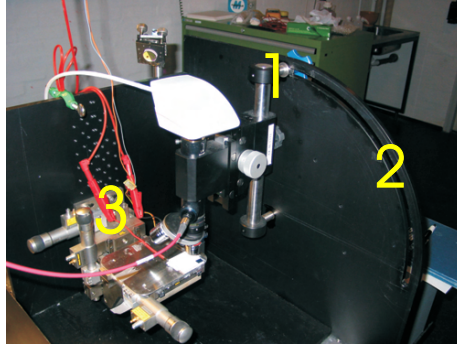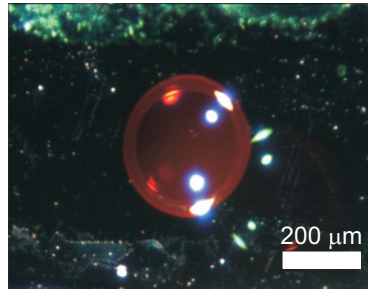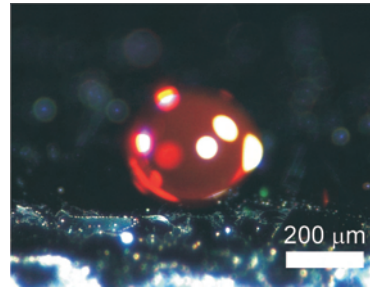
Figure 6.1: The build and used setup box with 1) The rotating arm, 2) the rail and 3) the metallic stage.
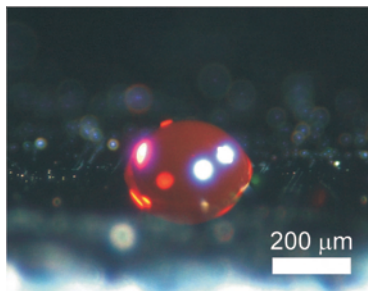

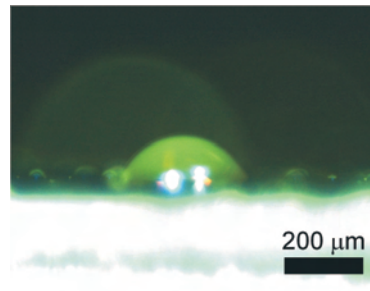(a) A microscope picture of the droplet seen from above (at an angle 90°).

(b) The droplet seen from an angle of 45°.

Figure 6.2: The microscope pictures of the droplet in angles: 90° and 45°.

(a) The droplet seen from an angle of 30°.

(b) A side view of the droplet at an angle of 0°. The green color of the droplet is due to the used microscope filter.

Figure 6.3: The microscope pictures of the droplet in angles: 30° and 0°.

6.2 The Microscope System

6.2.1 The TV-microscope

In principle, the used Leica TV-microscope, works in the same way as conventional microscopes. A focal lens with a $5\times$ magnification, placed at the bottom of the system, collects the light, i.e a sample picture, from the sample and focuses it to a build-in camera. In the middle of the microscope pipe system, a beam-splitter is placed, as shown in Fig 6.4, in order to reflect the half of the collected light to the optical fiber, the reason why this is mounted to measure the spectrum simultaneously with the droplet shape measurements as will be described in the following section. The other half of the light passes by to the microscope camera. After the mounting of the optical fiber, we encountered a little technical problem, that the reflected light from the beam-splitter was not focused into the optical fiber, which means that a big part of light is lost, and the optical fiber does not detect anything. This is due to that the beam-splitter was placed in an distorted angle. By placing a tinfoil wedge as shown in Fig 6.4, the reflected light was focused onto the center of the optical fiber. The mounted microscope camera was connected to the PC via an USB port. And with an installed software called Leica, it was possible to take pictures of the droplet. The displayed picture had dimensions 1 mm $\times$ 700 μm.
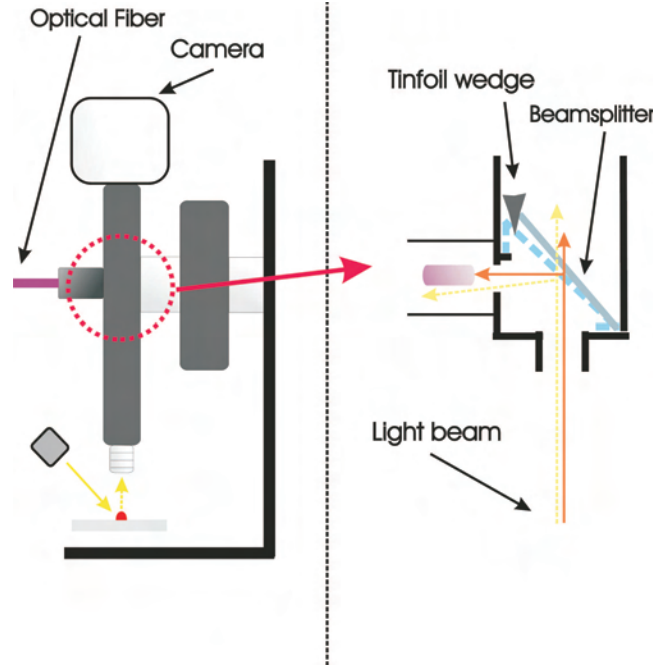

Figure 6.4: The microscope setup (left). A zoom-in picture of the inner part of the microscope pipe system (right). Before the placement of tinfoil wedge the emitted light from the liquid droplet dye laser (the dashed yellow line) was not reflected into the optical fiber by the beam-splitter (the dashed blue line). After the placement of the tinfoil wedge the half of the reflected light was focused into the optical fiber (the orange line) by the beam-splitter (the gray-blue line).

6.2.2 The Spectrometer and The Optical Fiber

The laser light emitted from the droplet is collected by an optical fiber connected to a spectrometer. The optical fiber has a pure silica core and a fluorine doped fused silica cladding which is a low index of refraction material cladding, in order to get the light guiding effect. In order to measure the laser light simultaneous with the contact angle measurement, the optical fiber was mounted on the build-in microscope. Fig 6.5 shows the spectrum measured, for the droplet shown in Fig 6.6, before and after the optical fiber have being mounted. Although the fluorescence area, for the optical fiber mounted on the microscope is a bit damped, where the intensity is reduced by the half, compared to when un-mounted on the microscope, it is still quit useful, since we operate with the relative intensity and the spectrum profile is nearly the same. The damping of the intensity is due to the above mentioned beam-splitter mounted within the microscope pipe system halving the received signal focused to the optical fiber and thereby halving light intensity.
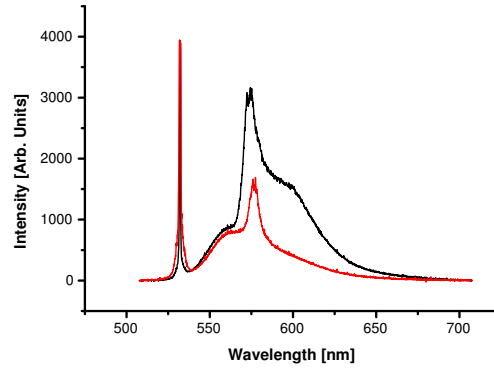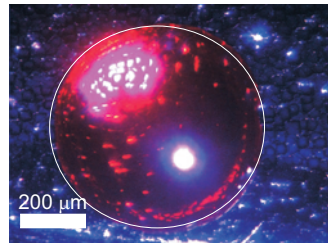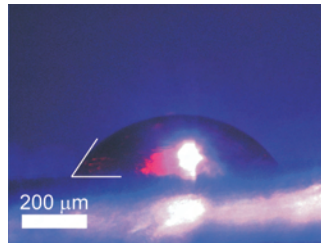

Figure 6.5: The laser spectrum for the droplet shown in Fig 6.6 at pump power 35 mW. The black line shows the spectrum with the optical fiber unmounted on the microscope. The red line shows the spectrum with the optical fiber mounted on the microscope.

(a) The droplet seen from above.   (b) A side view of the droplet.

Figure 6.6: The droplet for which the spectrum shown in Fig 6.5 belongs.

The spectrometer from Avantes (AVS-USB2000) is a 2048-element Charge Coupled Device (CCD) array detector. The light from the optical fiber is transmitted to the spectrometer and diffracted by a plane grating and then focused by a spherical mirror dispersing the different wavelengths across a CCD array. The CCD responds by generating a voltage that is proportional to the signal at each of the different dispersed wavelengths. This enables a simultaneous measurement of all the wavelengths. The spectrometer is connected directly to a PC via an USB port. The operation of the spectrometer is shown in Fig 6.7. Since the spectrometer has not being calibrated for a certain light source, it measures the light intensity in arbitrary units, i.e. only the relative output is measured.
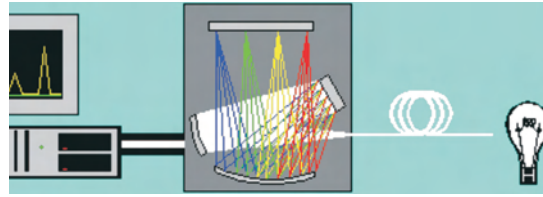

Figure 6.7: The operation of the spectrometer [55].

6.3   The Pump Laser

A so-called Nd:YAG laser setup is utilized for the optical characterization. The neodymium ions Nd^{3+} are doped into yttrium-aluminum-garnet (YAG) crystal producing what is referred to as an Nd:YAG laser. The pumping scheme is a four-level system. The emitted laser light is of the fundamental infra-red wave with wavelength 1064 nm. However, a frequency-doubling crystal placed inside the laser enables a generation of the second harmonic with the wavelength 532 nm.

The wavelength 1064 nm is filtered out by placing a frequency splitter permitting only the laser to emit with wavelength 532 nm. The laser light is emitted in pulses with a duration of 5 ns per pulse at 532 nm. The repetition rate of the pulses appear with a frequency of 10 Hz. The energy of each pulse can be up to 220 mJ corresponding to an effect of 44 MW per pulse. Thus the continuous effect is 2.2 W. More about the Nd:YAG output power in Section 7.1. After the frequency splitter an attenuator is placed in order to damp the powerful laser output by approximately 90 %. The Nd:YAG is varied by the flash-lamp voltage. The model used is Continuum, Surelite I-10.

6.4   The Peltier Element

The peltier element is a simple cooling element. The idea of using a peltier element originated as we in the beginning observed a rapid evaporation of the EG droplet during the pumping what limits the time of the measurements. It was therefore exceedingly necessary to use a cooling instrument able to reduce the evaporation rate and thereby increase the time of the measurements. More about the evaporation of the EG droplet in Section 7.2.

The mode of operation of the peltier element is superficially described as follows. A peltier is an electronic package that consists of two parallel ceramic plates with an array of small Bismuth telluride cubes (p and n type semiconductor elements connected in series) in between. By applying a DC voltage, heat is transferred from the cold side of the device to the hot side. The cold side is the side used to cool our droplet. The hot side requires a heat-sinker to remove the heat from the hot side to someplace else. If not, the cold side gets hot. That is why the peltier element is placed on a (10 cm×10 cm) metallic plate, serving as heat absorber, and additionally cooled by a CPU cooler, lying straight below the metallic plate, i.e the heat-sinker. The more efficient the removal of heat from the hot side, the colder the cold side will become. If the current is reversed the cold side gets hot and vice versa.

The physical explanation for the peltier effect is that the electrons speeds up or slow depending on the applied current. When speeding up the kinetic of the electrons turns into heat. And when slowed the kinetic energy decreases, and the temperature falls down. In the light of the p- and n-type semiconductor, the electrons are forced to move from the p- to the n-type when applying a DC voltage.

The peltier element used in this project was 4 cm×4 cm×4.7 mm in dimension, Fig 6.8, and required a maximal power supply of 65 W for cooling. The maximum reached cooling temperature under the existing conditions; i.e. room temperature and the limited cooling of the heat-sinker plate, was measured to about 11°C for a mean pump power of about 20 mW.
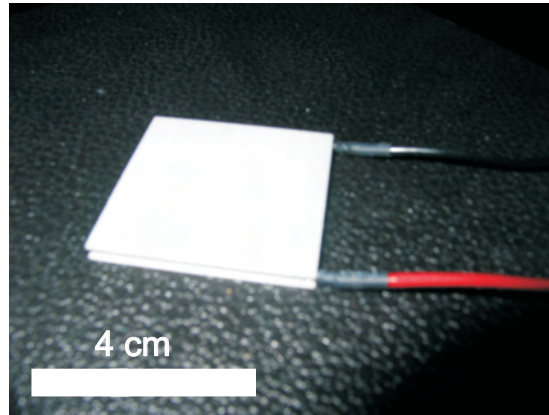

Figure 6.8: The peltier element.

6.5 Droplet Creation

6.5.1 The Spraying Technique and Pipette

In the beginning, the first idea was to either use the pipette or the spraying technique. However, later on, it showed that both techniques did not work. The large volume, i.e. 1 μL, plus control difficulties made the the pipette useless; and the spraying technique was impractical especially when one has to pick a single droplet and remove the others.

6.5.2 The TOPS-IN Pins

The nano-instrumentation company TOPS-PIN [54] has developed a silicon microfabricated pins for dispensing of liquids. Even though these pins are primary used for fabrication of DNA-arrays, I tested them in creating EG micro-droplets. The pin is manufactured with a combination of silicon and stainless materials
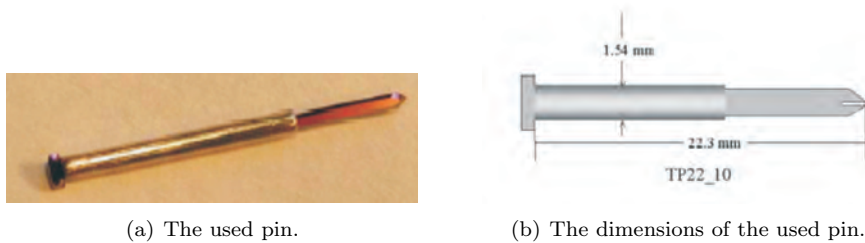

(a) The used pin.

(b) The dimensions of the used pin.

Figure 6.9: The used pin from developed by Topspin [54].

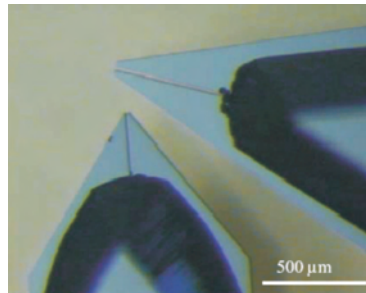
Figure 6.10: A close up view of the tip apex with a 10 μm wide channel [54].

and is 22.3 mm long as shown in Fig 6.9. The pin is then placed in a microarray robot and moves in the holder in a vertical position with the tip down. By dipping the tip of the pin in a well plate it aspirates liquid here from. Because of capillary forces the liquid is pulled up into the slot and into a closed cavity; Fig 6.10. The closed cavity prevents the liquid from evaporating. Hereafter, the robot moves the attached pin over the surface dispensing the droplets of the liquid when the tip touches the surface. The pin is able to deposit sub-nano-liter amounts of liquid onto the surface. The prints of the pin is uniformly

homogeneous and circular in shape from the first to the last spot. In our case

(a) The produced spots of the used pin.

(b) A close up view of 6.11(a). Notice the evaporation of liquid indicated by the white spots in the center of the drops.
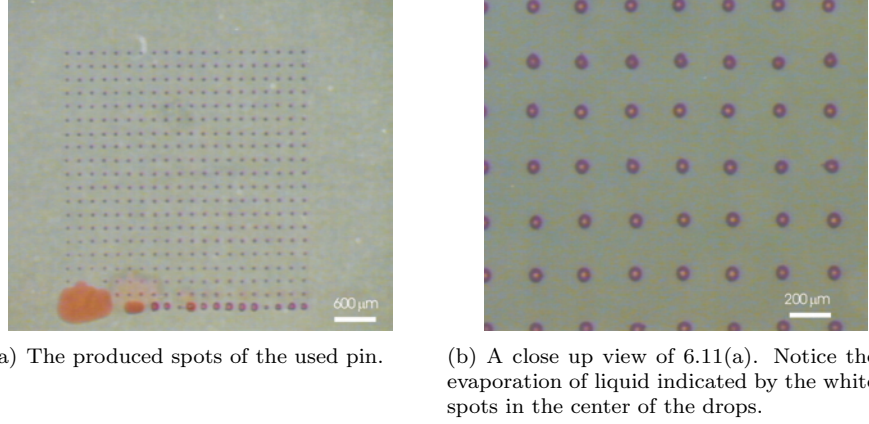
Figure 6.11: A picture of the produced spots (or drops) on hydrophilic surfaces.

the well was filled with EG. Fig 6.11 shows the produced spots of the used pin. A combination of the factor of low surface tension [1] (low hydrophobicity) and the extremely high evaporation rate of the droplets with a typical radius of 15 μm, resulted in completely flattened and nearly fully evaporated droplets. Few minutes after the dispensing, only the previously dissolved Rh6G is left on the surface as shown in Fig 6.11(b). The dispensing was tried on highly hydrophobic surfaces, but the very small droplets would not sit on these surfaces; probably because of the fakir effect. Unfortunately, the TOPS-IN pins could not be used.

6.5.3 The Dip Pen Method

Besides being the simplest method, the dip pen method turned to be the most useful, serviceable and practical method. A normal sized plastic pipette is filled with Rh6G dissolved in EG liquid. By manually applying an appropriate amount of pressure on the liquid; i.e. by pressing the top of the syringe filled with liquid, a micro-droplet will be created down the slot. Only the micro-droplet is tried to touch the surface, not the pipette; this will deform the shape of the droplet. By ensuring that only the droplet is touching the surface, the surface tension would do the job and ensure a spherical shape of the droplet. This method requires patience and experience in order to get beautiful spherical droplets. All the droplets reported in this project, except from those reported in Section 7.4, are created by the dip pen method. Naturally, this method has the disadvantage that it is limited to producing only micro-droplets. The sought after nano-droplets [2] is not possible with this method, since it can not be done manually.

---

[1]The used surface in the robot is the only allowed glass surface, which is hydrophilic.
[2]With nano-droplets we mean droplets with radii in nano range.

6.6 The Nd:YAG Laser Setup

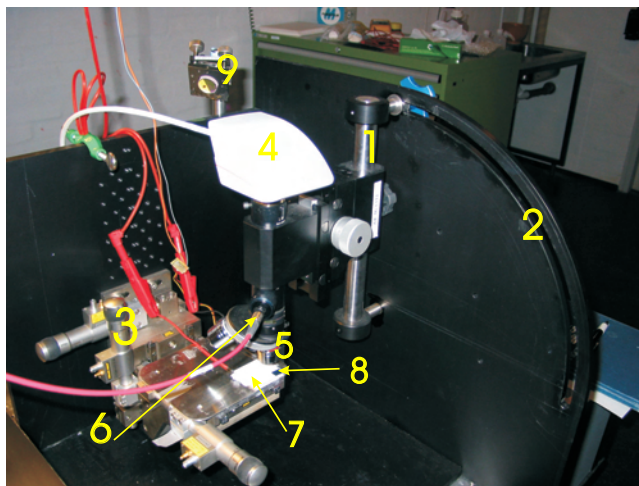The setup box viewed as a unified whole is shown in Fig 6.12. To begin with a

Figure 6.12: The setup box consisting of a 1) the rotating arm, 2) the rail, 3) the metallic stage, 4) the microscope camera, 5) the microscope lens, 6) the optical fiber, 7) the peltier element, 8) the hydrophobic surface and 9) the reflecting mirror with the wood wedge.

so-called heat conducting paste, improving the conductivity of the heat between two metals, was smeared on both the top and underneath the peltier element. This was placed on a heat-sinker which in advance was placed on a the metallic stage mounted on the aluminium black box. A silicon ethylene-glycol-phobic surface was then placed on the peltier element. A digital thermometer was hereafter mounted onto the silicon surface in order to measure and control the temperature of the droplet. A droplet was created and placed onto the surface of the silicon wafer by using a syringe, consisting of Rhodamine 6G dissolved in ethylene glycol with the concentration $2 \cdot 10^{-2}$ mol/L. Both the peltier element and the CPU cooler were turned on. The temperature of the surface and hence of the droplet was measured to $11°C$. The beam from the Nd:YAG laser (532 nm) was guided by a series of mirrors down onto the micro-droplet dye laser. A wood wedge is placed on the last reflecting mirror (the fourth mirror in Fig 6.13), to guide the beam down onto the droplet. The incline of the wedge determined by geometrical calculations, had to form an angle of about $22°C$ in order to strike the droplet. The output power of the pump laser beam was measured by a Power Meter (Coherent Field Master GS). The Power Meter is not sensitive for power less than 1-2 mW. The emitted light from the micro-droplet dye laser and the scattered pumping laser light was collected by the optical fiber mounted in the microscope system, which then was analyzed by the Spectro-meter.
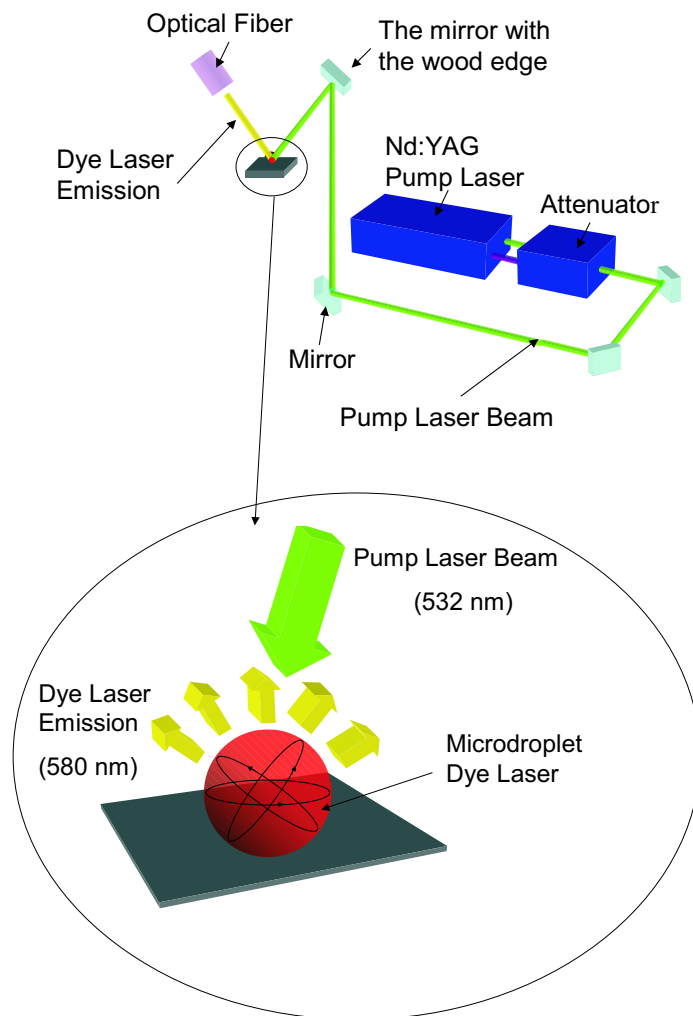
Figure 6.13: The Nd:YAG laser setup and the belonging mirrors guiding the light to the droplet (picture at the top). A close up view of the droplet placed on the surface (picture at the bottom) emitting laser light. The circulating inside the droplet indicates the WGM occuring within the droplet.

Chapter 7

Optical Characterization

In this chapter the optical characterization of the liquid micro-droplet dye laser is presented. Firstly, the chapter is introduced by some considerations about the optical pumping light, Section 7.1, followed by Section 7.2 where EG droplet evaporation measurements is presented. The lasing spectra for the droplet dye lying on various surface types and the levitated droplet dye is given in Section 7.3 and Section 7.4, respectively. The chapter is ended by section 7.5 where the results are summarized.

7.1 Optical Pumping Light

As described is Section 6.3, the output beam power of the Nd:YAG laser is varied by the flash-lamp voltage. Although, the voltage U of the flash tubes in the Nd:YAG laser can be controlled and thereby the output power P of the Nd:YAG laser, the reading based solely on the flash tube can not directly be converted to an output power value; i.e there are meaningless, since the attenuator can be varied and thereby the output power P still for a fixed flash tube voltage. In order to determine the pulse energy for the Nd:YAG laser, this is therefore measured by a power meter for varying flash tube voltage U, and for a fixed attenuator value. The power meter is placed in the path of the laser beam. The results of the measurements for the mean power power P of the Nd:YAG laser as a function of the flash tube voltage U is shown on Fig 7.1. The relation between the mean pump power P and the flash tubes U is close to quadratic for small voltage values given by

$$P = 614 \frac{\text{mW}}{(\text{kV})^2} U^2 - 1017 \frac{\text{mW}}{\text{kV}} U + 414 \text{ mW}. \tag{7.1}$$

For high voltages the relation is linear. The expression above is used to convert the flash voltages to the mean power.

Having expressed the mean pump power as a function of the flash voltage, it will be interesting to determine the approximative energy that is transferred to the dye droplet by a single pulse. Since many droplets showed to have laser threshold values around 25 mW, as will be shown in the coming sections, this is used as a numerical example. A single pulse from Nd:YAG laser is emitted with a repetition $\nu = 10$ Hz and lasts in $\tau = 5$ ns. The total energy in a single
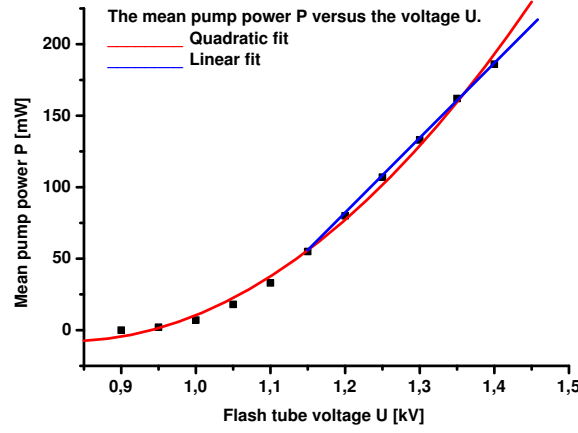
Figure 7.1: The measured mean pump power P depicted as a function of the flash tube voltage U. For small voltage values we notice a quadratic behavior, but for high voltages the behavior of the relation becomes linear.

pulse is thus given by

$$E_{\text{total}} = \frac{P}{\nu} = \frac{25 \text{ mW}}{10 \text{ Hz}} = 2.5 \text{ mJ}. \tag{7.2}$$

Lasting the time τ, this gives a power

$$P_{\text{total}} = \frac{E_{\text{total}}}{\tau} = 0.5 \text{ MW}, \tag{7.3}$$

which is an extremely high pump power value. The diameter d_{laser} of the laser beam (from the Nd:YAG laser) is measured to about 6 mm. Assuming a uniformly distribution of energy across the laser beam, the transferred energy flux pr. area F_{laser} is thus given by

$$F_{\text{laser}} = \frac{E_{\text{total}}}{\pi \left(d_{\text{laser}}/2 \right)^2} = 88 \frac{\mu J}{mm^2} \tag{7.4}$$

Assuming the simplest intensity profile of the laser beam namely as a constant function across the beam the energy transferred to the liquid droplet dye gain is given as a the ratio between the droplet surface area and the cross-section area of the beam. Assuming furthermore, the half of the droplet, with radius $R = 300$ μm for instance, being exposed (pumped) to the laser beam, the surface area of this is then given by $A_{\text{half droplet}} = (4\pi R^2)/2$. The transferred energy E_{transfer} to the droplet is thus given by

$$E_{\text{transfer}} = \frac{2\pi R^2}{\pi \left(d_{\text{laser}}/2 \right)^2} E_{\text{total}} = 0.02 E_{\text{total}}. \tag{7.5}$$

About 2 % of the pulse energy is delivered to the liquid droplet dye when pumped with a mean pump power 25 mW.

## 7.2 Evaporation of The Ethylene Glycol Droplet

7.2.1 Evaporation Rate

As mentioned before, we are interested in a dye solvent with a low evaporation rate for the creation of a droplet. An ethanol droplet was observed to evaporate few seconds after its creation, whereas the evaporation rate of an EG droplet was observed to be more slow and gradual. Based on picture analysis of the droplet, the evaporation rate of an EG droplet was measured. Fig 7.2-7.5 shows a series pictures of an EG droplet lying on a surface during more than 60 minutes. If we imagine the droplet sitting on a surface as a spherical cap, the volume $V_{droplet}$ of the droplet will be given by the following expression [56]

$$V_{droplet} = \frac{1}{3}\pi h^2(\frac{3}{2}d - h) \tag{7.6}$$

where h is the hight of the droplet, i.e. the perpendicular distance between the surface and the top point of the droplet surface. d is the virtual diameter of the droplet. Since the droplet lying on the surface is hemispherical, this is indicated by the white circle on the pictures and the virtual diameter is depicted as the diameter of the white circle.

As it clearly emerges from the picture series of the droplet, the circular shape of droplet seen from above remained nearly constant during evaporation; the reason why we could use the expression for the volume droplet. Only the height decreased significantly, which is sufficient for determining the volume droplet. The results given by the picture analysis of the decrease of the volume droplet due to evaporation as a function of time is depicted in Fig 7.6. The evaporation rate was observed to be linear and was determined as the slope of the linear fit to 2.4 nL/min, limiting the measurement time to few minutes since we are interested to perform a series of measurements on the droplet that last for more than few minutes. Add to this that we are interested to measure laser spectra for the same droplet, i.e. un-evaporated droplet. This evaporation rate was measured while the droplet was exposed to barely illumination from the microscope light resulting in a temperature lying a bit below room temperature namely at $T = 25°C$. Approximately 20 % and 50 % of the droplet liquid was evaporated after 23 min and 44 min, respectively. More than 80 % of the droplet was evaporated after more than 1 hour.
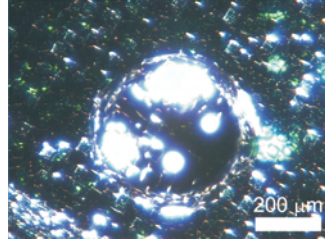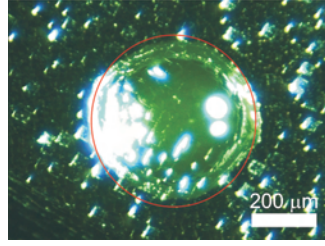
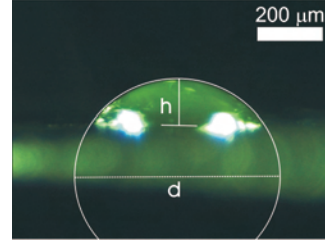(a) The spherical shaped droplet seen from above.
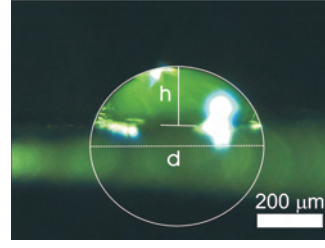
(b) A side view of the droplet. The virtual diameter and the hight are measured to $d = 520$ μm and $h = 168$ μm, respectively.

Figure 7.2: An EG droplet placed on a rough silicon teflon$^{\textregistered}$-coated surface at time $t = 0$ min.
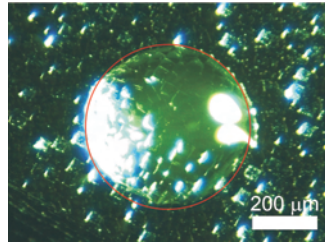

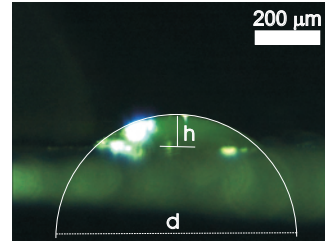(a) The spherical shaped droplet, indicated by the red circle, seen from above.

(b) A side view of the droplet. The virtual diameter and the hight are measured to $d = 585$ μm and $h = 136$ μm, respectively.

Figure 7.3: An EG droplet placed on a rough silicon teflon$^{\textregistered}$-coated surface at time $t = 23$ min.

(a) The spherical shaped droplet, indicated by the red circle, seen from above.

(b) A side view of the droplet. The virtual diameter and the hight are measured to $d = 670$ μm and $h = 96$ μm, respectively.

Figure 7.4: An EG droplet placed on a rough silicon teflon$^{\textregistered}$-coated surface at time $t = 44$ min.

(a) The spherical shaped droplet, indicated by the red circle, seen from above.

(b) A side view of the droplet. The virtual diameter and the hight are measured to $d = 880 \ \mu$m and $h = 50 \ \mu$m, respectively.
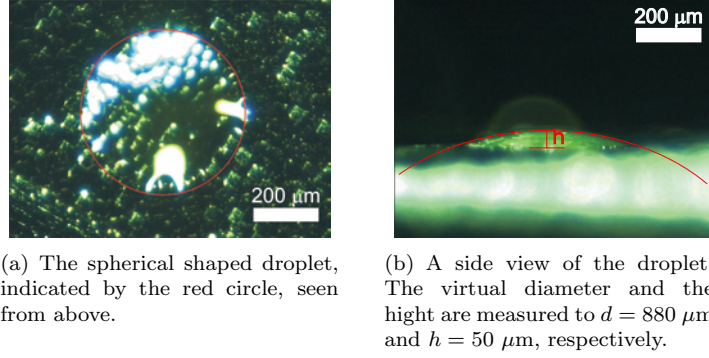
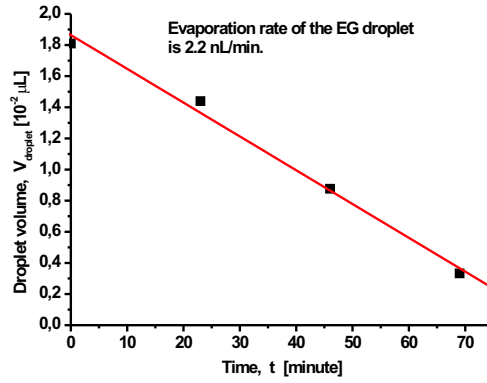Figure 7.5: An EG droplet placed on a rough silicon teflon®-coated surface at time $t = 67$ min.

Figure 7.6: The droplet volume $V_{droplet}$ depicted as a function of the time t. The evaporation rate is the slope of the linear fit. The evaporation rate is determined to be 2.4 nL/min at temperature $T = 25°$C.

7.2.2 Evaporation Rate with The Use of The Peltier Element During Pump Lasing

As mentioned in Section 6.4, the EG droplet was observed to evaporate rapidly, during the pumping and thereby decreasing the measurement time. It was therefore compelling to use a peltier cooling element in order to limit the evaporation rate of the EG droplet during pumping.

(a) The droplet before the pump-
ing.

(b) The remaining of the evapo-
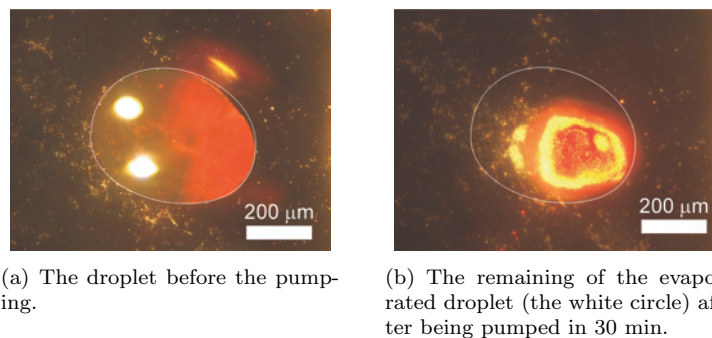rated droplet (the white circle) af-
ter being pumped in 30 min.

Figure 7.7: The droplet placed on a gold surface before the use of the peltier
element. Although, the used surface is hydrophilic (gold) and the shape of the
droplet non-spherical, it still gives a qualitative picture of the rapid evaporation
of the droplet during the pumping.

(a) The droplet before the pump-
ing.

(b) The droplet remains nearly un-
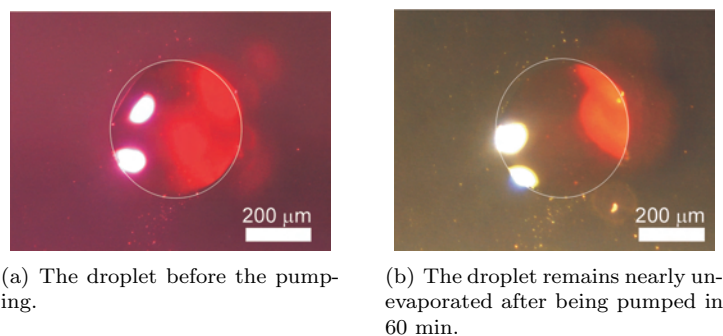evaporated after being pumped in
60 min.

Figure 7.8: The droplet placed on a gold surface after the placing and use of
the peltier element.

Fig 7.7 and 7.8 shows the EG droplet during the pumping before and after
the use of the peltier element. Without the peltier element, the liquid droplet
evaporated, after being pumped in 30 minutes leaving only the Rh6G powder
at the surface, as it emerges from Fig 7.7(b). The white circle in Fig 7.7(b),
indicating the initial shape of the droplet, reveals a rapid evaporation of the
evaporated droplet during the pumping. Following the same procedure as in
the previous section, the decrease of the volume droplet, during the pumping
before and after the use of the peltier element, is depicted versus time in Fig
7.9. Although the evaporation rate of the droplet during pumping after the use
of the peltier element is shown increasing; i.e meaning that the volume of the
droplet increases which physically is impossible unless the water vapor around
the droplet condense to water liquid [1] because of the cooling, this should be
taken with a grain salt. Due to the un-spherical shape of the droplet and the
uncertainties connected to the picture analysis, the results only give a qualitative

---

[1]If this is the case, the water will increase the polarity of the EG droplet and thereby lower
the quantum yield of the dye Rh6G.

picture of the evaporation rate. In this case, based on the graph, it is properly to ascertain that the evaporation rate with the use of the cooling element remains constant contrary to the evaporation rate without the use of the peltier element. More than 85 % of the droplet was evaporated only after 30 min during the pumping without the use of the peltier element. The time measurement was thus extended to about 60 min. It should be noted that the measured temperature T of the surface on which the droplet sits (and thereby the droplet presumably) was about 16°C during the pumping ($P = 20$ mW) with the peltier element turned on.

Since the droplet did not evaporate during the pumping with the peltier element turned on, the droplet would presumably not evaporate either if not pumped. The obtained temperature results of the surface for various apparatus configurations is listed in Table 7.1.
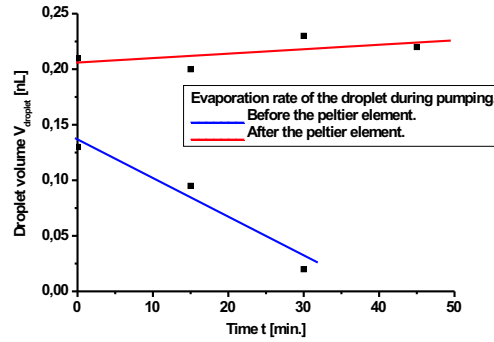

Figure 7.9: The evaporation rate of the EG droplet during pumping before and after the use of the peltier element.

| | Apparatus | | |
Temperature T	Peltier	Microscope light	Nd:YAG laser
22°C	÷	÷	÷
25°C	÷	✓	÷
11°C	✓	÷	÷
14°C	✓	✓	÷
16°C	✓	÷	✓

Table 7.1: The measured temperature of the surface on which the droplet lyes for various apparatus configurations. Symbols (✓) and (÷) indicates whether the respective apparatus is turned ON or OFF, respectively. The mean pump power of the Nd:YAG is 20 mW.

7.3 Lasing Measurements

The lasing spectra presented in this section are for droplet with varying radii all consisting of laser dye Rh6G dissolved in EG with the concentration of $2 \cdot 10^{-2}$

mol/L, and were optically pumped (at 532 nm) by an external frequency doubled Nd:YAG laser as described in Section 6.6. The following three various surfaces were chosen as the underlay for the droplet:

- The rough silicon surface deposited with fluorocarbon film, since this yielded the optimal contact angle among the silicon surfaces; e.g. (smooth silicon and the silicon surface coated with a layer silicon mitride). See Section 5.2.

- The BS surface deposited with fluorocarbon film.

- The fluorocarbon-deposited BS surface with the grooves.

7.3.1 Droplet Dye Laser on A Rough Si-fluorocarbon Surface

Fig 7.11 shows the typical measured spectra from the EG droplet labelled (A) shown in Fig 7.10 containing Rh6G. The droplet (A), placed on a rough Si-surface deposited with fluorocarbon film, is measured to have a radius of 150 μm and a contact angle 67°. The laser emission spectra located about 577-580 nm is the emitted light from the dye droplet and displays a multi-mode structure. The integration time of the spectro-meter was set to 10 sec. At an optical pumping power of 166 mW, a distinct peak with approximately 7 nm full width at half maximum (FWHM) line width appears on top of the 20 nm wide fluorescence from the Rh6G laser dye.

A plot of the emitted output power from the dye droplet versus optical pump power, shown in Fig 7.12, reveals the lasing characteristics of the system, with threshold, indicated as a bend on the curve for lasing around 110 mW, similar to the efficiency curve, Fig 3.2, explained in Section 3.2. Threshold occurred because the gain of the laser medium exceeded the sum of the cavity losses. Above threshold the cavity mode output intensity increase abruptly with pump laser.
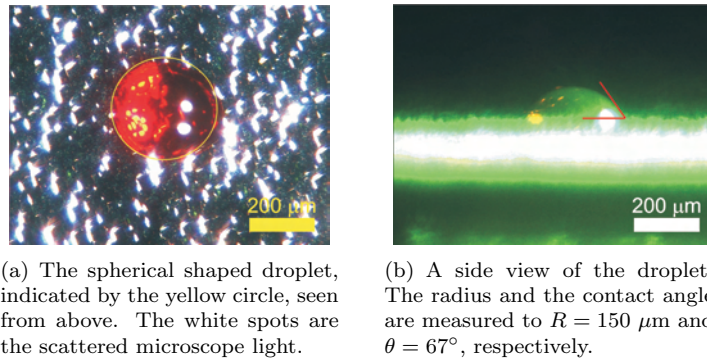

(a) The spherical shaped droplet, indicated by the yellow circle, seen from above. The white spots are the scattered microscope light.

(b) A side view of the droplet. The radius and the contact angle are measured to $R = 150$ μm and $\theta = 67°$, respectively.

Figure 7.10: An EG droplet (A) containing Rh6G placed on a rough silicon surface deposited with fluorocarbon film.

Laser Spectra

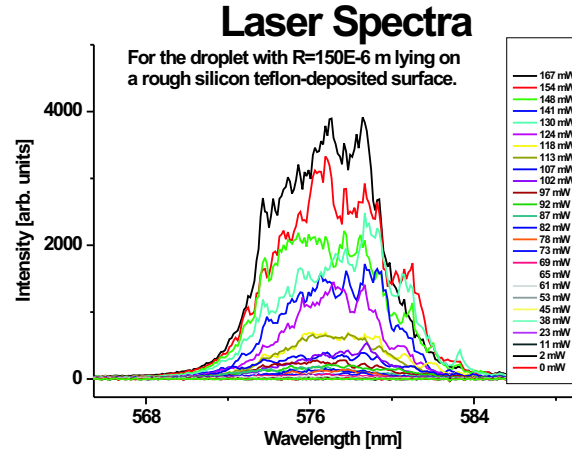**For the droplet with R=150E-6 m lying on a rough silicon teflon-deposited surface.**

Figure 7.11: The measured optical spectra for different excitation powers emitted from the micro-cavity dye laser droplet (A) with Rh6G dissolved in EG with a concentration of $2 \cdot 10^{-2}$ mol/L. Droplet (A) was placed on a hydrophobic rough silicon surface deposited with fluorocarbon. The radius of droplet (A) and the contact angle is 150 μm and 67 $^\circ$, respectively. The peak with the multi-mode system is the dye droplet laser emission spectra at wavelength about 577 nm.

Laser threshold
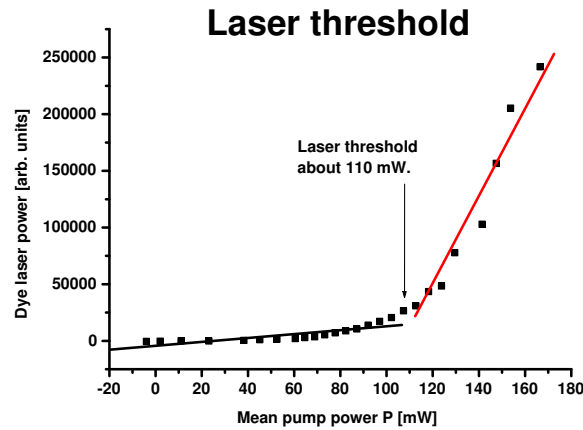
Laser threshold about 110 mW.

Figure 7.12: The emitted power from the dye droplet (A) determined as the output peak intensity of the dye laser emission spectra versus optical pump power. The threshold for lasing indicated by the bend at an excitation power of 110 mW. Droplet (A) with Rh6G dissolved in EG with a concentration of $2 \cdot 10^{-2}$ mol/L was placed on a hydrophobic rough silicon surface deposited with fluorocarbon. The radius of droplet (A) and the contact angle is 150 μm and 67 $^\circ$, respectively.
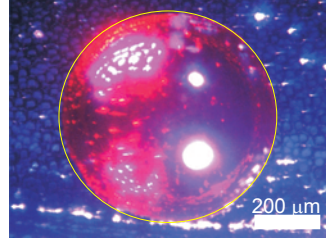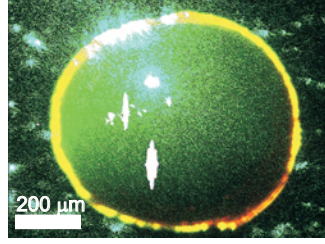
(a) The spherical shaped droplet, indicated by the yellow circle, seen from above.
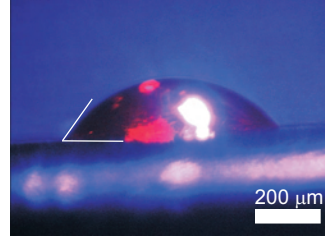
(b) A side view of the droplet. The radius and the contact angle are measured to $R = 330$ μm and $\theta = 65°$, respectively.

Figure 7.13: An EG droplet (B) containing Rh6G placed on a rough silicon surface deposited with fluorocarbon film.

(a) The droplet during lasing. The green color onto the droplet is the Nd:YAG laser beam. The yellow color at the droplet edge is the emitted dye droplet light. The circulating of the dye droplet light at the edge indicate that the droplet liquid-air and liquid-substrate functions as a WGM resonator.
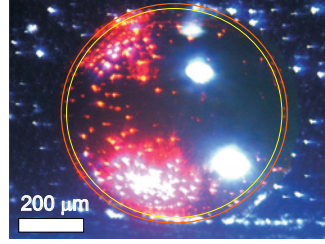
(b) The same droplet after lasing. The yellow circle indicates the droplet shape before pumping, whereas the red circle is the shape after pumping. The shape of the droplet is nearly unchanged.

Figure 7.14: The EG droplet (B) containing Rh6G with $R = 330$ μm placed on a rough silicon surface deposited with fluorocarbon film.

Fig 7.15 shows an emission spectra for droplet (B) that is double as big as droplet (A). Droplet (B) has radius $R = 330$ μm and is shown in Fig 7.13. At an optical pumping power of 35 mW, a distinct peak with approximately 6 nm FWHM appearing on top of the 26 nm is displaced about 5-6 nm towards shorter wavelengths, more specifically at 571-575 nm. In 1971, Peterson *et al.* [60] discovered that a reduction of the cavity losses results in a red shifting of the laser light. Assuming that for droplets with larger dimensions; i.e. larger radius, the travelling path for the light around the droplet circumference is longer. This may very likely result in a higher absorption rate for larger droplets increasing the cavity losses, which in the light of Peterson's discovery may explain the displacement of the emission spectra towards shorter wavelengths.
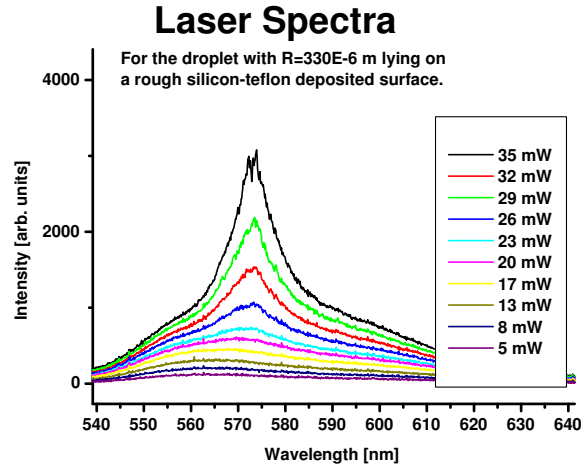
Figure 7.15: The measured optical spectra for different excitation powers emitted from the micro-cavity dye laser droplet (B) with Rh6G dissolved in EG with a concentration of $2 \cdot 10^{-2}$ mol/L. Droplet (B) was placed on a hydrophobic rough silicon surface deposited with fluorocarbon. The radius of droplet (B) and the contact angle is 330 μm and 65 °, respectively.
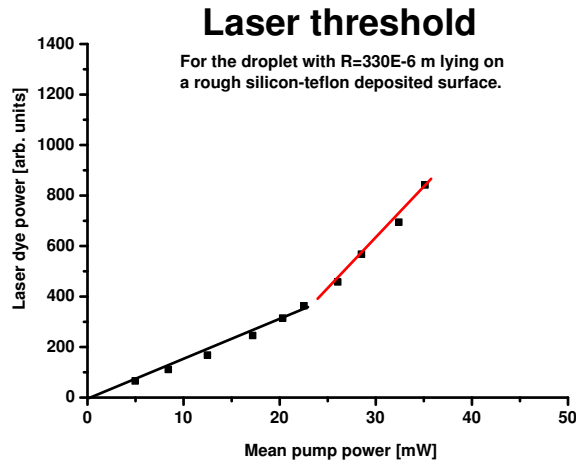

Figure 7.16: The emitted power from the dye droplet determined as the output peak intensity of the dye laser emission spectra versus optical pump power. The threshold for lasing indicated by the bend at an excitation power of 25 mW. The droplet (B) with Rh6G dissolved in EG with a concentration of $2 \cdot 10^{-2}$ mol/L was placed on a hydrophobic rough silicon surface deposited with fluorocarbon. The radius of droplet (B) and the contact angle is 330 μm and 65 °, respectively.

Fig 7.16 shows the laser threshold for droplet (B) occurring at 25 mW. This laser threshold value is about four times less than for droplet (A) (with $R = 150$ μm, threshold=110 mW) lying on the same surface. This suggests a relation between the increase of the droplet dimension and the decrease of threshold. Since the laser threshold value, as explained in Section 3.2, is the point where the gain equals the cavity loss effects, a less gain-cell (volume) requires a higher pumping power in order for the cavity system to overcome the losses. This results in a higher threshold value.

Fig 7.14 shows droplet (B) during and after lasing. The yellow color at the edge of the droplet is the emitted dye droplet light whereas the green light is from the Nd:YAG laser beam. This observation indicate that the liquid-air and liquid-solid interfaces functions as a resonator reflecting the light around the circumference of the droplet which is in agreement with the WGM resonator model. However, the resonator model also predicts that light from the dye droplet is emitted around the whole droplet. This is clearly not the case, since only the utmost circumference of the droplet is radiant and not the inner part of the droplet. This effect is observed for all the droplets lying on a surface.

In addition, it should be noted that the shape of the droplet after lasing remained nearly unchanged as shown in Fig 7.14(b).

## 7.3.2   Droplet Dye Laser on A BS Surface

Fig 7.17 shows droplet (C) with $R = 270$ μm placed on a BS fluorocarbon deposited surface. The emission spectra for droplet (C) is shown in Fig 7.19. Compared to droplet (A), the emission spectra for droplet (C) is displaced about 6 nm. More specifically, the emission spectra are centered at 584 nm. This may be interpreted by the BS surface. Because of the nano-structures characterizing the BS surface as mentioned in Section 5.4, this may absorb a part of light. The average distance between adjacent peaks and the hight of each peak on a BS surface is about 300 nm and 350 nm, respectively; Fig 5.13. These values are in the same wavelength order as the operating dye laser droplet, why a part of light presumably is trapped in the BS surface. This may result, so to say, in a reduction of the cavity losses and thereby displacing the output emission spectra towards longer wavelengths. Laser threshold for droplet (C) occurs at 26 mW, nearly at the same value as for droplet (B) lying on the rough silicon fluorocarbon deposited.

The droplets placed on the BS surface deforms during lasing. This is shown in Fig 7.17. Although the deformation is not that clear, it is however a general problem with the BS surface. A more persuasive deformation is shown for another droplet [2] in Fig 7.18. The orientation of the deformation occurred almost always orthogonal to the direction of the pump lasing. Our immediate first thought was to fabricate grooves on the BS surface in the order of the droplet dimension in order to prevent the deformation in a certain direction.

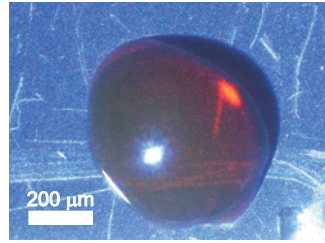[2]No emission spectra were measured for this droplet, why only the previous one was shown.
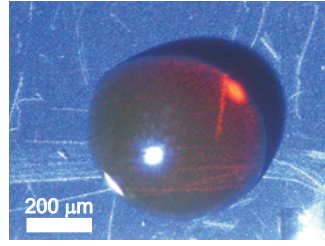
(a) The spherical shaped droplet seen from above.
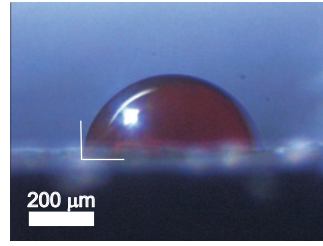
(b) A side view of the droplet. The radius and the contact angle are measured to $R = 270\ \mu$m and $\theta = 90°$, respectively.

Figure 7.17: An EG droplet (C) containing Rh6G placed on a BS surface deposited with fluorocarbon film.

(a) Droplet (C) is deformed after lasing.
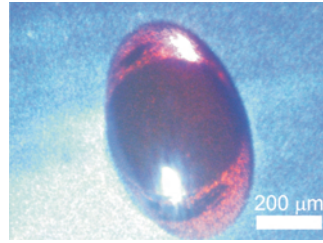
(b) A droplet placed on a BS surface coated with fluorocarbon is deformed after being pumped by an external laser.

Figure 7.18: Deformation of EG droplets placed on fluorocarbon-coated BS surface.

Figure 7.19: The measured optical spectra for different excitation powers emitted from the micro-cavity dye laser droplet (C) with Rh6G dissolved in EG with a concentration of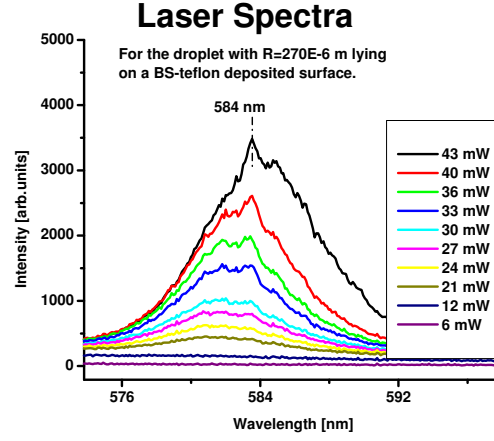 $2 \cdot 10^{-2}$ mol/L. Droplet (C) was placed on a hydrophobic BS surface deposited with fluorocarbon. The radius of droplet (C) and the contact angle is 270 μm and 90 °, respectively.

Figure 7.20: The emitted power from the dye droplet (C) determined as the output peak intensity of the dye laser emission spectra versus optical pump power. The threshold for lasing indicated by the bend at an excitation power of 26 mW. The droplet (C) with Rh6G dissolved in EG with a concentration of $2 \cdot 10^{-2}$ mol/L was placed on a hydrophobic BS surface deposited with fluorocarbon. The radius of droplet (C) and the contact angle is 270 μm and 90 °, respectively.
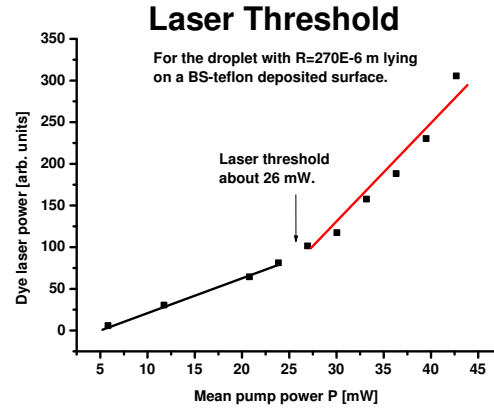
89

7.3.3 Droplet Dye Laser on A BS-groove Surface

Fig 7.22 shows the emission spectra for droplet (D) with $R = 330$ μm placed on a BS-groove fluorocarbon deposited surface shown in Fig 7.21. Since only the micron structures (grooves) are added to the BS surface, the same emission spectra displacement as for the BS surface is expected. However, the 6 nm wide peak covering a wavelength area 570-576 nm, was not displaced as with the previous droplet for unknown reasons. The laser threshold for droplet (D) was obtained at 23 mW. Although the deformation was in most cases not observed on BS-groove surfaces, yet it should be mentioned that the lasing on such surfaces was difficult to obtain for small droplets.

(a) The spherical shaped droplet seen from above.

(b) A side view of the droplet. The radius and the contact angle are measured to $R = 330$ μm and $\theta = 95°$, respectively.
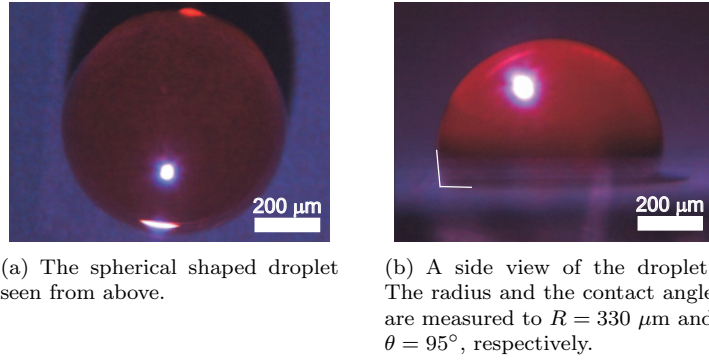
Figure 7.21: An EG droplet (D) containing Rh6G placed on a BS-groove surface deposited with fluorocarbon film.

Measurements carried out on droplet (E) with $R = 170$ μm placed on BS-groove fluorocarbon deposited surface, Fig 7.24, showed no sign of lasing, since the relation between the depicted dye laser power versus mean pump power is linear as shown in Fig 7.26. Moreover, the emission spectra is too broad, about 20-30 nm. Increasing the pump power further than 87 mW results in a saturation of the emission spectra.

Compared to lasing droplet (A) which has nearly the same dimension but lies on a different surface, this may indicate the following: Since the droplet (E) is placed on a BS surface which might absorb a part of light, the gain in the relatively small droplet can not overcome the cavity losses and thereby not develop a beam either that can sustain oscillations within the micro-cavity. Thus, the result of this will be no lasing.

Laser Spectra

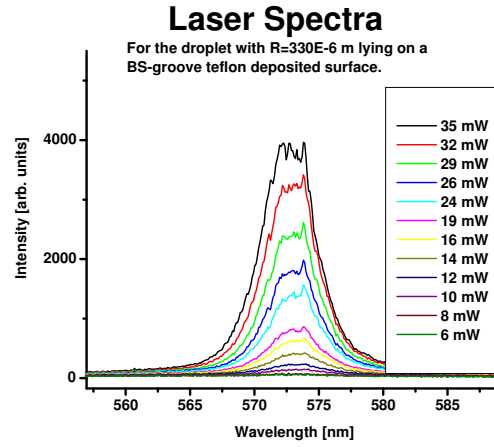**For the droplet with R=330E-6 m lying on a BS-groove teflon deposited surface.**

Figure 7.22: The measured optical spectra for different excitation powers emitted from the micro-cavity dye laser droplet (D) with Rh6G dissolved in EG with a concentration of $2 \cdot 10^{-2}$ mol/L. Droplet (D) was placed on a hydrophobic BS-groove surface deposited with fluorocarbon. The radius of droplet (D) and the contact angle is 330 μm and 95°, respectively.

Laser Threshold

For the droplet with R=330E-6 m lying on a BS-groove teflon deposited surface.

Laser threshold about 23 mW.

Figure 7.23: The emitted power from the dye droplet (D) determined as the output peak intensity of the dye laser emission spectra versus optical pump power. The threshold for lasing indicated by the bend at an excitation power of 23 mW. Droplet (D) with Rh6G dissolved in EG with a concentration of $2 \cdot 10^{-2}$ mol/L was placed on a BS surface deposited with fluorocarbon. The radius of droplet (D) and the contact angle is 330 μm and 95°, respectively.

It should be noted that emission output is tried measured from three different directions; that is from three different angles: 0°, 45° and 90°. At the angles 0° and 45°, nothing was detected. Only at the angle 90° an output was detected,

i.e. light emitted vertically to the optical fiber, which is not in agreement with the theory assuming the light to be emitted in all directions around the droplet. All the emission spectra presented in this section was measured above the droplet, i.e. at angle 90°.
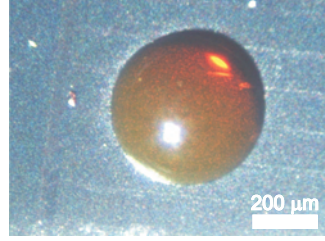
(a) The spherical shaped droplet seen from above.
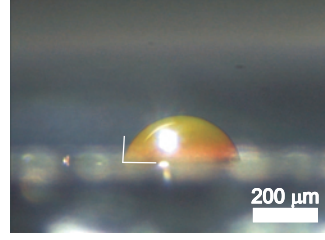
(b) A side view of the droplet. The radius and the contact angle are measured to $R = 170$ μm and $\theta = 88°$, respectively.

Figure 7.24: An EG droplet containing Rh6G placed on a BS-groove surface deposited with fluorocarbon film.

All the discussed results are listed in Table 7.2.

Surface type	Droplet types	R	Emission maximum	Laser threshold
Rough Si	A	150 μm	577-580 nm	110 mW
	B	330 μm	571-575 nm	25 mW
BS	C	270 μm	584 nm	26 mW
BS-groove	D	330 μm	570-576 nm	23 mW
	E	170 μm	566 nm	-

Table 7.2: The obtained results for laser dye droplets with different radii R lying on various fluorocarbon-coated surfaces. Note for droplet with $R = 170$ μm no threshold value is indicated, since no lasing was obtained for this droplet.
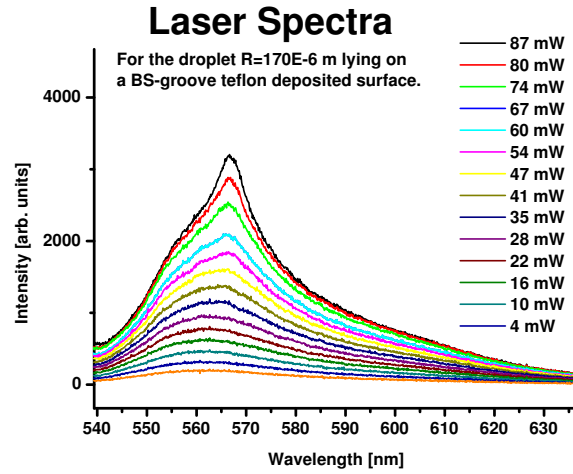
Figure 7.25: The measured optical spectra for different excitation powers emitted from the micro-cavity dye laser droplet. with Rh6G dissolved in EG with a concentration of $2 \cdot 10^{-2}$ mol/L. The droplet was placed on a hydrophobic BS-groove surface deposited with fluorocarbon. The radius of the droplet and the contact angle is 170 μm and 88°.
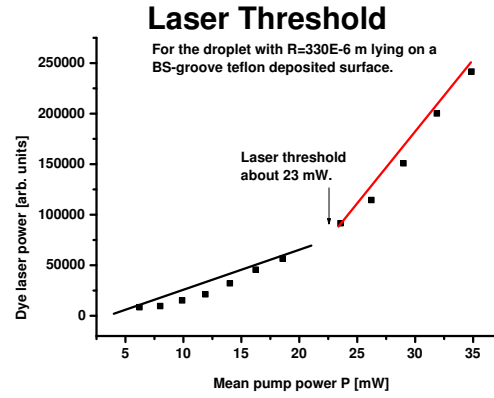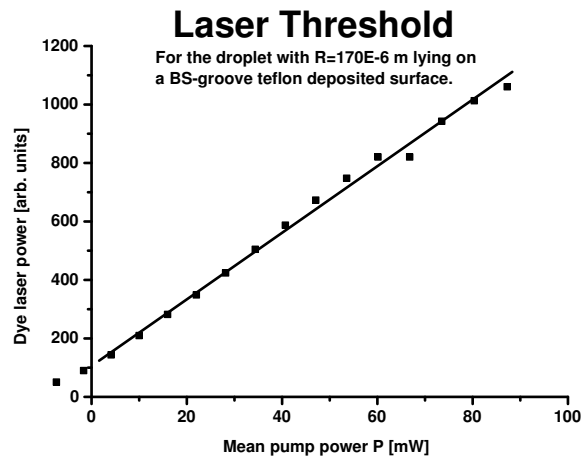

Figure 7.26: The emitted power from the dye droplet determined as the output peak intensity of the dye laser emission spectra versus optical pump power. No knee is seen on the curve, indicating that no lasing is occurring. The droplet with Rh6G dissolved in EG with a concentration of $2 \cdot 10^{-2}$ mol/L was placed on a hydrophobic rough Silicon surface deposited with fluorocarbon. The radius of the droplet and the contact angle is 170 μm and 88 °.

93

7.3.4 Mode-spacing

To measure mode-spacing, we consider for instance a close-up view, Fig 7.11, of the emission spectra shown in Fig 7.27 with the peak with excitation power 166 mW and 7 nm FWHM. But firstly it should be noted that the spectrometer resolution is 0.15 nm, which is too close to the mode-spacing values predicted by the resonator model; eq. (4.38). The mode-spacing measurements may therefore be taken with a grain of salt. The noticeable peaks could be noise as well. Nevertheless, all the noticeable peaks are marked as black vertical lines Fig 7.27. There appear to be 17 peaks with mode-spacing values varying from 0.23 nm to 0.94 nm. However, the most dominating peak (indicated with red lines), of which pattern seems to repeat, might be the micro-droplet cavity modes and not the noise. The mode-spacing for these is measured to 0.90 nm and 0.94 nm. For droplet (A) with $R = 150$ μm and an emission maximum at 577 nm, the resonator theory in Section 4.3 predicts a mode-spacing value of 0.84 nm. This is in good agreement with the measured mode-spacing values 0.90 nm and 0.94 nm.
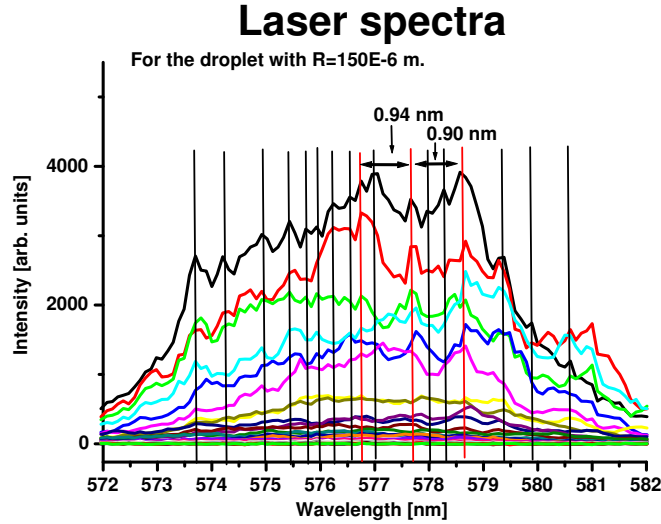
Figure 7.27: A close-up of the emission spectrum shown in Fig 7.11 in order to measure the mode-spacing for the mean pump power 166 mW. 17 peaks are marked with the black vertical. The mode-spacing values for the peaks indicated with the red lines (presumably modes) are 0.90 nm and 0.94 nm.

Besides the discussed in Section 4.3.1 and the resolution of the optical spectrometer, the deviation between the calculated mode-spacing by theory and the measured may be due to the following:

- The imperfect spherical shape of the droplet.

- Except from the semi-spherical droplets, i.e. with contact angle 90°, the

94

stated droplet radii are not exactly, but only estimates. More accurate radii would be the virtual radii mentioned in Section 7.2.

Following the same procedure for measuring mode-spacing for the rest droplets, the obtained results are listed in Table 7.3. The emission spectrum with marked peaks and mode-spacing values for the rest of droplets is to find in Appendix D.

Surface type		R	$\Delta\lambda_{\text{theory}}$	$\Delta\lambda_{\text{measured}}$
Si-fluorocarbon	A	150 μm	0.84 nm	0.23-0.94 nm
Si-fluorocarbon	B	330 μm	0.38 nm	0.20-0.75 nm
BS	C	270 μm	0.58 nm	0.21-0.87 nm
BS-groove	D	330 μm	0.38 nm	0.19-0.74 nm
BS-groove	E	170 μm	-	-

Table 7.3: The calculated mode-spacing $\Delta\lambda_{theory}$ compared with the measured $\Delta\lambda_{measured}$ for three different droplet radii and two different surface types. Note that for droplet (E) with $R = 170$ μm no mode-spacing values are indicated, since no lasing was obtained for this droplet.

As it clearly emerges from Table 7.3 there are a wide variation on the measured mode-spacing values. However, the measured mode-spacing values are still in the order of the calculated.

7.4 Levitated Liquid Droplet Dye Laser

7.4.1 The Ultrasonic Levitator

The acoustic levitation is a technique that facilitates the performance of variety of investigations on small volumes of liquid samples, i.e. liquid droplets and particles. It suspends the object in a fixed point in fixed position (nodal points) of an ultrasonic standing wave without being in contact with any surface. The only contacting surface is the surrounding air. The technique was described in the 30'ies and requires no specific physical properties of the sample. The acoustic levitation technique is used in bio-analytical and analytical chemistry applications [57]. More specifically, the technique has been used to study properties of molten materials, the equilibrium shape and stability of liquid droplets and the mechanical properties of the biological materials [57].

The used acoustic levitator in this work operates in the ultrasonic frequency range, more specifically with a frequency of 58 kHz corresponding to a wavelength of about 6 mm. The ultrasonic wave is then reflected back and forth between the ultrasonic transducer and a solid reflector, Fig 7.28, which is adjusted concentrically at a distance of some multiple half wavelengths, resulting in a standing wave with equally spaced nodes, and antinodes of sound pressure (and velocity) will be generated. Since the maximal droplet diameter is a function of the ultrasonic wavelength, only samples with effective diameters of less than half a wavelength will be able to float or levitate. Droplets with diameters $d \geq 2/3\lambda$ can not be levitated. The optimal droplet diameter, for which minimal ultrasonic power is required is $d = \lambda/3$. If the levitated droplet exceeds the critical value of 1.5 of the Bond number, it disintegrates. And exceeding a droplet diameter of 2 mm, calculated by the Bond number in Section 2.2.4 the droplet begins deforming. The acoustic energy around the levitated droplet may also deform the droplet. With increasing sound intensity the drop will be spheroidally deformed.

Liquid sample is manually introduced from a μL-syringe and requires some experience. After the deployment of the EG droplet with the dissolved laser dye Rh6G, this was pumped by the external Nd:YAG laser (532 nm) by guiding the laser beam via a mirror horizontally into the levitated droplet, Fig 7.29. The emitted light from the micro-droplet dye laser was collected by the optical fiber placed at a position forming a lower angle of about 50°-60° with the direction of the external (Nd:YAG) laser beam. Since the droplet dye emission light actually was detected at this angle, this suggests that the dye droplet emits light in all directions around the droplet, at least around the droplet equator. According to the WGM model in Section 4.2, the light rays will undergo total internal reflection in a perfect EG sphere droplet, only if the angle of incidence is > 44°, which means that once the light is trapped within the droplet it intersects repeatedly with no light escape subsequently. However, real liquid droplets will never assume a perfect spherical form, why the droplet always will have edges that allows an amount light to be emitted.
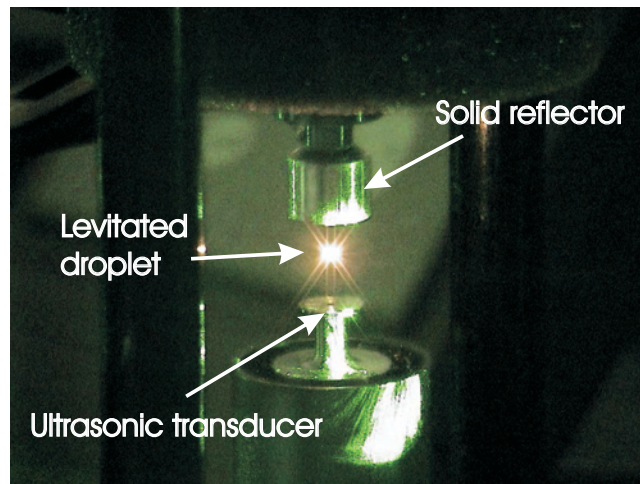
Figure 7.28: The ultrasonic levitator.
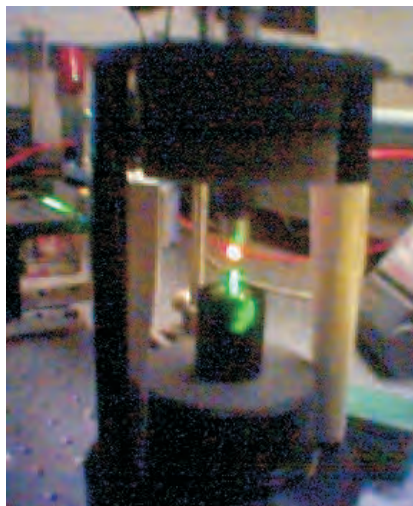
(a) Despite of the blurred picture, the lasing levitated droplet dye laser (fluorescent red spot) is clearly seen. The green light is the scattered pump laser light.
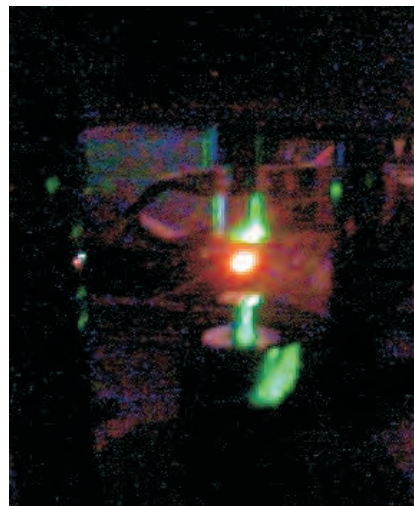
(b) A close-up view of the lasing levitated droplet dye laser.

Figure 7.29: The levitated droplet dye laser.

7.4.2 Lasing Measurements

Since the cooling of the levitated droplet was not possible during the measurements (pumping), it was appropriate and convenient to initiate the measurements by examining the behavior of the emission spectra of the droplet dye laser under the influence of evaporation during the pumping.

Thus, the measurements in this case were carried out by first measuring the emission spectra for increasing mean pump power P, and then for decreasing P for the same levitated droplet. Fig 7.30 shows the results obtained for an optically pumped EG droplet with the concentration $2 \cdot 10^{-2}$ mol/L of the dissolved laser dye Rh6G. The volume of the droplet was by an $\mu$L-syringe measured to about 1.5 μL. This corresponds to a droplet radius of $R \simeq 700$ μm. For increasing mean pump power, Fig 7.30(a), a distinct peak with approximately 7 nm FWHM is centered at 605 nm, at an optical pumping power of 15 mW. The emission spectra measured for decreasing mean pump power, Fig 7.30(b), carried out on the same droplet is displaced with approximately 13 nm towards higher wavelengths, more specifically centered at 618 nm. The distinct peak here has approximately the same FWHM, but a lower optical pumping power 7 mW. The measurement time for the increased and decreased mean pump power altogether is about 20 min. The displacement of the emission spectra may be due to the EG evaporation of the droplet and thereby leading to an increase of the concentration of the dye molecules within the droplet. This makes more Rh6G molecules available for excitations. Thus the laser obtains a lower threshold population inversion and thereby a red shifting of the lasing wavelength. And according to Peterson's discovery this indicates a reduction in the cavity losses. The reduction of the cavity losses as above-mentioned results in a red shifting of the laser light. The tuning of the output wavelength by changing the dye molecule concentration in the solvent is called *concentration tuning*. The evaporated droplet volume was by eye estimated to 30% of the origin droplet increasing the available excited dye molecules with same amount.

Another effect that is observed in both lasing spectra, i.e. for increased and decreased pumping, is the displacement of the single spectra relative to each other for the same measurement. The little displacement (about 2 nm) seems to be random. However, these may be a result of the evaporation process reducing the droplet volume and thereby making it more sensitive for the acoustic energy which again may lead to droplet deformation. This effect is observed for all the emission spectra.

Fig 7.31 shows the laser threshold for both increasing and decreasing pump power measurements of the same droplet. The efficiency curve for increasing mean pump power is quit convincing unlike the one for the decreased mean pump power. For the increasing pumping measurement, Fig 7.31(a) reveals the laser threshold of the system to be around 5 mW, and a linear rise of the output power. Although the measurement for decreasing pumping was not carried out for sufficient high mean pump power values as was done for the increased pumping measurement, the lack of a bend in Fig 7.31(b) may on the surface suggest that no lasing is occurring in the system, i.e. an initial droplet volume 1.5 μL decreased with about 30 %. However, measuring on a droplet with an initial volume approximatively corresponding to the leftover volume of the evaporated droplet, i.e. $70\% \Rightarrow 1\mu$L, and with the same dye concentration ($2 \cdot 10^{-2}$ mol/L), a more convincing efficiency curve is obtained for the system as shown in Fig 7.32(b). Although the red line in Fig 7.32(b) is not as steep as desired, however the efficiency curve reveals lasing characteristic of the 1 μL droplet, with threshold for lasing around 24 mW. That is about five times as high as the laser threshold (5 mW) for the droplet with initial volume 1.5 μL.
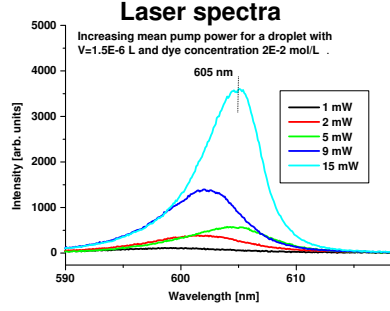
(a) The measured optical spectra for five increasing excitation powers emitted from the micro-cavity dye laser droplet. The laser emission spectra is centered at wavelength 605 nm.
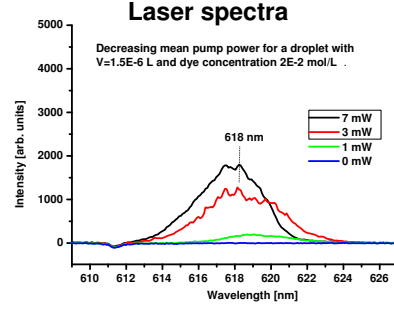
(b) The measured optical spectra for four decreased excitation powers emitted from the same micro-cavity dye laser droplet. The laser emission spectra is centered at 618 nm.

Figure 7.30: The measured optical spectra from a levitated micro-cavity droplet dye laser with volume 1.5 μL ($R \simeq 700$ μm) Rh6G dissolved in EG with a concentration of $2 \cdot 10^{-2}$ mol/L.
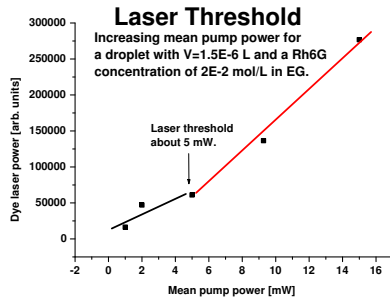
(a) The emitted power from the dye droplet determined as the output peak intensity of the dye laser emission spectra versus increased optical pump power. The threshold for lasing indicated by the bend occurs at an excitation power of 5 mW.

(b) The emitted power from the dye droplet determined as the output peak intensity of the dye laser emission spectra versus decreased optical pump power. Seemingly, no lasing occurs.

Figure 7.31: The emitted power from the dye droplet determined as the output peak intensity of the levitated droplet dye laser emission spectra versus both the increased and decreased optical pump power with initial volume 1.5 μL ($R \simeq 700$ μm).

(a) The measured optical spectra for six excitation powers emitted from the micro-cavity dye laser droplet. The laser emission spectra is centered at wavelength 616 nm.
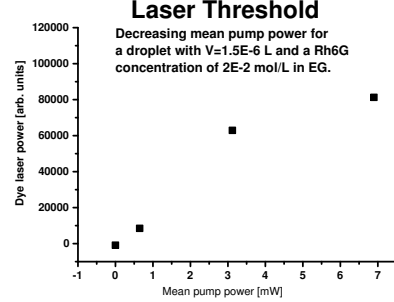
(b) The emitted power from the dye droplet determined as the output peak intensity of the dye laser emission spectra versus optical pump power. The threshold for lasing indicated by the bend at an excitation power of 24 mW.

Figure 7.32: Lasing spectra and laser threshold for a levitated micro-cavity droplet dye laser with volume 1 μL ($R \simeq 600$ μm) Rh6G dissolved in EG with a concentration of $2{\cdot}10^{-2}$ mol/L.

(a) The measured optical spectra for seven excitation powers emitted from the micro-cavity dye laser droplet. The laser emission spectra is centered at wavelength 608 nm.
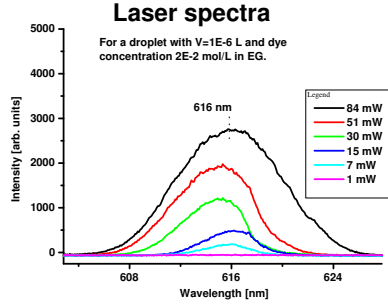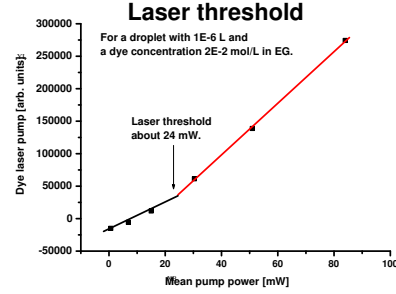
(b) The emitted power from the dye droplet determined as the output peak intensity of the dye laser emission spectra versus optical pump power. The threshold for lasing indicated by the bend at an excitation power of 36 mW. The marked points with blue seems to indicate that the Rh6G dye molecules are bleached by the high mean pumping powers 185 mW and 232 mW.

Figure 7.33: Lasing spectra and laser threshold for a levitated micro-cavity droplet dye laser with volume 1 μL ($R \simeq 600$ μm) Rh6G dissolved in EG with a concentration of $2{\cdot}10^{-6}$ mol/L.

The emission spectra in 7.32(a), is centered at 616 nm, at an optical pumping power of 84 mW above threshold. This matches the emission spectra measured for the evaporated droplet in Fig 7.30(b), where about 30 % of the droplet was estimated (by eye) evaporated, reducing the droplet volume to about 1 μL, confirming the assumption made about the red shifted displacement due to increased concentration of the dye molecules.

For a droplet with a 1000 times lower dye laser Rh6G concentration, namely $2 \cdot 10^{-6}$ mol/L, and the same volume, i.e. 1μL, the emission spectra in Fig 7.33(a) is observed to move towards shorter wavelengths, namely to 608 nm. Because of the low dye laser molecule concentration (1000 times lower), less molecules may be excited as explained resulting in an a "blue" shift of the wavelengths. However, Arbeola *et al.* [61] reports that the quantum yield of the dye molecules increases with decreasing concentrations in ethanol as a solvent. The effect is called fluorescence quenching, and is shown in Fig 7.34. Assuming a similarity between ethanol and EG, this effect has to be taken into account.

More specifically, a dye concentration $2 \cdot 10^{-2}$ mol/L corresponds to a quantum yield $\phi = 45$ % as shown in Fig 7.34. Already at concentration $6 \cdot 10^{-3}$ mol/L, ϕ saturates and keeps being constant for low concentrations why we assume that for the dye concentration $2 \cdot 10^{-6}$ mol/L, ϕ is 85 %. By using a concentration 1000 times lower, we lower the dye molecules available for excitation 1000 times. The fluorescence quantum yield for this concentration is only increased by factor about 2 which is much less factor 1000. This means that a 1000 times decrease of the dye molecule concentration, the quantum yield is in no way capable to match the decreased number of available Rh6G molecules. Thus the laser obtains a higher threshold population inversion and a strongly displacement of the emission spectra towards shorter wavelength. This also explains the relatively high obtained laser threshold value 36 mW shown in Fig 7.33(b).
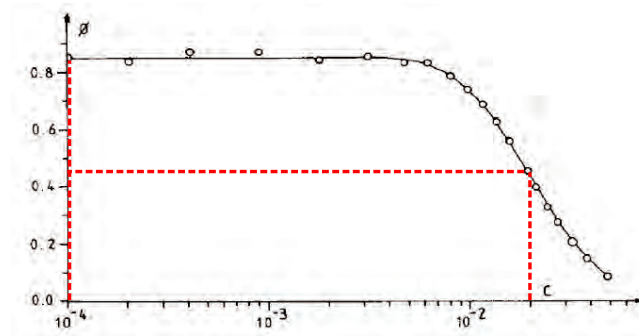
Figure 7.34: Fluorescence quantum yield of Rh6G in ethanol at different concentrations (mol/L) at 20°C [61].

For the same dye laser concentration ($2 \cdot 10^{-6}$ mol/L) and a four times bigger droplet, i.e. volume of 4 μL $\Rightarrow R =$1200 μm , the emission spectra is positioned at nearly the same wavelength, namely 605 nm. Although there is a little displacement, i.e. about 3 nm, compared to the previous emission spectra, this may be due to statistical random. The laser threshold occurs however as

expected at a lower value, namely at 12 mW. This is shown in Fig 7.35. The discussed results are listed above in Table 7.5.
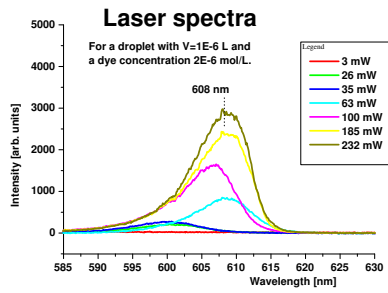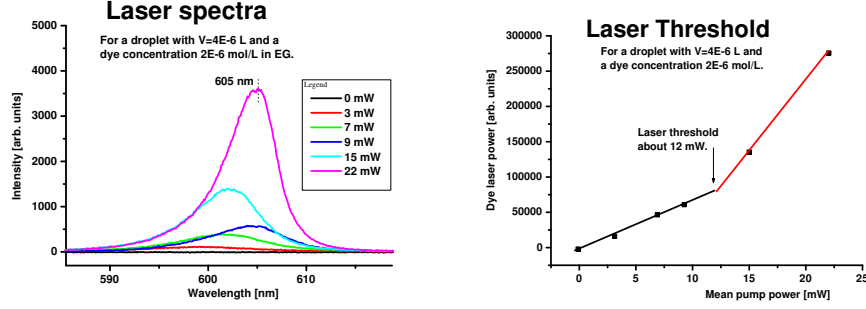

(a) The measured optical spectra for six excitation powers emitted from the micro-cavity dye laser droplet. The laser emission spectra is centered at wavelength 605 nm.
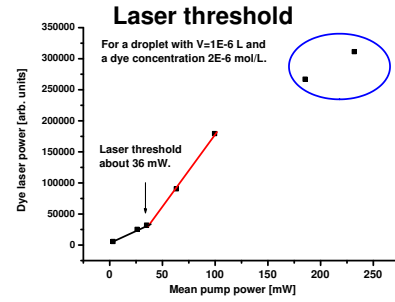
(b) The emitted power from the dye droplet determined as the output peak intensity of the dye laser emission spectra versus optical pump power. The threshold for lasing indicated by the bend at an excitation power of 12 mW.

Figure 7.35: Lasing spectra and laser threshold for a levitated micro-cavity droplet dye laser with volume 4 μL ($R \simeq 1200$ μm) Rh6G dissolved in EG with a concentration of $2 \cdot 10^{-6}$ mol/L.

V	Rh6G concentrations in EG	Emission maximum	Laser threshold
1 μL	$2 \cdot 10^{-2}$ mol/L	614-616 nm	24 mW
1 μL	$2 \cdot 10^{-6}$ mol/L	607-608 nm	36 mW
$1^{\dagger}$ μL	$2 \cdot 10^{-2}$ mol/L	618-619 nm	-
1.5 μL	$2 \cdot 10^{-2}$ mol/L	602-605 nm	5 mW
4 μL	$2 \cdot 10^{-6}$ mol/L	603-605 nm	12 mW

Table 7.4: The obtained results for three different laser dye droplet radii and two different dye concentrations. The measured mode-spacing are average values. The droplet volume indicated with † is the estimated volume for the droplet after evaporation (30 % evaporated of the origin droplet with initial volume 1.5 μL) with laser spectra shown in Fig 7.30(b) for decreased pumping.

7.4.3 Mode-spacing

As regards the mode-spacing, a close-up view of the emission spectra for the droplet with volume 1 μL and dye laser concentration $2 \cdot 10^{-6}$ mol/L can for instance be considered for a mean pump power 100 mW. This is shown in Fig 7.36. The same reservations are valid as those mentioned in Section 7.3.4 when measuring the mode-spacing between the noticeable peaks on the emission spectra. Nevertheless, the distance between 12 visible peaks marked in Fig 7.36 is in the interval of 0.18-0.35 nm, which is still in the order is of the calculated mode-spacings. However, besides the resolution of the spectrometer

the deviation between the predicted and the measured value may be due to the following:

- The uncertainty of the droplet volume associated with the manual droplet deployment. I have estimated the uncertainty of the droplet volume to be about 0.1 μL corresponding to a radius change of about 300 μm. The influence of such radius change on mode-spacing is a changes of about 0.1 nm.

- Despite the little droplet radius (or volume), which in most cases fulfils the condition of the Bond number, the frequency generator requiring a fine adjusting still may deform the droplet.

- The droplet evaporation during the pumping process reduces droplet volume, i.e. droplet radius, and thereby increasing the mode-spacing.

Following the same procedure as above mentioned, the mode-spacing for the rest of the measurements carried out on various levitated droplets is determined and listed in Table 7.5. The emission spectrum with marked peaks and mode-spacing values for the rest of droplets is to find in Appendix E.
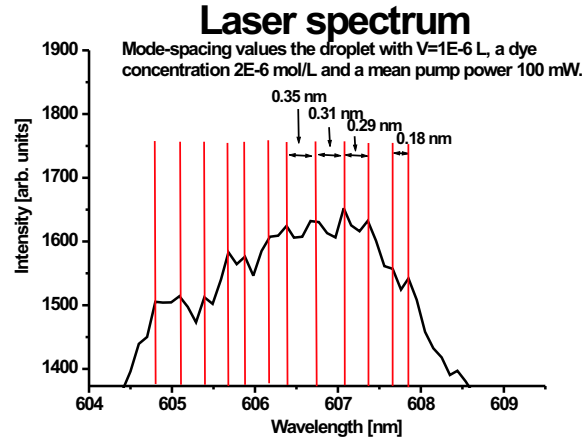

Figure 7.36: A close-up of the emission spectrum shown in Fig 7.33(a) in order to measure the mode-spacing for the mean pump power 15 mW. 12 peaks marked with the red vertical lines, with varying mode-spacing values: 0.35 nm, 0.31 nm, 0.29 nm and 0.18 nm.

Droplet volume V	Rh6G concentration in EG	$\Delta\lambda_{theory}$	$\Delta\lambda_{measured}$
1 μL	$2 \cdot 10^{-2}$ mol/L	0.24 nm	0.20-0.59 nm
1 μL	$2 \cdot 10^{-6}$ mol/L	0.24 nm	0.18-0.35 nm
1.5 μL	$2 \cdot 10^{-2}$ mol/L	0.19 nm	0.19-0.60 nm
4 μL	$2 \cdot 10^{-6}$ mol/L	0.12 nm	-

Table 7.5: The calculated mode-spacing $\Delta\lambda_{theory}$ compared with the measured $\Delta\lambda_{measured}$ for two different droplet radii and two different dye concentrations. The calculated mode-spacing for the droplet with volume 4 μL lies below the resolution of the spectrometer, why this could not be measured.

The calculated mode-spacing for a droplet volume 4 μl ($R \simeq 1200$ μm) is 0.12 nm. Since the spectrometer resolution is 0.15 nm, this could unfortunately not be measured. Although the measured mode-spacing values does not reflect the fact of decreasing mode-spacing for increasing droplet volumes, i.e droplet radius, as discussed in Sec 4.3, however it emerges clearly that the measured mode-spacings is in the order of the calculated mode-spacing values.

For instance, desiring a mode-spacing of about 3-4 nm (corresponding to about 2 modes within a 7 nm broad gain) at an emission maximum 580 nm, the droplet radius has to be reduced to about 30-40 μm according to eq. (4.38); i.e. droplet volumes of 0.1-0.3 nL. An advanced setup of the levitator system is actually able to produce droplets with radius in the order of 30 μm. And with a cooling system installed in the levitator system, the droplet might be prevented from evaporating while pumping.

7.5   Summary

To summarize the obtained results and point out the observed physical properties and connections, we first consider the droplets lying on the various surface types. For this the following common characteristics were observed:

- For decreasing droplet (gain-cell) dimension, the threshold value increased. A small gain requires high laser pumping power in order to overcome the cavity losses, and thus a high laser threshold is obtained.

- A doubling of the droplet dimension from 150 μm to 330 μm, resulted in a 5-6 nm displacement of the lasing wavelengths towards shorter wavelength. This was explained with the long path alight ray has travel resulting in a higher absorption rate and thus an increase in the cavity losses.

- For relatively small droplets ($R = 170\mu$m) placed on a BS surface, no lasing occurred. This was interpreted by the BS surface that may absorb an amount of light and thereby lead to an increase of cavity losses which the gain can not overcome and the lasing fail to occur.

- The light emitted from the dye droplet is observed to travel around the utmost circumference of the droplet in agreement with the resonator model. However, the light was not emitted in all directions and did not occur around the whole droplet in contrast to theory.

As regards the levitated droplet, the following was observed:

- Besides the dependency between the laser threshold and the gain dimension, another dependency is observed, namely between laser threshold and dye concentration. For increasing concentrations the threshold decreases.

- The dependency of the emission spectra on the dye concentration was also demonstrated by the so-called concentration tuning, where the increase of the dye concentration results in a red shift of the emission spectra.

- The whole droplet was observed to be radiant, indicating that the liquid-air interface of the levitated droplet is reflecting the light around the whole droplet. The emitted light from the dye droplet was also detected from different angles around the droplet. These observations indicate the liquid-air interface of the droplet is functioning as a resonator similar to the WGM resonator model.

The mode-spacing dependency on the droplet dimension for both droplet types, i.e. surface and levitated droplets, was theoretically demonstrated, where the increase of the droplet dimension decreases the mode-spacing. However, this was not observed experimentally due to the mentioned reasons in the previous two sections. However, the measured mode-spacing values are still in the order of the calculated values, which again indicate that the droplet is a spherical cavity as predicted.

Chapter 8

Conclusion

The liquid micro-droplet dye laser with self-organized spherical cavities have been investigated and described in this thesis. The primary target is to demonstrate lasing in liquid droplet dye laser and to get an overview of the theory describing the resonant modes. The minor target is to optimize the contact angle of the liquid droplet by fabricating ethylene-glycol-phobic surfaces. All the targets are basically reached.

Requiring a hemispherical shape of the droplet, the Bond number estimated the droplet radius to be < 1 mm. This estimate was confirmed by droplet simulations carried out in the simulation program: Evolver, and most important by the droplet shape experiments. The dimension of the created droplets lying on surfaces were in the micron range; from 150 μm to 330 μm. These were deposited by a dip pen method.

Compared to a silicon surface, with rms roughness of 10-30 μm, with a contact angle of $40°$ for an EG droplet, the contact angle was optimized to about $77°$ by C_4F_8 gas phase deposition of a fluorocarbon film on these silicon surfaces. However, a relatively high ethylene-glycol-phobic surface was obtained by fabricating a Black Silicon (BS) surface deposited with a fluorocarbon film. The BS surface with a roughness of about 300 nm was fabricated by anisotropic Reactive Ion Etch based on SF_6 and O_2. The BS surfaces yielded the optimal contact angle for EG droplets among the tested surfaces. The contact angle on BS was optimized to about $90° - 100°$. The fluorocarbon-deposited BS surface may nearly be characterized as super-hydrophobic, since the contact angle for a water droplet on this was measured to $145°$. To prevent the liquid droplet dye laser from the inexplicable deformation during pumping, the so-called BS-groove surface was fabricated. The width of the grooves is 25 μm and the distance between them is 100 μm. These patterned BS surfaces were fabricated by utilizing the Nanoimprint Lithography (NIL) technique. Although the BS-groove surface did prevent a big part of deformations, it could not completely prevent the occurrence of these.

In the resonator model a shielded and isotropic spherical dielectric resonator was taken as a starting point. The resonant behavior of the Whispering Gallery Mode (WGM) in such a resonator was to begin with in the simple heuristic picture viewed as a single ray (mode) that once trapped near the surface of the spherical cavity undergos total internal reflection. And since we in our case work with an EG droplet with refractive index 1.43, the trapped ray could only

undergo total internal reflection if the angle of incidence is $> 44°$. Here after, we advanced further in developing a model, which not only views a single mode, but all the modes that identifies an individual WGM. These are (l, m, n) representing together the radial, equatorial and polar electromagnetic components. The modes were demonstrated to be solutions to Maxwell's equations, and an expression for the mode-spacing considering all the modes, was subsequently derived. The similarities between the shielded homogeneous isotropic dielectric sphere and our actual liquid droplet was discussed.

A visualization of the WGMs within a sphere was tried carried out via the simulation program FEMLAB. The simulation of the WGMs in the range of our droplet dimensions; i.e 150-600 μm, failed due to limitations in the simulation program. However, we did get an impression of the WGMs as an effect occurring at the edge of the sphere for sphere dimensions much less than ours, namely those with radii 2 μ nm and 600 nm.

However, it should be pointed out that the resonator model does not considerate the resonant behavior for a droplet placed on a substrate. We assumed that light in this case still will travel along the droplet circumference. However, one could imagine that a resonator occurs between the substrate and the top of the droplet surface, and thus leading to a vertically light reflection back and forth, instead of a light travelling along the circumference of the droplet. A further development of the model should take this under consideration.

The liquid droplet dye laser has been characterized using the laser dye Rhodamine 6G (Rh6G) dissolved in ethylene glycol (EG) as the active gain medium. The liquid droplet was optically pumped vertically at 532 nm by an external frequency doubled Nd:YAG laser. The evaporation rate of the droplet was measured to 2.2 nL/min, limiting the measurement time to few minutes. Evaporation of the droplet was minimized if not prevented by cooling it with a peltier-element to about 11°C. Deposited on three different surfaces: rough silicon, BS and BS-groove, multi-mode lasing was observed on liquid spherical droplet dye laser. However, due to the limitation in the spectrometer resolution and the appearing noise on the emission spectra, one could not rely on the measured mode-spacing values, why these could not be compared to the calculated mode-spacing values. Nevertheless, the measured values were in the order of the calculated. The laser threshold was observed to increase with decreasing droplet dimension. This was explained by that a less gain-cell requires a higher pumping power in order for the cavity system to equalize the losses; thus a higher laser threshold value. The dye laser light was observed to circulate around the circumference of the droplet, indicating the WGM resonances to occur in the droplet, as predicted by the model. The WGM model assumes the liquid droplet dye laser to emit light around the whole droplet. This is not observed for the liquid droplet dye laser lying on a substrate, since dye laser light is only detected vertically (above the droplet) and not around it.

The levitated liquid droplet dye laser was successfully characterized also by means of Rh6G dissolved in EG and was optically pumped horizontally by a pulsed frequency doubled Nd:YAG laser at 532 nm. The dimension of the created levitated liquid droplet ranged from about 600 μm to about 1200 μm. Also here, the measured mode-spacing values were in the order of the calculated. The levitated liquid droplet dye laser was observed to emit laser light around the droplet. This suggests a WGM resonance occurring within the droplet in agreement with the theory. The fact that the levitated spherical droplet is not

in contact with any surface, makes it the resonator that nearly matches the ideal resonator treated in the model. For a spherical droplet with volume 1 μL, the change of the dye concentration resulted in a laser spectra shift to about 7 nm, between 607 nm and 614 nm. The shifts was explained by the change in the threshold population inversion leading to a change in laser wavelength as discovered in 1971. A four doubling of the EG droplet volume did not result in a significant shift of the laser spectra. The shift was measured to about 3 nm, and could as well be due to statistical randoms.

Future experiments can be improved, especially by being able to measure the droplet dye output power. This could be done by utilizing a low-energy-power meter.

The major problem when measuring on the levitated droplet is the rapid evaporation rate. However, a more sophisticated levitator setup is actually able to cool the droplet down to 0°C [57]. This will presumably prevent the droplet from evaporating. Ensuring such a levitator setup system, following experiments on the liquid droplet dye laser are suggested :

- Decrease the droplet radius to about 30-40 μm in order to get a mode-spacing to 3-4 nm and thereby reduce the number of the modes to one or few modes in the about 7 nm broad gain window. The above mentioned sophisticated levitator setup has an integrated droplet shooter system able to create droplets with dimensions in the order of 30 μm.

- The tunability of the dye laser can be investigated by experimenting with different dyes besides Rh6G such as : Rhodamine 110 and Fluorescein.

- With the cooled liquid droplet, more accurate and systematic concentration tuning measurements can be performed.

- The tunability of the liquid droplet dye laser can also be investigated by changing the refractive index [35], i.e. changing solvents. Such a cooling system may prevent an ethanol droplet from evaporating.

- The dependency of laser spectra on various droplet shapes; i.e deformation of droplets, can be investigated.

Laser dye functionalised levitated droplets may add a new range of possibilities for droplet manipulating systems, both with regards to sensor applications and laser physics in the self-organized spherical cavities. The dream would be to create a levitated liquid micro-droplet dye laser with the ability to lase in the whole optical spectrum by continuously shooting micro-droplets in the node points created in the levitator system, where the droplet shape and dimension, dye concentration, dye- and solvent type is controlled (or changed).

Bibliography

[1] F. Treussart, V. S. Ilchenko, J. F. Roch, P. Domokos, J. Hare, V. Lefévre, J.-M. Raimond, S. Haroche : *Whispering gallery mode microlaser at liquid Helium temperature*, Journal of Luminescence, 76 and 77, pp. 670-673, 1998.

[2] Vladimir S. Ilchenko, Anatoliy A. Savchenkov, Andrey B. Matsko, and Lute Maleki: *Dispersion Compensation in Whispering-gallery Modes*, Optical Society of America, Vol. 20, No. 1, January, 2003.

[3] F. P. Scäfer, B. B. Snavely, C. V. Shank, E. P. Ippen, K. H. Drexhage, and T. W. Hänsch: *Topics in Applied Physics, Dye Lasers*, Volume 1, Springer-Verlag Berlin, Heidelberg, New York, 1973.

[4] B. Helbo: *Investigation of The Dye Concentration Influence on The Lasing Wavelength and Threshold for A Micro-fluidic dye laser*, preprint, 2003.

[5] H. Yokoyama, M. Suzuki, and Y. Nambu: *Spontaneous emission and laser oscillation properties of microcavities containing a dye solution*, Appl. Phys. Lett. 58 (23), 10 june, 1991.

[6] J. Klebniczki, J. Hebling, B. Hopp, G. Hajós, and Z. Bor: *Fluid jet with variable thickness in the range 5-20 μm*, Meas. SCi. Technol., Vol. 5, pp. 601-603, 1994.

[7] Sung Kwon Cho, Shih-Kang Fan, Hyejin Moon, and Chang-Jing "CJ" Kim: *Towards Digital Microfluidic Circuits: Creating, Transporting, Cutting and Merging Liquid Droplets by Electrowetting-based Actuation*, Proc. of the IEEE 15th International Conference on Micro Electro Mechanical Systems, MEMS 2002, Las Vegas, USA, 2002, pp. 32-35.

[8] Proffesor Staffan Nilsson,
Department of Technical Analytical Chemistry,
Lund Institute of Technology,
Lund University.
staffan.nilsson@teknlk.lth.se

[9] Arthur W. Adamson: *Physical Chemistry of Surfaces*, Physical Chemistry of Surfaces, Fifth Edition, John Wiley and Sons, Inc., Los Angeles, California, 1990.

[10] J.J.bikerman: *pPhysical Surfaces*, Academic Press, New York and London 1970.

[11] Keith J. Laidler and John H. Meiser: *Physical Chemistry*, Third Edition, Houghton Mifflin Company, Boston, New York.

[12] Mads Jakob Jensen: *Bubbles in Microchannels*, Master thesis, Department of Micro and Nanotechnology (MIC), Technical University of Denmark, 2002.

[13] Joseph H. Noggle: *Physical Chemistry*, Third Edition, HarperCollinsCollegePublishers.

[14] Gordon M. Barrow: *Physical Chemistry*, Third Edition, McGraw-Hill Book Company.

[15] Gilbert W. Castellan: *Physical Chemistry*, Second Edition, Addison-Wesley Publishing Company.

[16] S. S. Dukhin, G. Kretzschmar and R. Miller: *Dynamics of Adsorption at Liquid Interfaces*, Vol. I, series Editors: D. Mobius and R. Miller, 1995 Elsevier.

[17] Egon Matijevic: *Surface and Colloid science*, Vol. 2, Wiley-interscience, 1969.

[18] Norman H. March and Joseph F. Mucci: *Chemical Physics of free Molecules*, Plenum Press, New York, 1993.

[19] P. W. Atkins: *Physical Chemistry*, Fourth edition, Oxford University Press, 1990.

[20] *Handbook of Chemistry and Physics*, 67Th Edition, CRC Press, 1986-1987.

[21] *Medicinsk Biofysik 1.Grundbog*, AArhus Universitetsforlag, 1997.

[22] G. McHale, N. J. Shirtcliffe and M. I. Newton: *Super-hydrophobic and super-wetting surfaces: Analytical potential?*, The Royal Society of Chemistry, Analyst, 129, February 2004.

[23] J. Bico, C. Marzolin and D. Quére: *Pearl Drops*, Europhysics Letters, Eurpphys. Lett., 47(2), pp. 220-226, 15 July 1999.

[24] Mathilde Callies, Anne Pépin, Yong Chen, and David Quéré: *Microfabricated textured surfaces for super-hydrophobicity investigations*, Laboratoire de Physique de la Matiére Condensée, Collége de France, 11 place Marcelin Berthelot, 75231 Paris Cedex 05, France.

[25] S. C. S. Lai: *Mimicking nature: physical basis and artificial synthesis of the Lotus-effect*, Universiteit Leiden, August 2003.

[26] *www.botanik.unibonn.de/system/lotus/en/prinzip_html.html*.

[27] Frank L. Pedrotti and Leno S. Pedrotti: *Introduction to Optics*, Second Edtion, Prentice Hall International Editions, 1996.

[28] Jeff Hecht: *The Laser Guidebook*, Second Edition, Tab Books, 1992.

[29] J. Wilson and J.F.B Hawkes: *Lasers, Principles and Applications*, First Edition, Prentence Hall International (UK) Ltd, 1987.

[30] Michael Bass, Eric W. Van Stryland, David R. Williams, and William L. Wolfe: *Handbook of Optics, Fundamentals, Techniques, & Design*, Second Edition, Volume I, McGraw-Hill, Inc., 1995.

[31] Peter W. Milonni and Joseph H. Eberly: *Lasers*, Willey-Interscience Publication, USA, 1988.

[32] A. Mattland and M. H. Dunn: *Laser Physics*, Noth-Holland Publishing Company, Amterdam-London, 1969.

[33] Douglas Magde, Roger Wong and Paul G. Seybold: *Fluorescence Quantum Yields and Their relation to Lifetimes of Rhodamine 6G and Fluorescein in Nine Solvents: Improved Absolute Standards for Quantum Yields*, Photochemistry and Photobiology, 75(4), 327-334, 2002.

[34] *www.exciton.com*

[35] Morten Gersborg-Hansen: *A coupled Cavity Micro Dye Ring Laser*, Master thesis, Copenhagen, 2004.

[36] Shaozhong Deng, Wei Cai: *Numerical Modeling of Optical Coupling by Whispering Gallery Modes between Microcylinders*, Departement of Mathematics, University of North Carolina at Charlotte, January 9, 2004.

[37] S. L. McCall, A. F. J. Levi, R. E. Slusher, S. J. Pearton, and R. A. Logan: *Whispering-gallery mode microdisk lasers*, Appl. Phys. Lett. 60(3), 20 January 1992.

[38] R A YADAV and I D SINGH: *Normal modes and quality factors of spherical dielectric resonators: I-Shielded dielectric sphere*, Pramana -journal of physics Vol. 62, No.6 June 2004, pp. 1255-1271.

[39] John D. Joannopoulos, Robert D. Meade, Joshua N. Winn.: *Photonic Crystals, Molding the flow of light*,

[40] Juha-Pekka Laine: *Design and Applications of Optical Microsphere Resonators*, Helsini University of Technology, Materials Physics, 2003.

[41] Rachel Symes, Robert M. Sayer and Jonathan P. Reid: *Cavity enhanced droplet spectroscopy: Principles, perspectives and prospects*, Phys. Chem., (6), pp. 474-487, 2004.

[42] Emily Shuk Chi Ching, Pui Tang Leung, and Kenneth Young: *Optical Processes in Microcavities - The Role of Quasinormal Modes*, Department of Physics, The Chineese University of Hong Kong, Hong Kong.

[43] A.A. Ayón, D.-Z Chen, R. Khanna, R. Braff, H. H. Sawin and M. A. Schmidt: *A novel Integrated MEMS Process Using Fluorocarbon Films Deposited with a Deep Reactive Ion Etching (DRIE) Tool*, Mat. Res. Soc. Symp. Proc. Vol.605, 2000, pp. 141-147.

[44] Dr. David Mecerreyes,
New Materials Department,
CIDETEC-CENTRO de Tecnologías Electroquímicas,
San Sebastian, Spain.
dmecerreyes@cidetec.es

[45] *www.honeywell.com.*

[46] Daniel A. Maidenberg, Willi Volksen, Robert D. Miller and Reinhold H. Dauskradt: *Toughening of nanoporous glasses using porogen residuals*, Nature materials, Vol.3, July 2004, pp. 464-469.

[47] F. Zhang, O. Leonte, Z. J. Chen, L. Jin, J. A. Camarena, B. Daniels, J. Dunne, T. Nguyen, T. A. Ramos, S. Thanawala: *Nanoglass^{TM} E Copper Damascene Processing for Etch, Clean, and CMP* 2004.

[48] Kenneth K. S. Lau, José Bico, Kenneth B. K. Teo, Manish Chhowalla, Gehan A. J. Amaratunga, William I.Milne, Gareth H. McKinley, and Karen K. Gleason: *Superhydrophobic Carbon Nanotube Forests*, Nano Letters, Vol.3, No.12, 2003, pp.1701-1705.

[49] Michael Stenbæk Schmidt: *Anistropic reactive ion etching of carbon nanotube structured stamps for nanoimprint lithography*, M. Sc. Thesis, Department of Micro and nanotechnology, DTU, September 2004.

[50] Søren Dahl Petersen and Anders Thaulow: *Black Silicon Nanostructures*, Midterm Project, Department of Micro and nanotechnology, DTU, June 25, 2004.

[51] James D. Plummer, Michael D. Deal and Peter B. Griffin: *Silicon VLSI Technology, Fundamentals, Practice and Modeling*, Prentice Hall, New Jersey, USA, 2000.

[52] T. Nielsen, R. H. Pedersen, O. Hansen, J. Ahepelto and A. kristensen: *Flexible stamp for homogeneous large area thermal nanoimprint lithography*, MIC-Department of Micro and Nanotechnology, Technical University of Denmark (DTU), Journal of Vacuum Science and Technology B, October 7, 2004.

[53] *http://mse.iastate.edu/microscopy/home.html*

[54] TOPS-PIN Aps, Oersteds Plads build, 345 east, DK-2800 Lyngby: *www.topspin.dk*, Contact: Karen Birkelund.

[55] *www.oceanoptics.com*

[56] Murray R. Spiegel: *Mathematical Handbook of Formulas and Tables*, Schaum's outline series, McGraw-Hill, 36th Printing, 1997, USA.

[57] Sabina Santesson: *Miniaturised Bioanalytical Chemistry in Acoustically Levitated Droplets*, Ph.D Thesis, Department of Technical Analytical Chemistry, Lund University of Technology, Lund University, Sweden, 2004.

[58] Johan Nilsson, Thomas Laurell, Lars Wallman and Johan Drott: *A Flow-Through Liquid Picoliter Sampling Cell*, Proceedings μTAS'96, Nov. 19-22, Bassel, Schweitz.

[59] Compound Microdispensing: *Johan Nilsson, Jonas Bergkvist, Simon Ekström, Lars Wallman and Thomas Laurell*, Department of Electrical Measurements, Lund Institute of Technology, Lund, Sweden.

[60] O. G. Peterson, J. P. Weeb, W. C. McColgin, and J. H. Eberly: *Organic Dye Laser Threshold*, J. Appl. Phys., 42(5):1917-1982, 1971.

[61] F. López Arbeola and P. Ruiz Ojeda: *The Fluorescence Quenching mechanisms of Rhodamine 6G in Concentrated Ethanolic Solution*, journal of Photochemistry and Photobiology, A:Chemisrty, 45 (313-323), 1998.

[62] B. Shapiro, H. Moon, R. Garrel, Chang-Jin "CJ" Kim: *Equilibrium Behaviour of Sessile Drops under Surface tension, Applied External Fields, and material Variations*, Journal of Applied Physics, December, 2002.

[63] Lee W. Casperson: *Electromagnetic modes of an inhomogeneous sphere*, Applied Optics, Vol. 20, No. 15. 1 August, 1981.

[64] Günter Roll and Gustav Schweiger: *Geometrical Optics Model of Mie resonances*, J. Opt. Soc. Am. A, Vol. 17, No. 7, July, 2002.

Appendix A

A Conversion from an Energy Minimum to the Modified Young's Equation

Based on [62], we introduce an analysis based on an energy minimization framework to derive the *Young's equation*. The derivative of the energy is given by eq.(2.25). The volume of the droplet is is given by [62]

$$v(R, \theta) = \pi R^3 \left(\frac{2}{3} - \frac{3 \cos \theta}{4} + \frac{\cos 3\theta}{12} \right) \tag{A.1}$$

Since the volume of the droplet is assumed constant, the derivative of it must be zero. Thus

$$dv = \left[\frac{\partial v}{\partial R}(R, \theta) \right] dR + \left[\frac{\partial v}{\partial \theta}(R, \theta) \right] d\theta = 0. \tag{A.2}$$

Solving eq. (A.2) for dR in terms of $d\theta$ we get

$$dR = Rq(\theta)d\theta = R\left(-\frac{2cos^2(\theta/2)\cot(\theta/2)}{2 + \cos \theta} \right) d\theta. \tag{A.3}$$

Substituting eq. (A.3) in eq. (2.25) yields the energy change with respect to the contact angle:

$$\frac{dE}{d\theta} = \left[\frac{\partial E}{\partial R}(R, \theta) + \right] Rq(\theta) + \left[\frac{\partial E}{\partial \theta}(R, \theta) + \right] = 0, \tag{A.4}$$

where $q(\theta)$ is defined as

$$q(\theta) = -\frac{[2 \cos^2(\frac{\theta}{2}) \cot(\frac{\theta}{2})]}{[2 + \cos \theta]}. \tag{A.5}$$

In order to get the Young term $\gamma_{lg} \cos \theta$ to appear in eq. (A.4) we multiply by $-(2 + \cos \theta)/2\pi R^2 sin\theta$, and we get eq. (2.26).

If we assume the surface tension coefficients constant, the interface potential energy of the droplet is given by

$$E_{int} = (\gamma_{ls} - \gamma_{gs})A_{ls} + \gamma_{lg}A_{lg}, \tag{A.6}$$

where A_{ij} is the interface area. From geometrical reasoning we get

$$A_{ls}(R, \theta) = \pi R^2 sin^2\theta \tag{A.7}$$
$$A_{lg}(R, \theta) = 2\pi R^2(1 - \cos\theta) \tag{A.8}$$

Thus we get for the interfacial potential energy

$$E_{int}(R, \theta) = R^2[(\gamma_{ls} - \gamma_{gs})\pi \sin^2\theta + \gamma_{lg}2\pi(1 - \cos\theta)]. \tag{A.9}$$

Solving eq. (A.9) we get Young's equation: $\gamma_{lg}cos\theta - (\gamma_{gs} - \gamma_{ls}) = 0$.

Appendix B

A Comparison between The WGMs in A Sphere and A Quantum Particle in Spherical Quantum Dsot

It is quit convenient and suitable for the strengthen of the intuitive understanding to carry out a comparison between two physical phenomenon in order to identify the similarities between the two. In our case it is the WGMs and a photon circulating.

We can start by considering the ray in Fig 4.1(b) as a photon. Its momentum would be

$$p = \hbar k = \hbar \frac{2\pi}{\lambda/n_{\text{ref}}} \tag{B.1}$$

where k is the wave number. If it hits the surface at near-glancing incidence ($\theta_{\text{in}} = \pi/2$), the angular momentum, denoted as $\hbar l$, is

$$\hbar l = pR = \frac{2R\pi\hbar}{\lambda/n_{\text{ref}}} \tag{B.2}$$

which is exactly eq. (4.3). The point of this derivation is to identify the integer n, originally introduced as the number of wavelengths in the circumference, as the angular momentum in the usual sense.

The photon propagates in a circle, which may be inclined at an angle α with respect to the equator ($x - y$ plane); e.i. α is the angle between the normal to the circle and the z axis as shown in Fig B.1. The z component of angular momentum is then

$$m = l\cos\alpha \tag{B.3}$$

Furthermore, there is also the radial component of the photon momentum also called, the radial quantum number ν.
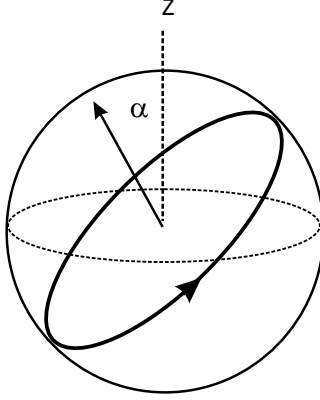
Figure B.1: Photon path is a great circle.

B.1 Alternative solution to the TE mode

Alternatively, the solution to the TE mode could be carried out by introducing the angular momentum operator $\mathbf{L}$ defined as, $L = (1/j)(\mathbf{r} \times \nabla)$, where $j = \sqrt{-1}$, and constructing L^2 and its relationship with the Laplacian operator. This procedure can be identified with the following derivation considering a quantum particle in a sphere with energy spectrum governed by the one-particle Schrödinger equation given by

$$-\nabla^2 \psi(\mathbf{r}) = \xi \psi(\mathbf{r}) \tag{B.4}$$

with a boundary condition

$$\psi(\mathbf{r})|_{r=0} = 0 \tag{B.5}$$

corresponding to particle confinement to a sphere of radius a. In spherical coordinates we have

$$-\frac{1}{r^2}\left[\frac{\partial}{\partial r}\left(r^2 \frac{\partial \psi}{\partial r} \right) + \frac{1}{\sin\theta}\frac{\partial}{\partial\theta}\left(\sin\theta \frac{\partial \psi}{\partial\theta} \right) + \frac{1}{\sin^2\theta}\frac{\partial^2 \psi}{\partial\phi^2} \right] = \xi\psi \tag{B.6}$$

The solutions are spherical harmonics,

$$\psi_{nlm}(\mathbf{r}) = R_{nl}(r)Y_{lm}(\theta,\phi) \tag{B.7}$$

and since $\mathbf{L}^2 Y_{lm} = l(l+1)Y_{lm}$ we get

$$
\begin{aligned}
0 &= -\frac{1}{r^2}\frac{\partial}{\partial r}\left(r^2 \frac{\partial R_{nl}}{\partial r} \right) + \left(\frac{l(l+1)}{r^2} - \xi \right)R_{nl}, & \text{(B.8)} \\
&= -\frac{1}{r^2}\frac{\partial}{\partial r}(rR_{nl}) + \left(\frac{l(l+1)}{r^2} - \xi \right)R_{nl}, & \text{(B.9)} \\
&= -\left(\frac{\partial}{\partial r} + \frac{2}{r}\frac{\partial}{\partial r} \right)R_{nl} + \left(\frac{l(l+1)}{r^2} - \xi \right)R_{nl}. & \text{(B.10)}
\end{aligned}
$$

117

The general solution is

$$R_{nl}(r) = \alpha r^{-1/2} J_{l+1/2}(\kappa_{nl} r) + \beta r^{-1/2} Y_{l+1/2}(\kappa_{nl} r) \tag{B.11}$$

where $\xi_{nl} = \kappa_{nl}^2$ with a degenracy $2l + 1$. Since the last term diverges when $r \to 0$ we have $\beta = 0$. From the boundary condition $R_{nl}(a) = 0$ we get

$$J_{l+1/2}(\kappa_{nl} a) = 0, \tag{B.12}$$

which determines the energy spectrum.

Appendix C

Helmholtz equation and its solution

The Helmholtz equation is given by

$$(\nabla^2 + k^2)\psi = 0, \tag{C.1}$$

where $k = \omega\sqrt{\varepsilon_r\varepsilon_0\mu_0}$ is a constant and $\psi \equiv \psi(r, \theta, \phi)$ is some scalar function. Inserting the expression of laplacian ∇^2, in the spherical polar coordinate system given by

$$\nabla^2\psi = \frac{1}{r^2}\frac{\partial}{\partial r}\left(r2\frac{\partial\psi}{\partial r^2}\right) + \frac{1}{\sin\theta}\frac{\partial}{\partial\theta}\left(\sin\theta\frac{\partial\psi}{\partial\theta}\right) + \frac{1}{r^2\sin^2\theta}\frac{\partial^2\psi}{\partial\phi^2} \tag{C.2}$$

in equation (4.29) we simply get

$$\frac{1}{r^2}\frac{\partial}{\partial r}\left(r2\frac{\partial\psi}{\partial r^2}\right) + \frac{1}{\sin\theta}\frac{\partial}{\partial\theta}\left(\sin\theta\frac{\partial\psi}{\partial\theta}\right) + \frac{1}{r^2\sin^2\theta}\frac{\partial^2\psi}{\partial\phi^2} + k^2\psi = 0 \tag{C.3}$$

To solve the Helmholtz equation, it is convenient to use the method of separation of variables. Separation means that the solution is written in a factored form:

$$\psi(r, \theta, \phi) = R(r)\Theta(\theta)\Phi(\phi) \tag{C.4}$$

Inserting eq. (C.4) in eq. (C.3) we obtain

$$r^2\sin^2\theta\frac{\ddot{R}}{R} + 2r\sin^2\theta\frac{\dot{R}}{R} + \sin^2\theta\frac{\ddot{\Theta}}{\Theta} + \sin\theta\cos\theta\frac{\dot{\Theta}}{\Theta} + \frac{\ddot{\Phi}}{\Phi} + \omega^2\varepsilon_r\varepsilon_0\mu_0 r^2\sin^2\theta = 0 \tag{C.5}$$

where the dots denote derivates with respect to r, θ, ϕ as the case may be. Since ϕ occurs in the differential equation of the second order $\ddot{\Phi}/\Phi$ only, it can be replaced by a constant $-m^2$, i.e.,

$$\frac{\ddot{\Phi}}{\Phi} + m^2 = 0 \tag{C.6}$$

The solutions of eq. (C.6) are of the form

$$\Phi(\phi) \sim \left\{ \begin{array}{c} \cos \\ \sin \end{array} \right\}. \tag{C.7}$$

Thus, eq. (C.5) is reduced to the following form:

$$\frac{r^2}{R}\left[\ddot{R} + \frac{2\dot{R}}{r} + \omega^2 \varepsilon_r \varepsilon_0 \mu_0 R\right] + \frac{1}{\Theta}\left[\ddot{\Theta} + \cot\theta\dot{\Theta} - \frac{m^2\Theta}{\sin^2\theta}\right] = 0. \qquad (C.8)$$

Since the first bracketed term contains r only and the second bracketed term contains θ only, these two terms can separately be equated to a constant. We let the first bracketed term be replaced by a constant $n(n+1)$ then we get

$$\ddot{\Theta} + \cot\theta\dot{\Theta} + \left[n(n+1) - \frac{m^2}{\sin^2\theta}\right]\Theta = 0, \qquad (C.9)$$

$$\ddot{R} + \frac{2\dot{R}}{r} + \left[\omega^2\varepsilon_r\varepsilon_0\mu_0 - \frac{n(n+1)}{r^2}\right]R = 0. \qquad (C.10)$$

The solutions to the angular equation for Θ, eq. (C.9), are associated Legendré polynomials $P_n^m(\cos\theta)$ and $Q_n^m(\cos\theta)$. However, only $P_n^m(\cos\theta)$ is the acceptable solution since $Q_n^m(\cos\theta)$ leads to infinite values[1] of ψ and hence, of the magnetic field. Thus, the solution of eq. (C.9) is given by

$$\Theta(\theta) \sim P_n m(\cos\theta). \qquad (C.11)$$

Substituting $X = R\sqrt{r}$ in eq. (C.10), it reduces to

$$\ddot{X} + \frac{\dot{R}}{r} + \left[\omega^2\varepsilon_r\varepsilon_0\mu_0 - \frac{(n+(1/2))^2}{r^2}\right]X = 0, \qquad (C.12)$$

, where the dots denote derivatives with respect to r. Eq. (C.10) is recognized as a Bessel differential equation of order $(n+(1/2))$. Changing the variable from r to $(\sqrt{\omega^2\varepsilon_0\mu_0\varepsilon_r})r = (\omega\sqrt{\varepsilon_0\mu_0\varepsilon_r}) = (\frac{\omega}{c}\sqrt{\varepsilon})r = kr$, where $c = 1/\sqrt{\varepsilon_0\mu_0}$ is the speed of light in vacuum, eq. (C.12) has the solutions of the form $J_{n+(1/2)(kr)}$ or $Y_{n+(1/2)(kr)}$ or a linear combination of these two. But since $Y_{n+(1/2)(kr)}$ has infinite value at $r = 0$, the only acceptable solution to eq. (C.12) is of the form

$$X(r) \sim J_{n+(1/2)(kr)}. \qquad (C.13)$$

Thus, $R(r) \sim J_{n+(1/2)(kr)/\sqrt{r}}$ and the total solution is given by

$$\Psi(r, \theta, \phi) = \frac{A}{\sqrt{r}}J_{n+(1/2)}(kr)P_n^m(\cos\theta)\cos m\phi \qquad (C.14)$$

where A is a constant.

---

[1] This is due to the singularities it has at $\cos\theta = \pm 1$.

Appendix D

Mode-spacing for droplets lying on various surfaces

Laser Spectra

Mode-spacing for the droplet with R=330E-6 m lying on a rough silicon teflon deposited surface. The mean pump power is 35 mW.
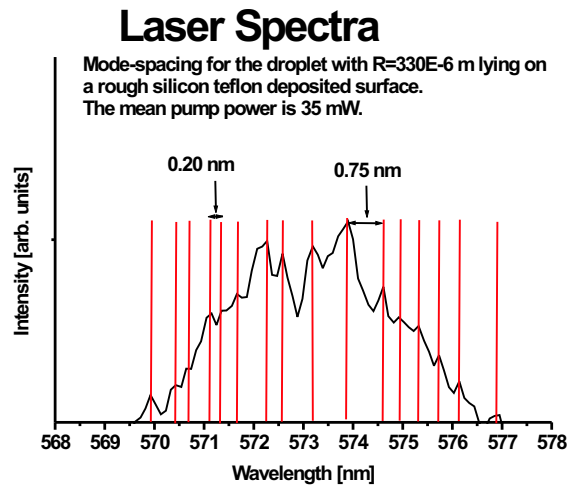
Figure D.1: A close-up of the emission spectrum shown in Fig 7.15 in order to measure the mode-spacing for the mean pump power 35 mW. 16 peaks are marked with the red vertical lines. The mode-spacing values for the peaks indicated varies from 0.20 nm to 0.75 nm.
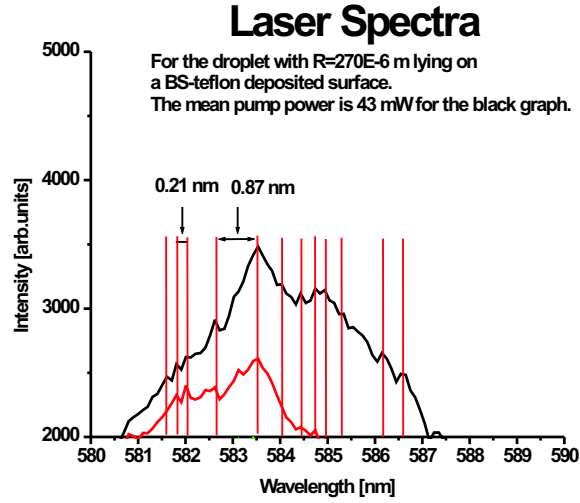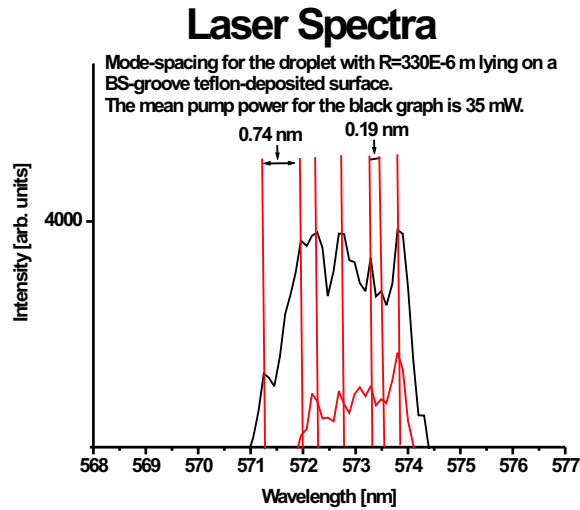
Figure D.2: A close-up of the emission spectrum shown in Fig 7.19 in order to measure the mode-spacing for the mean pump power 43 mW. 12 peaks are marked with the red vertical lines. The mode-spacing values for the peaks indicated varies from 0.19 nm to 0.74 nm.

Figure D.3: A close-up of the emission spectrum shown in Fig 7.22 in order to measure the mode-spacing for the mean pump power 35 mW. 7 peaks are marked with the red vertical lines. The mode-spacing values for the peaks indicated varies from 0.19 nm to 0.74 nm. and 0.94 nm.

Appendix E

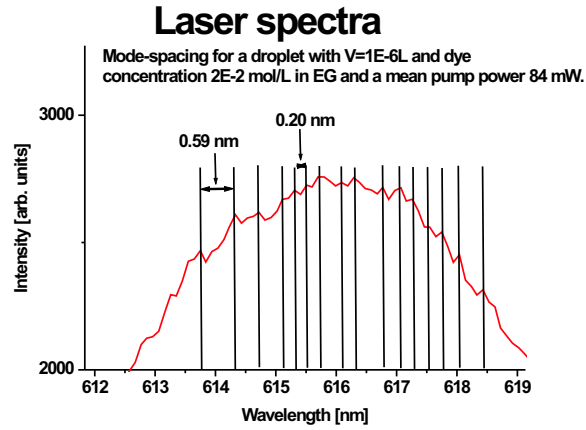# Mode-spacing for levitated droplets

Figure E.1: A close-up of the emission spectrum shown in Fig 7.32(a) in order to measure the mode-spacing for the mean pump power 84 mW. 16 peaks are marked with the black vertical lines. The mode-spacing values for the peaks indicated varies from 0.20 nm to 0.59 nm. However, the mode-spacing with values near 0.20 nm are more courteously.
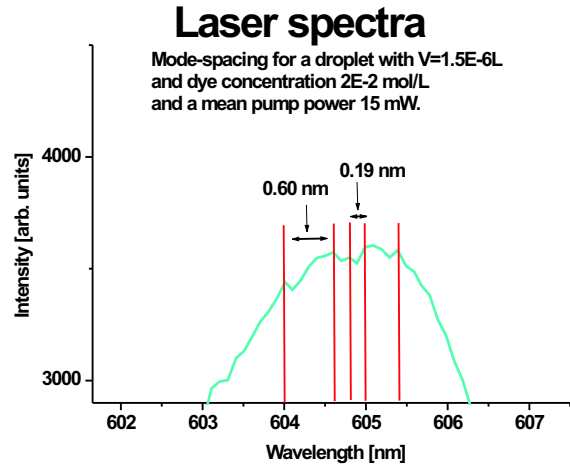
Figure E.2: A close-up of the emission spectrum shown in Fig 7.30 in order to measure the mode-spacing for the mean pump power 15 mW. 5 peaks are marked with the red vertical lines. The mode-spacing values for the peaks indicated varies from are 0.19 nm and 0.60 nm.

Appendix F

International Conference Contribution

The enclosed poster was submitted and presented in the Eighth International Conference on Micro Total Analysis Systems (μTAS), 26-30 September in Malmö, Sweden.
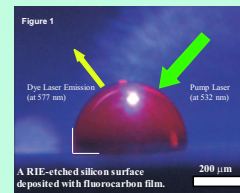
Liquid Droplet Dye Laser

Hatim Azzouz[1], Søren Balslev, and Anders Kristensen

MIC- Department of Micro and Nanotechnology, Technical University of Denmark (DTU), DK-2800 Kongens Lyngby, Denmark

[1]ha@mic.dtu.dk
www.mic.dtu.dk

Introduction

▪ We present the first observation of lasing in a droplet of laser dye deposited on a hydrophobic substrate.

▪ The droplets consists of the laser dye Rhodamine 6G dissolved in ethylene glycol (EG) and are optically pumped (at 532 nm) by an external frequency doubled ND:YAG laser.

▪ Why choose EG as a dye solvent? To from a usable droplet we are interested in the following: (1) A dye solvent with low evaporation rate and (2) a solvent having a relatively low polarity, in order for the laser dye to retain a high quantum yield. EG fulfils these criteria.

Figure 1

Dye Laser Emission (at 577 nm)   Pump Laser (at 532 nm)

A RIE-etched silicon surface deposited with fluorocarbon film.   200 µm

Hydrostatics of microdroplet

1. We need a spherical droplet because: (1) A spherical drop geometry can be described by only to parameters, radius R and contact angle θ (Figure 2) and (2) the lasing optical geometry for a spherical droplet is much simpler to describe.

Figure 2

2. Requiring a hemispherical shape of the droplet, the Bondnumber estimates the droplet radius to be much less than 1 mm.

3. This was investigated by using a simulation program to predict the shape of the droplet for various radii, leading to the following:
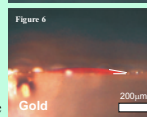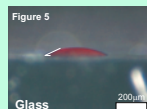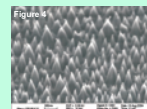

Figure 3.A

Figure 3.B

A. Given a contact angle of 140º and a radius of 1 cm, the shape of the droplet becomes squashed.

B. Given the same contact angle and a radius of 0.1 mm, the shape of the droplet becomes hemispherical. This is in good agreement with the estimate given by the Bondnumber.

Fabrication of hydrophobic surfaces

▪ Ensuring a hemispherical shape only the optimization of the contact angle is left. A surface with roughness of 200-300 nm is fabricated by an anisotropic silicon Reactive Ion Etch (RIE) based on SF_6 and O_2, se Figure 4. The surface is made hydrophobic by deposition of a fluorocarbon film deposited from a C_4F_8 plasma.

▪ The contact angle for ethylene glycol on this surface was optimized to 90º . For comparison, the contact angle for gold and glass were measured to 21º and 30º, respectively. This is shown in Figure 5 and 6.

▪ Droplets with linear dimensions in the 100 micron range were deposited by a dip pen method.

Figure 4

Figure 5

Glass   200µm

Figure 6

Gold   200µm

Lasing measurements

A series of the measured emission spectra from droplet optically pumped at 532 nm. The seven displayed spectra are recorded with different optical pumping power and displays a multimode structure. At an optical pumping power above threshold, a distinct peak (approximately 7 nm FWHM) appears on top of the more than 50 nm wide fluorescence from the Rh6G laser dye.

Laser threshold

Laser spectra

2 mW
82 mW
118 mW
133 mW
148 mW
155 mW
166 mW
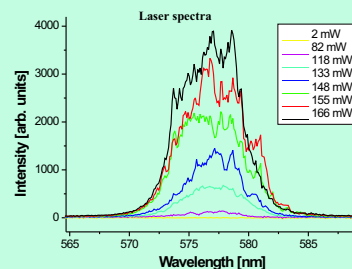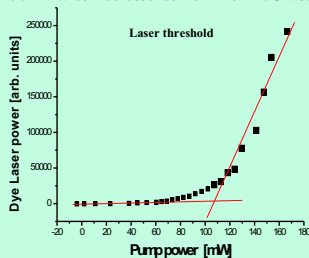
A plot of the emitted power output, reveals lasing characteristics of the system, with threshold for lasing around 100 mW and a linear rise of output power for increased pumping. The pump laser was pulsed at 10 Hz with 5 ns pulses.

Conclusion & Outlook

▪ The lasing in the liquid droplet dye laser has been demonstrated in thin sheets of liquid laser dye, relying only on reflections at the liquid-air interfaces.

▪ Laser dye functionalised droplets adds a new range of possibilities for droplet manipulating systems, both with regards to sensor applications and laser physics in the self-organized spherical cavities whose shape can be tuned.